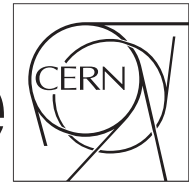


The Compact Muon Solenoid Experiment

CMS Draft Note

Mailing address: CMS CERN, CH-1211 GENEVA 23, Switzerland



2018/01/30

Head Id: 407949

Archive Id: 443339

Archive Date: 2017/06/01

Archive Tag: trunk

Search for new physics with dijet angular distributions in proton-proton collisions at $\sqrt{s}=13$ TeV

Leonard Apanasevich¹, Andreas Hinzmann², Klaus Rabbertz³, Nikos Varelas¹, and Jingyu Zhang¹

¹ University of Illinois at Chicago

² University of Hamburg

³ Karlsruhe Institute of Technology

Abstract

A search for extra spatial dimensions, quantum black holes, and quark contact interactions using measurements of dijet angular distributions in proton-proton collisions at $\sqrt{s} = 13$ TeV is presented. The data were collected with the CMS detector at the CERN LHC and correspond to an integrated luminosity of 35.9 fb^{-1} . The distributions are found to be in agreement with predictions from perturbative quantum chromodynamics that include electroweak corrections. The most stringent lower limits to date are set on the scale of graviton exchange. In the Giudice–Rattazzi–Wells convention, virtual graviton exchange is excluded up to a scale of 10.6 TeV at 95% confidence level. The production of quantum black holes is excluded for masses below 8.3 and 6.0 TeV depending on the scenario. Limits for different contact interaction models are obtained. In the benchmark scenario, valid to next-to-leading order in quantum chromodynamics, and in which only left-handed quarks participate, quark contact interactions are excluded to a scale of 13.1 (17.4) TeV for destructive (constructive) interference. Mediators in a simplified model of interactions between quarks and dark matter with masses between 2.5 and 4.4 or 5.0 TeV are excluded for vector or axial-vector mediators.

This box is only visible in draft mode. Please make sure the values below make sense.

PDFAuthor: Leonard Apanasevich, Andreas Hinzmann, Klaus Rabbertz, Nikos Varelas, Jingyu Zhang

PDFTitle: Search for new physics with dijet angular distributions in proton-proton collisions at $\text{sqrt}s = 13 \text{ TeV}$

PDFSubject: CMS

PDFKeywords: CMS, physics, QCD, contact interactions, extra dimensions, quantum black holes

Please also verify that the abstract does not use any user defined symbols

DRAFT

1 Introduction

2 High energy proton-proton collisions with large momentum transfers predominantly produce
 3 events containing two jets (dijets) with high transverse momenta (p_T). Such events probe the
 4 interacting partons at the shortest distance scales and provide a fundamental test of quantum
 5 chromodynamics (QCD). They can also be used to test the standard model (SM) at previously
 6 unexplored small distance scales, to search for signals predicted by new physics models, such
 7 as substructure of quarks (quark compositeness), additional compactified spatial dimensions,
 8 and quantum black holes.

9 The dijet angular distribution probes the properties of parton-parton scattering without strong
 10 dependence on the parton distribution functions (PDFs). The reason for this is the dominance
 11 of the t-channel gluon exchange in the three main scattering processes, $qg \rightarrow qg$, $q\bar{q}(q') \rightarrow$
 12 $q\bar{q}(q')$, and $gg \rightarrow gg$, which makes their angular distributions similar. $\chi_{\text{dijet}} = \exp(|(y_1 - y_2)|)$,
 13 where y_1 and y_2 are the rapidities of the two leading jets, $y \equiv \frac{1}{2}\ln[(E + p_z)/(E - p_z)]$, and
 14 p_z is the projection of the jet momentum on the beam axis. The choice of this variable was
 15 motivated by the fact that Rutherford scattering the χ_{dijet} distribution is flat. It also allows
 16 signatures of new physics that might have a more isotropic angular distribution than QCD
 17 (e.g., quark compositeness) to be more easily examined as they would produce an excess at low
 18 values of χ_{dijet} . Measurements of dijet angular distributions have previously been reported at
 19 the Tevatron by the D0 [1, 2] and CDF [3] collaborations, and at the LHC by the ATLAS [4–8]
 20 and CMS [9–13] collaborations.

21 A common signature of quark compositeness models is the appearance of new interactions be-
 22 tween quark constituents at a characteristic scale Λ that is much larger than the quark masses.
 23 At energies well below Λ , these interactions can be approximated by a contact interaction
 24 (CI) [14, 15] characterized by a four-fermion coupling. In this letter, flavor-diagonal color-
 25 singlet couplings between quarks are studied. These can be described by the effective La-
 26 grangian [14, 16]

$$\mathcal{L}_{qq} = \frac{2\pi}{\Lambda^2} [\eta_{LL}(\bar{q}_L \gamma^\mu q_L)(\bar{q}_L \gamma_\mu q_L) + \eta_{RR}(\bar{q}_R \gamma^\mu q_R)(\bar{q}_R \gamma_\mu q_R) + 2\eta_{RL}(\bar{q}_R \gamma^\mu q_R)(\bar{q}_L \gamma_\mu q_L)],$$

27 where the subscripts L and R refer to the chiral projections of the quark fields and η_{LL} , η_{RR} , and
 28 η_{RL} can be 0, +1, or -1. The various combinations of η_{LL} , η_{RR} , and η_{RL} correspond to different
 29 CI models. The following CI scenario is investigated:

Λ	$(\eta_{LL}, \eta_{RR}, \eta_{RL})$
Λ_{LL}^\pm	(±1, 0, 0)
Λ_{RR}^\pm	(0, ±1, 0)
Λ_{VV}^\pm	(±1, ±1, ±1)
Λ_{AA}^\pm	(±1, ±1, ±1)
$\Lambda_{(V-A)}^\pm$	(0, 0, ±1)

31 The most stringent limits on these models come from the searches studying the dijet angular
 32 distributions [8, 13] at high jet-jet masses and inclusive jet p_T [17] distribution.
 33 The dijet angular distributions are also sensitive to signatures from extra dimension models.
 34 The existence of compactified extra dimensions as proposed in the Arkani-Hamed-Dimopoulos-
 35 Dvali (ADD) model [18, 19] provides a possible solution to the hierarchy problem of the SM. In

the ADD model, gravity is assumed to propagate in the entire higher-dimensional space, while SM particles are confined to a 3+1 dimensional subspace. As a result, the fundamental Planck scale M_D in the ADD model is much smaller than the 3+1 dimensional Planck energy scale M_{Pl} , which may lead to phenomenological effects that can be tested with proton-proton collisions at the LHC. The coupling of the Kaluza-Klein modes to the SM energy-momentum tensor can be approximated by an effective theory with virtual graviton exchange at leading order in perturbation theory. Such a theory predicts a non-resonant enhancement of dijet production, whose angular distribution differs from QCD prediction. We consider two parametrizations for virtual graviton exchange in the ADD model, namely the GRW (Giudice, Rattazzi, Wells) [20] and the HLZ (Han, Lykken, Zhang) [21] convention. In the GRW convention, the phenomenology after summing over the Kaluza-Klein states is controlled by a single parameter Λ_T . The HLZ convention describes the phenomenology in terms of the parameters M_S and n_{ED} , where M_S represents a string scale expected to be of order M_D and n_{ED} is the number of extra dimensions in a $4+n_{ED}$ dimensional space. The parameters M_S and n_{ED} can be directly related to Λ_T [22]. We consider scenarios with 2 to 6 extra dimensions. The case of $n_{ED} = 1$ is not considered since it would require extra dimensions of sizes larger than 1 mm, which are already excluded experimentally. The case of $n_{ED} = 2$ is special in the sense that the relation between M_S and Λ_T also depends on the parton-parton center of mass energy $\sqrt{\hat{s}}$. The effective theory is expected to break down at an energy scale of order M_D . Therefore the range of M_S which we explore is higher than the highest dijet mass we measure. Signatures from virtual graviton exchange have previously been searched for in dilepton [23–25], diphoton [26–29] and dijet [30, 31] final states where the most stringent limits come from the dijet search [13].

Microscopic black holes can be produced at the LHC if the plank scale is modified to a few TeV in the context of large extra dimension models [32–34]. Semi-classical black holes, which have mass much greater than the plank scale and decay into multi-jets through Hawking radiation [35], have been studied in multi-jet final states at the LHC [36–40]. Quantum black holes (QBHs), unlike the semi-classical black holes, will be produced with mass near the plank scale and mostly decay into di-jets giving an excess at low χ_{dijet} [41–43]. Two large extra dimension models, ADD with number of extra dimensions $n_{ED} = 6$ (ADD6) and Randall-Sundrum model (RS1) [44, 45] are considered as benchmark models to provide low energy plank scale for the QBH productions. The QBH production cross section can be described by the classical geometrical cross section as: $\sigma_{\text{QBH}} \sim \pi r_s^2$ where r_s is the Schwarzschild radius of the black hole, and thus is proportional to the mass of the QBH and the plank scale (M_{plank}). As QBHs are produced with mass threshold close to the plank scale, we assume the minimum mass of QBH M_{QBH} equals to M_{plank} for simplification. Most stringent limits for searches on QBH productions at the LHC can be found in Ref. [8, 13].

In a simplified model of interactions between DM (χ) and quarks [46, 47], a DM mediator (Z') with unknown mass M_{Med} is assumed to be a spin-1 particle (vector or axial-vector) and to decay only to $q\bar{q}$ and pairs of DM particles, with mass m_{DM} , and with a universal quark coupling g_q and a DM coupling g_{DM} . This model has the following Lagrangian

$$L_{\text{vector}} = -g_{\text{DM}} Z'_{\mu} \bar{\chi} \gamma^{\mu} \chi - g_q \sum_{q=u,d,s,c,b,t} Z'_{\mu} \bar{q} \gamma^{\mu} q,$$

or

$$L_{\text{axial-vector}} = -g_{\text{DM}} Z'_{\mu} \bar{\chi} \gamma^{\mu} \gamma_5 \chi - g_q \sum_{q=u,d,s,c,b,t} Z'_{\mu} \bar{q} \gamma^{\mu} \gamma_5 q,$$

for vector and axial-vector mediator, respectively. Searches for dijet resonances [48, 49] exclude the quark couplings g_q in the range between 0.07 and 0.5, depending on M_{Med} . In a scenario

74 with $g_q = 0.25$ and a DM coupling $g_{\text{DM}} = 1.0$, vector and axial-vector mediator masses below
75 2 TeV are excluded. Searches for invisible particles produced in association with quarks or
76 bosons [50, 51], exclude axial-vector and vector mediators below 1 TeV and 2 TeV in scenarios
77 with $g_q = 0.25$ and $g_q = 1.0$, respectively, and $g_{\text{DM}} = 1.0$.

78 In this paper, our previous searches are extended to higher contact interaction (CI) scales using
79 a data sample corresponding to 35.9 fb^{-1} of integrated luminosity at $\sqrt{s} = 13 \text{ TeV}$, following
80 exactly the same analysis strategy. We first present the measurement of the dijet angular distri-
81 butions unfolded for detector effects and then search for evidence for CI and extra dimension
82 signatures.

83 This analysis note is structured as follows. In Section 2 the observables and analysis phase
84 space are defined. Section 3 summarizes the jet reconstruction and identification. Data samples,
85 triggers, event selection, data-MC comparisons, the unfolding correction applied to the data
86 and the systematic uncertainties are presented in Section 4. The theory prediction is discussed
87 in Section 5. The final result, the comparison of the unfolded data to the theory prediction,
88 is shown in Section 6. Section 7 describes the limit setting procedure on a contact interaction
89 model using the angular distributions.

DRAFT

90 2 Definition of Observable and Phase Space

91 The dijet system consists of the two largest transverse momentum jets in the event. The dijet
 92 mass is formally expressed as:

$$M_{jj}^2 = P_{j_1}^\mu P_{j_2}^\mu = (E_1 + E_2)^2 - (\vec{p}_1 + \vec{p}_2)^2 \quad (1)$$

93 where $P_{ji}^\mu = (E_i, \vec{p}_i)$ are the four-momenta of the two leading jets. In the limit of massless jets,
 94 the dijet mass can be expressed in terms of measured jet quantities as

$$M_{jj}^2 = 2p_{T_1}p_{T_2}[\cosh(\eta_1 - \eta_2) - \cos(\phi_1 - \phi_2)]. \quad (2)$$

95 As mentioned in the Introduction, the angular distribution is characterized by $\chi_{\text{dijet}} = \exp(2y^*)$
 96 where $y^* = \frac{1}{2}|y_1 - y_2|$. In massless $2 \rightarrow 2$ scattering processes, $\pm y^*$ are the rapidities of the two
 97 jets in the dijet center-of-mass frame which are related to the scattering angle in this frame, θ^* ,
 98 by $y^* = \frac{1}{2} \ln \left(\frac{1 + |\cos \theta^*|}{1 - |\cos \theta^*|} \right)$. In this approximation the dijet angular variable χ_{dijet} can be written
 99 as $\chi_{\text{dijet}} = \frac{1 + |\cos \theta^*|}{1 - |\cos \theta^*|}$. The variable $y_{\text{boost}} = \frac{1}{2}(y_1 + y_2)$ denotes the average rapidity of the two
 100 jets. In massless $2 \rightarrow 2$ scattering processes, y_{boost} specifies the longitudinal boost by which the
 101 dijet center-of-mass frame is boosted with respect to the detector frame.

102 2.1 Definition of Phase Space

103 In this analysis, the χ_{dijet} distribution is measured over the range $1 < \chi_{\text{dijet}} < 16$, which implies
 104 a maximum value of $y^* = 1.39$. The rapidity of each jet is restricted to $|y| = 2.5$ so that the jets
 105 were contained in a well understood region of the calorimeter. The maximum value of y_{boost}
 106 is constrained to $|y_{\text{boost}}| < 1.11$, since the variables y_{boost} , y^* , and y_{max} satisfy the inequality:
 107 $|y_{\text{boost}}| + y^* < |y_{\text{max}}|$.

108 The dijet angular distributions are measured in 7 bins of dijet mass: 2.4-3.0, 3.0-3.6, 3.6-4.2, 4.2-
 109 4.8, 4.8-5.4, 5.4-6.0, 6.0- ∞ TeV. The minimum mass threshold is chosen above the point where
 110 the jet triggers are fully efficient. The remaining dijet mass bins are chosen with a width well
 111 above the dijet mass resolution, requiring at least 50 events in highest mass bin, to allow a
 112 measurement of the shape of the angular distribution.

113 3 Jet Reconstruction

114 Particle flow jets were used to study the angular distribution of dijets. These jets are recon-
 115 structed using particles (charged hadron, neutral hadrons, electrons, muons and photons) re-
 116 constructed using all detector components (tracker, calorimeters and muon system) as input,
 117 excluding charged particles which do not originate from the primary vertex in the event. Jets
 118 are formed using the anti- k_T clustering algorithm with a size parameter $R = 0.4$. To com-
 119 pare the data with NLO and PYTHIA predictions, particle-level jets are made by applying the
 120 same jet clustering algorithm to the Lorentz vectors of stable particles generated in the case of
 121 PYTHIA, and to the outgoing partons in the case of NLO predictions.

122 3.1 Jet Identification

123 A set of jet identification (JetID) requirements has been determined to remove jets created from
 124 unphysical energy depositions in the calorimeter (e.g. noise, hot cells) [52]. For this analysis,
 125 the “tight” JetID selection criteria for particle flow jets have been applied. These criteria include
 126 requirements on the neutral hadron fraction (NHF), neutral electromagnetic fraction (NEF),
 127 charged hadron fraction (CHF), charged electromagnetic fraction (CEF), number of constituents
 128 ($n_{\text{constituents}}$) and charged multiplicity (n_{charged}). These requirements are summarized in Table 1.
 129 In addition, jets with a muon energy fraction greater than 0.8 are rejected to suppress noise from
 130 misreconstructed high energy muons. For jets with p_T greater than 30 GeV, losses due to the
 131 application of these selection criteria are estimated to be less than 1%.

Table 1: Tight particle flow jet quality criteria

variable	$ \eta $	tight JetID
NHF		< 0.9
NEF		< 0.9
CHF	< 2.4	> 0
CEF	< 2.4	< 0.99
$n_{\text{constituents}}$		> 1
n_{charged}	< 2.4	> 0

132 3.2 Jet Energy Scale Corrections

133 The transverse momenta of jets were corrected for the response of the detector using the relative
 134 (η) and absolute (p_T) jet corrections developed by the JetMET POG [53] in Summer16_23Sep2016V3*_DATA.
 135 These corrections are a combination of MC truth corrections determined from QCD events gen-
 136 erated by PYTHIA [54] and were further processed using a full, GEANT4-based [55] detector
 137 simulation and a residual correction determined from the absolute and relative jet response
 138 measured in dijet and photon+jet data. The corresponding uncertainties are parametrized as a
 139 function of η and p_T and range from 3%-4% for particle flow jets with $p_T > 100$ GeV.

140 4 Data Analysis

141 The data presented in this analysis corresponds to 35.9 fb^{-1} of integrated luminosity collected
 142 in 2016. The analysis was done using officially validated input events from the following
 143 datasets:

144 /JetHT/Run2016*23Sep2016*/MINIAOD

145 The selection of good runs and luminosity sections was technically implemented by using offi-
 146 cially produced JSON files /afs/cern.ch/cms/CAF/CMSCOMM/COMM_DQM/certification/
 147 Collisions16/13TeV/Cert_271036-284044_13TeV_23Sep2016ReReco_Collisions16_JSON.txt.

148 4.1 Triggers

149 The CMS trigger uses a two-tiered system to select physics events of interest for further analy-
 150 sis; Level-1 Trigger (L1) and High-Level Trigger (HLT). The trigger paths used in this analysis
 151 were the single jet triggers and HT triggers. The single jet trigger require a Level-1 jet and an
 152 HLT jet with certain thresholds (PFJet450). The HT trigger require the scalar sum of the trans-
 153 verse momenta of the jets at Level-1 and HLT with certain thresholds (PFHT900). The trigger
 154 logic between the single jet trigger and the HT trigger is OR.

155 The trigger turn-on curves have been measured using a lower threshold prescaled reference
 156 trigger (PFHT650 and PFJet320) within our analysis phase space as defined in Section 2. There-
 157 fore the turn-on curves were scaled by the effective luminosities of the triggers. The trigger
 158 efficiency in all 2016 data taking period as a function of dijet mass is shown in Figure 1. There
 159 is a know problem regarding the trigger that CMS observed some inefficiency for HT triggers
 160 in 2016 RunH period. To reproduce the HT trigger inefficiency, we measured the trigger effi-
 161 ciency for PFHT900 only as shown in Figure 2. The reference trigger used here are PFHT650
 162 OR PFJet320 as before. A cross check is made for the measurement of the trigger turn-on curve
 163 by replacing the reference trigger with an orthogonal trigger. Figure 3 shows the trigger turn-
 164 on curve with HLT_IsoMu24 as the reference trigger. To study the effect that events migrating
 165 from lower mass bin ($1.9 < m_{jj} < 2.4 \text{ TeV}$) to the first mass bin in Table 2 (see details in section
 166 4.4), we apply corrections for trigger inefficiency to events at mass bin $1.9 < m_{jj} < 2.4 \text{ TeV}$. The
 167 trigger corrections are derived from fits of trigger efficiencies in several bins in χ_{dijet} shown in
 168 Figure 4.

169 4.2 Event Selection

170 A primary vertex is required to be reconstructed from at least 5 tracks (fit $n_{\text{dof}} > 4$) with $|z_{\text{PV}}| <$
 171 24 cm with $\rho_{\text{PV}} = \sqrt{x_{\text{PV}}^2 + y_{\text{PV}}^2} < 2 \text{ cm}$. Filters for HBHE and HBHEiso noise, CSC beam halo
 172 noise, ECAL TP noise, EE bad SC noise, badMuon and badChargedHadron are applied. Finally
 173 events with the first two jets passing the tight jet ID(as described in Section 3.1) are selected and
 174 the analysis phase space cuts are applied. The final number of data events in each mass bin is
 175 summarized in Table 2 The highest value of M_{jj} observed in the data is 8153.3 TeV . The event
 176 display for this event can be seen from Figure 5. The p_T and rapidity of the two leading jets in
 177 this event are 2805.3 GeV and -1.1 and 2535.6 GeV and 0.9 . The χ_{dijet} for this event is 7.15 .

Table 2: The final number of data events in each mass bins.

Mass bin [TeV]	# events
2.4-3.0	353083
3.0-3.6	71840
3.6-4.2	16714
4.2-4.8	4287
4.8-5.4	1154
5.4-6.0	330
6.0- ∞	95

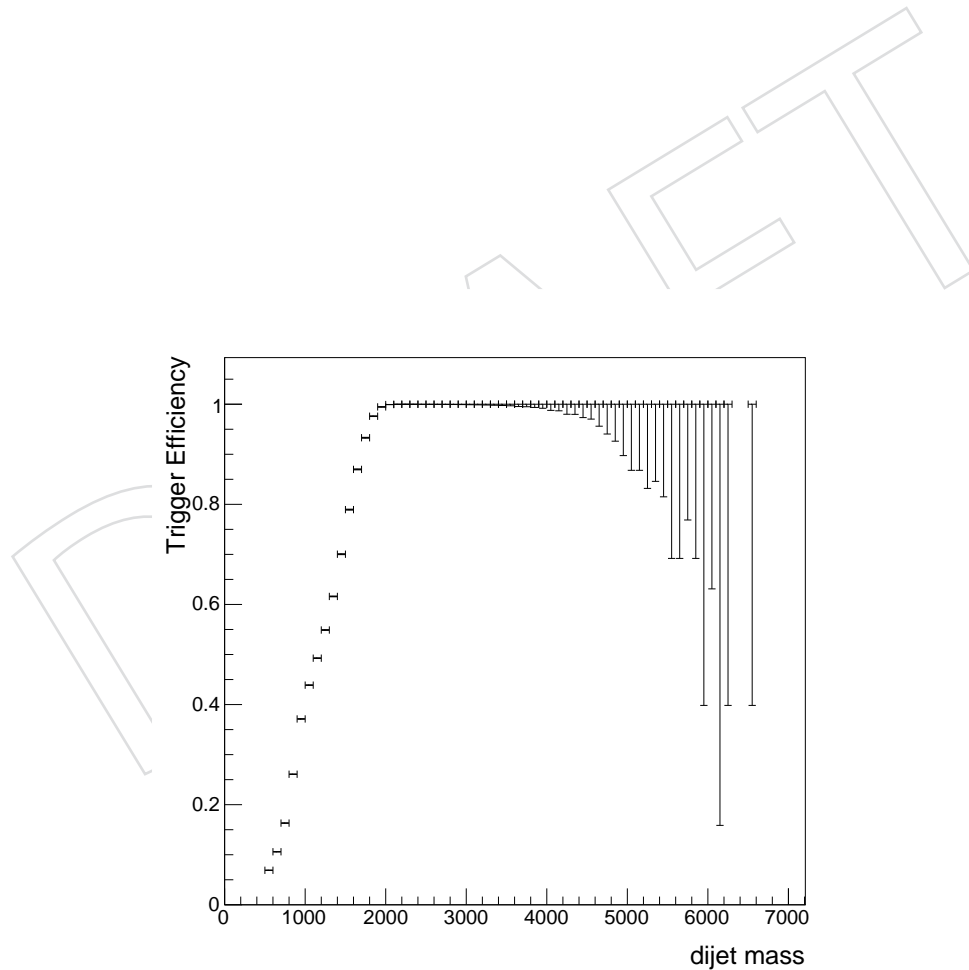


Figure 1: Trigger efficiency in 2016 datasets for HLT_PFT900 OR HLT_PFJet450 as a function of dijet mass.

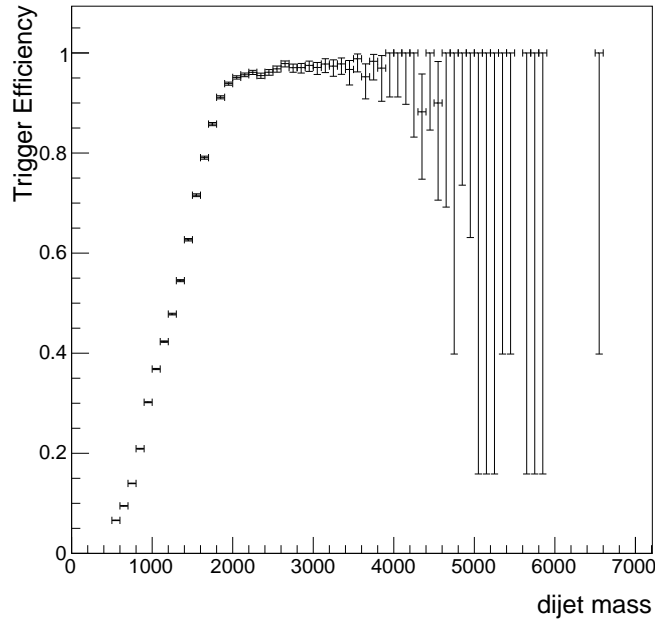


Figure 2: Trigger efficiency in 2016 RunH datasets for HLT_PFT900 as a function of dijet mass.

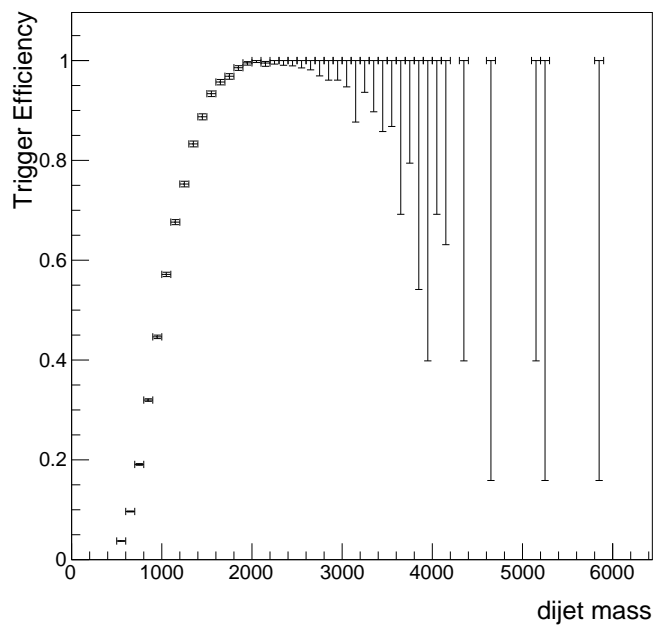


Figure 3: Trigger efficiency in 2016 datasets for HLT_PFT900 OR HLT_PFJet450 as a function of dijet mass with HLT_IsoMu24 as the reference trigger.

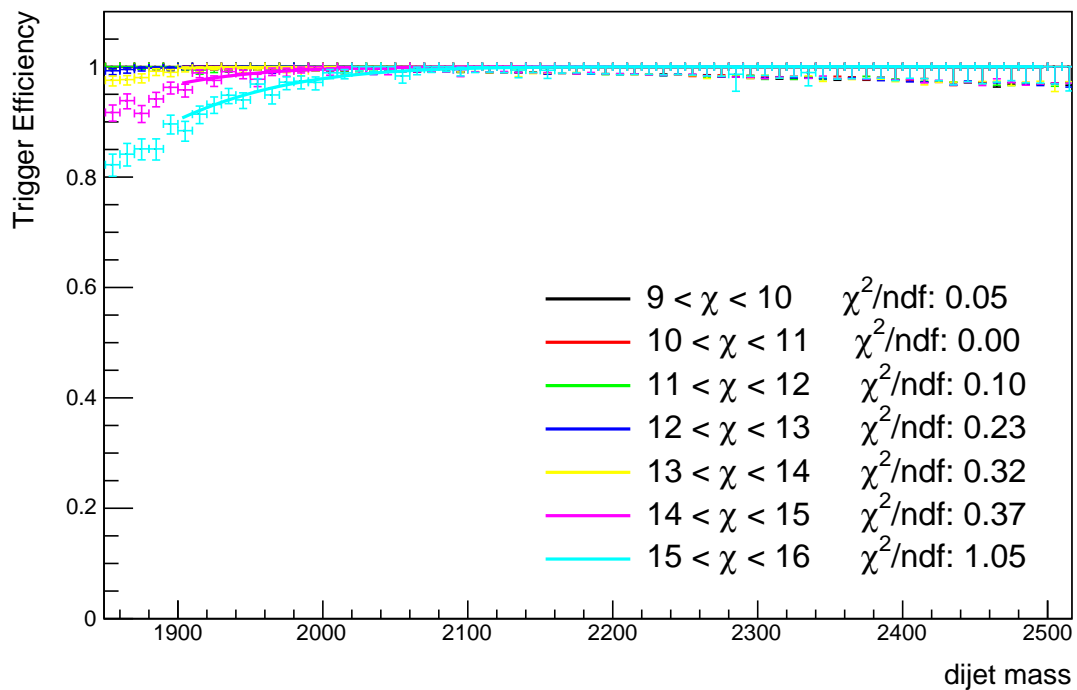


Figure 4: Fits of trigger efficiencies as a function of dijet mass in dijet mass range $1.9 < m_{jj} < 2.4$ TeV for several bins in χ_{dijet} greater than 9. For χ_{dijet} smaller than 9, the trigger is fully efficient in this dijet mass range.

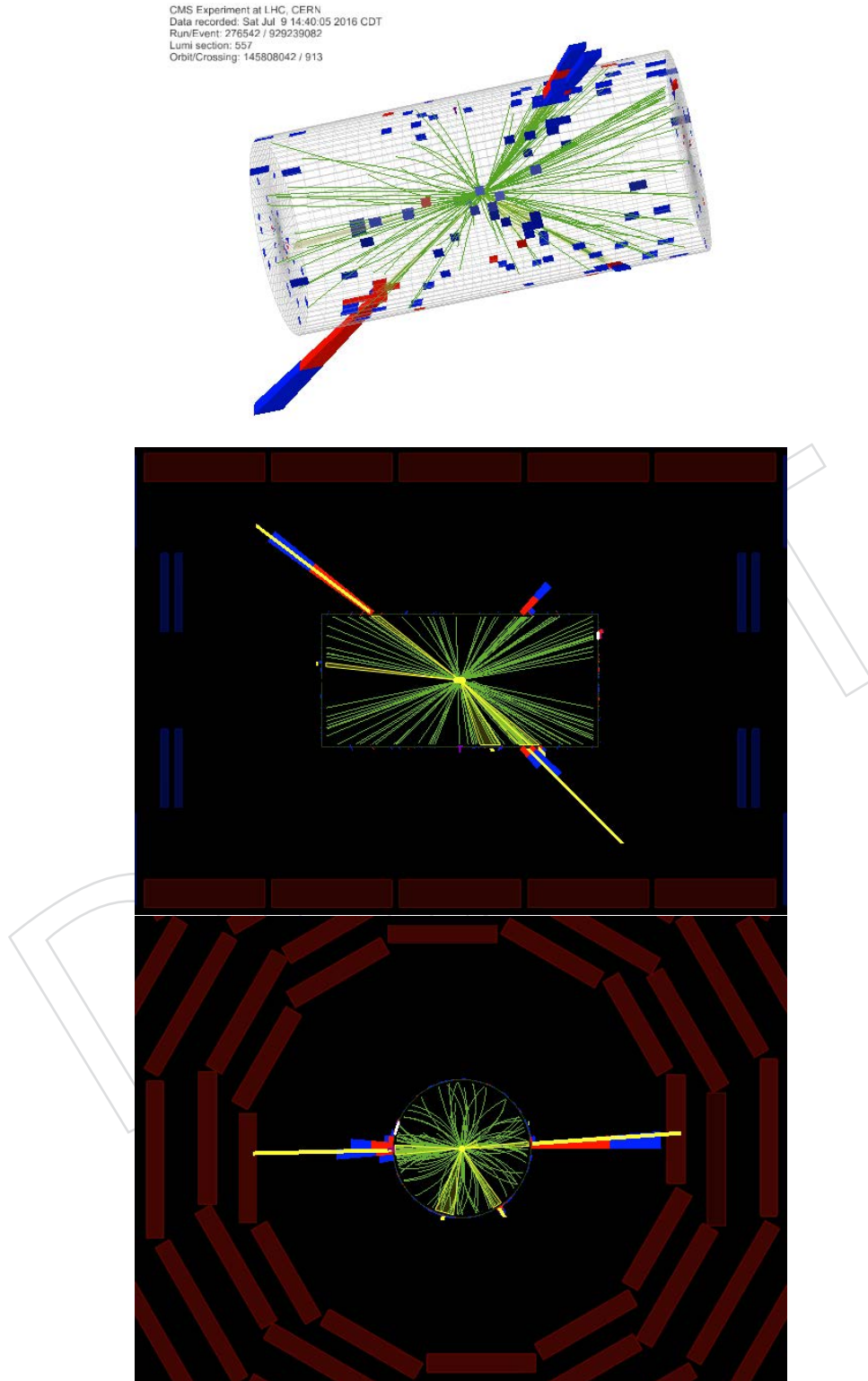


Figure 5: Event display for the event which has the highest M_{jj} .

178 4.3 Comparisons with the Detector Simulation

179 A detailed simulation of the CMS spectrometer has been developed using the GEANT4 pack-
 180 age to study the detector performance. Simulated events were processed and reconstructed in
 181 the same manner as collision data. In this analysis, the following Monte Carlo simulated sam-
 182 ples have been used. Fully simulated Herwigpp flat QCD with Tune TuneCUETHS1 (Moriond17)

183 /QCD_Pt-15to7000_TuneCUETHS1*/Summer16MiniAODv2-PUMoriond17*/*

184 , Fully simulated MadGraph with Tune CUETP8M1 (Moriond17)

185 /QCD_HT*to*_TuneCUETP8M1*/Summer16MiniAODv2-PUMoriond17_80X*/*

186 , Fully simulated Pythia8 flat QCD with Tune CUETP8M1 (Moriond17)

187 /QCD_Pt-15to7000_TuneCUETP8M1*/Summer16MiniAODv2-PUMoriond17_80X*/*

188 and privately generated particle-level Pythia8 Tune CUETP8M1 samples with significantly in-
 189 creased statistics using the official configurations.

190 A variety of comparisons were made between the data and simulation to verify that the sim-
 191 ulation provided an adequate description of the QCD events observed in the data. We ex-
 192 plore all mass regimes include the mass bin below 2.4 TeV. All the event selection requirements
 193 used in the final analysis have been applied to both MC and data. The events in mass region
 194 $1.9 < m_{jj} < 2.4$ TeV are corrected for trigger inefficiency. The MC distributions are nomalized
 195 to the number of events in data.

196 The comparison plot for dijet invariant mass in data and MC is shown in Figure 6 for M_{jj} . We
 197 do not use the LO QCD MC as a theory prediction, however, we use it to derive a detector
 198 response matrix for the unfolding. Therefore, the modeling of the dijet mass by the MC is im-
 199 portant. The modeling of all other kinematic properties of the LO QCD MC is of second order
 200 importance, since the detector response matrix is dominated by jet energy resolution effects
 201 migrating events between dijet mass bins. The jet angular resolution is practically perfect, as
 202 shown in [56] figure 22+23. Therefore modeling of the dijet angular distributions by the LO
 203 QCD MC is not important. In fact the LO QCD MC is not expected to describe well the dijet
 204 angular distribution and we use NLO QCD as our theory prediction.

205 First, we look at comparisons in mass bins listed in Table 2. In Figures 7 and 8 the p_T distribu-
 206 tions are compared for both the leading and 2nd-leading jets in the event in all mass bins. In
 207 Figures 9 and 10, the rapidities of the leading and 2nd-leading jets are plotted for all mass bins,
 208 respectively. In Figure 11, we compare the y_{boost} distributions in data and MC, in Figure 12, the
 209 χ_{dijet} distributions, in Figure 13 the $\frac{p_{T,1}-p_{T,2}}{p_{T,1}+p_{T,2}}$ distributions, in Figure 14, the $\Delta\phi_{1,2}$ distributions,
 210 and in Figure 15 the $E_T^{\text{miss}} / \sum E_T$ distributions.

211 The comparisons are shown for the full simulated Pythia, Herwig and MadGraph Monte Carlo.
 212 In general, there is reasonable agreement of data and MC. In most distributions, Pythia8 de-
 213 scribe the data well and Pythia together with Madgraph envelope the data. We therefore use
 214 Pythia8 to derive the response matrices and use Madgraph to predict the uncertainty due to
 215 MC modelling in unfolding.

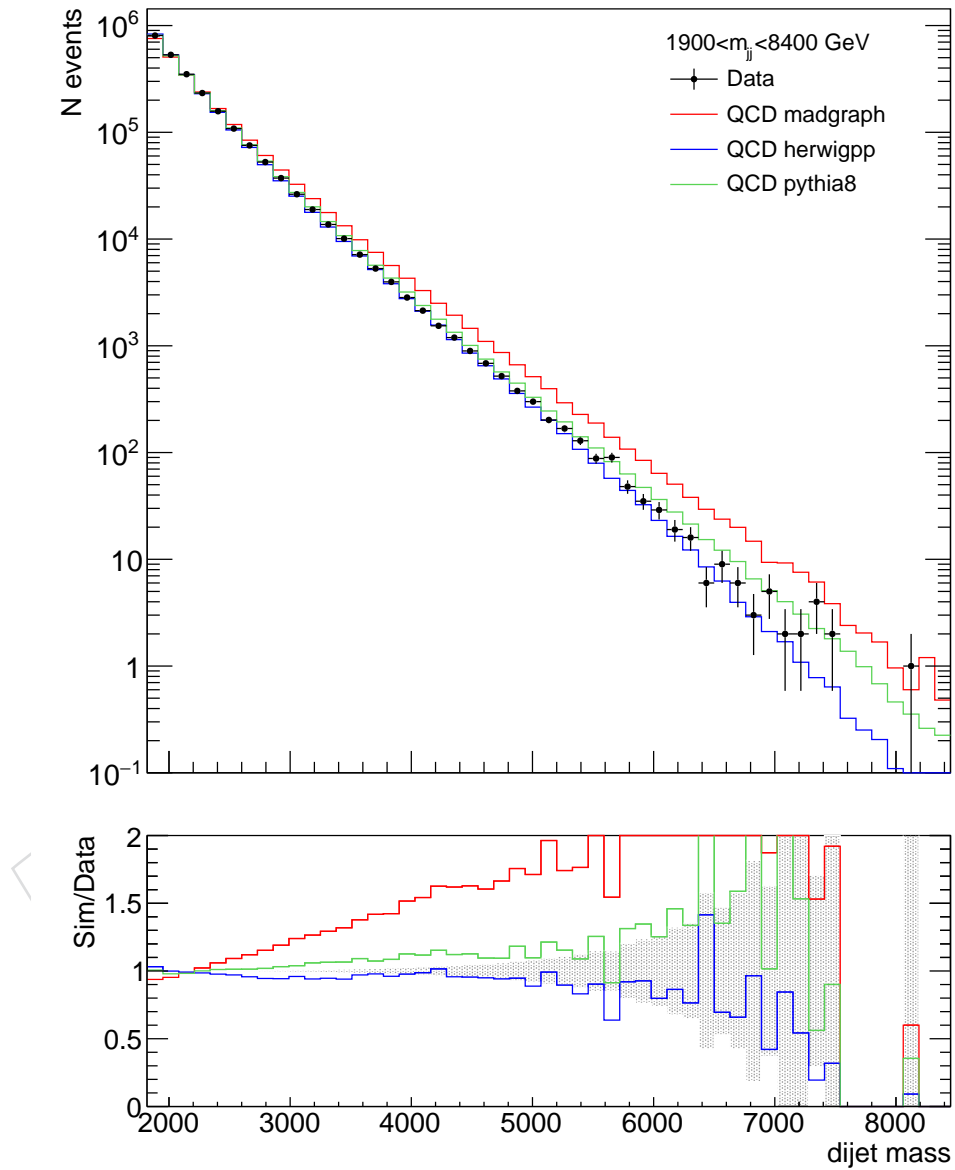


Figure 6: Comparisons of distributions in the dijet invariant mass between data (points) and simulation (histograms).

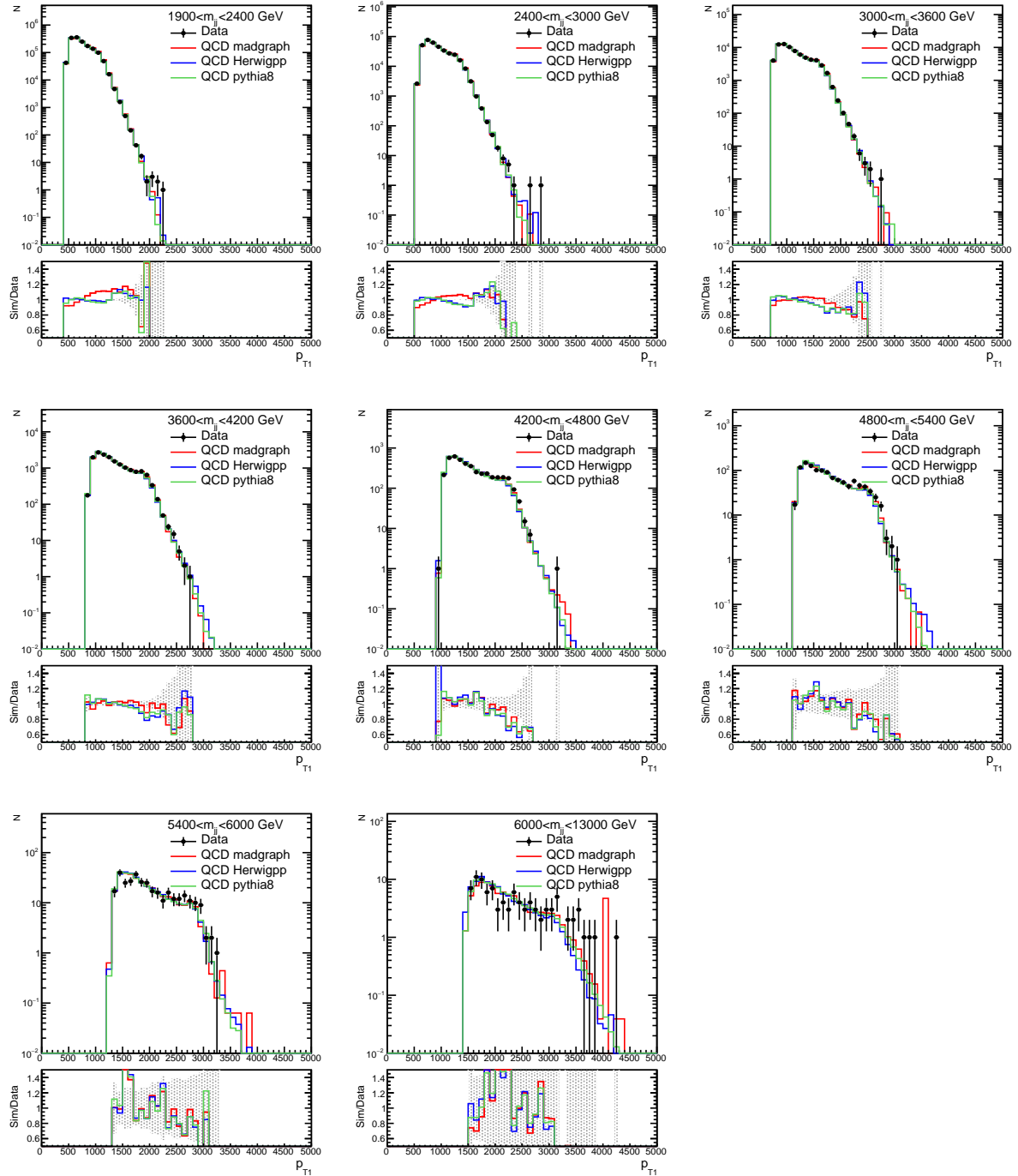


Figure 7: Comparisons of distributions in p_T for leading jet between data (points) and simulation (histograms).

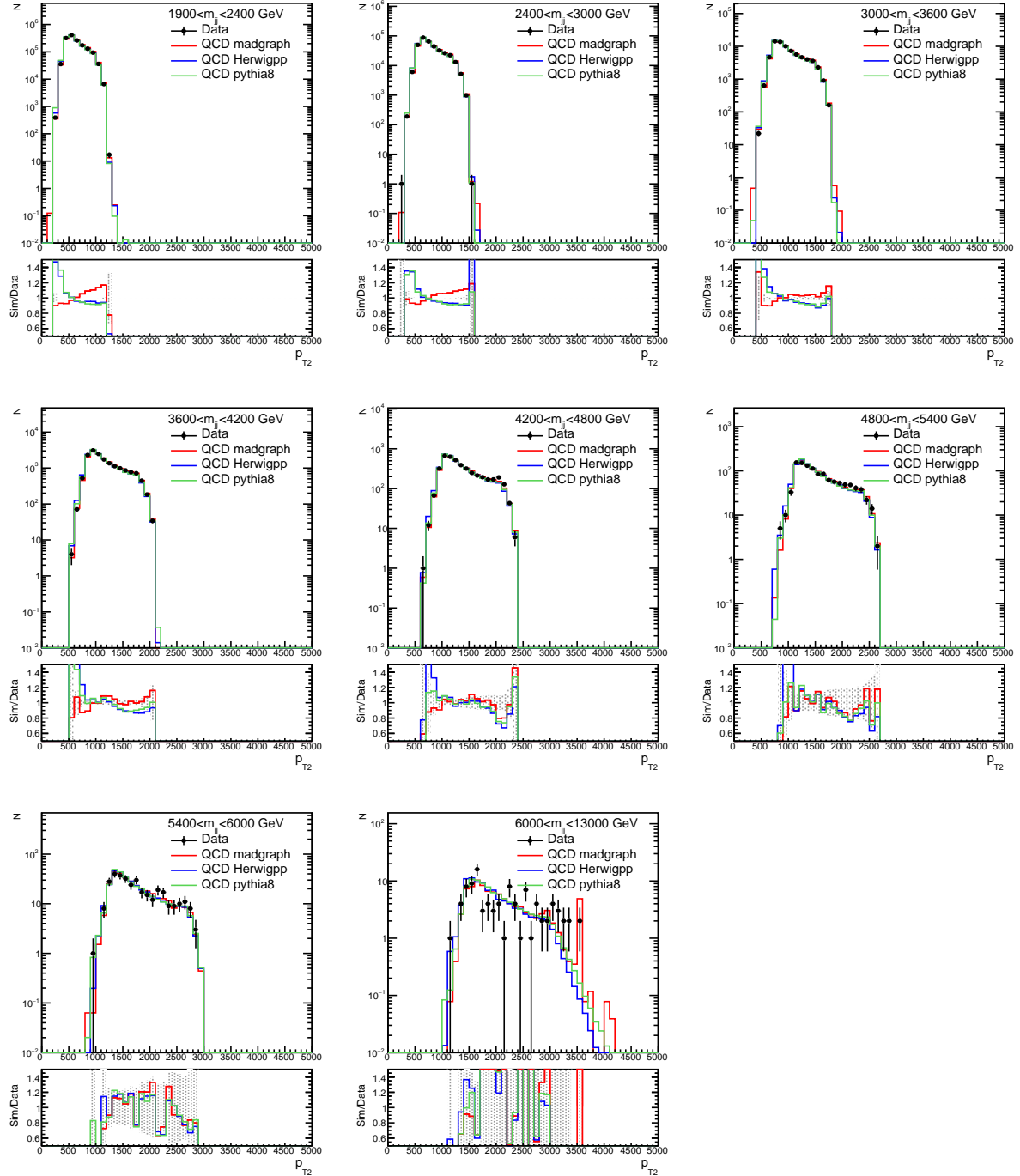


Figure 8: Comparisons of distributions in p_T for 2nd leading jet between data (points) and simulation (histograms).

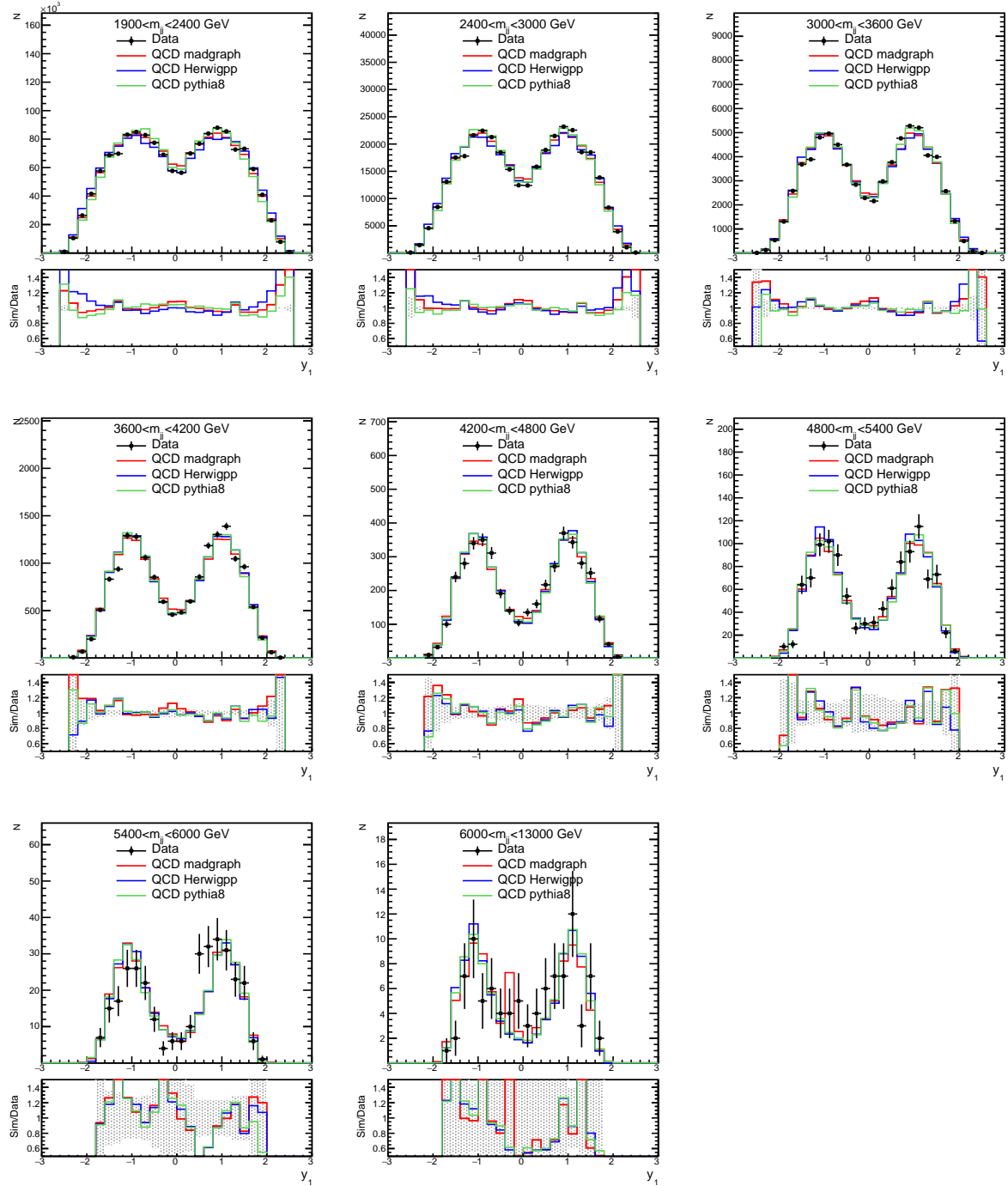


Figure 9: Comparisons of distributions in rapidity for leading jets between data (points) and simulation (histograms).

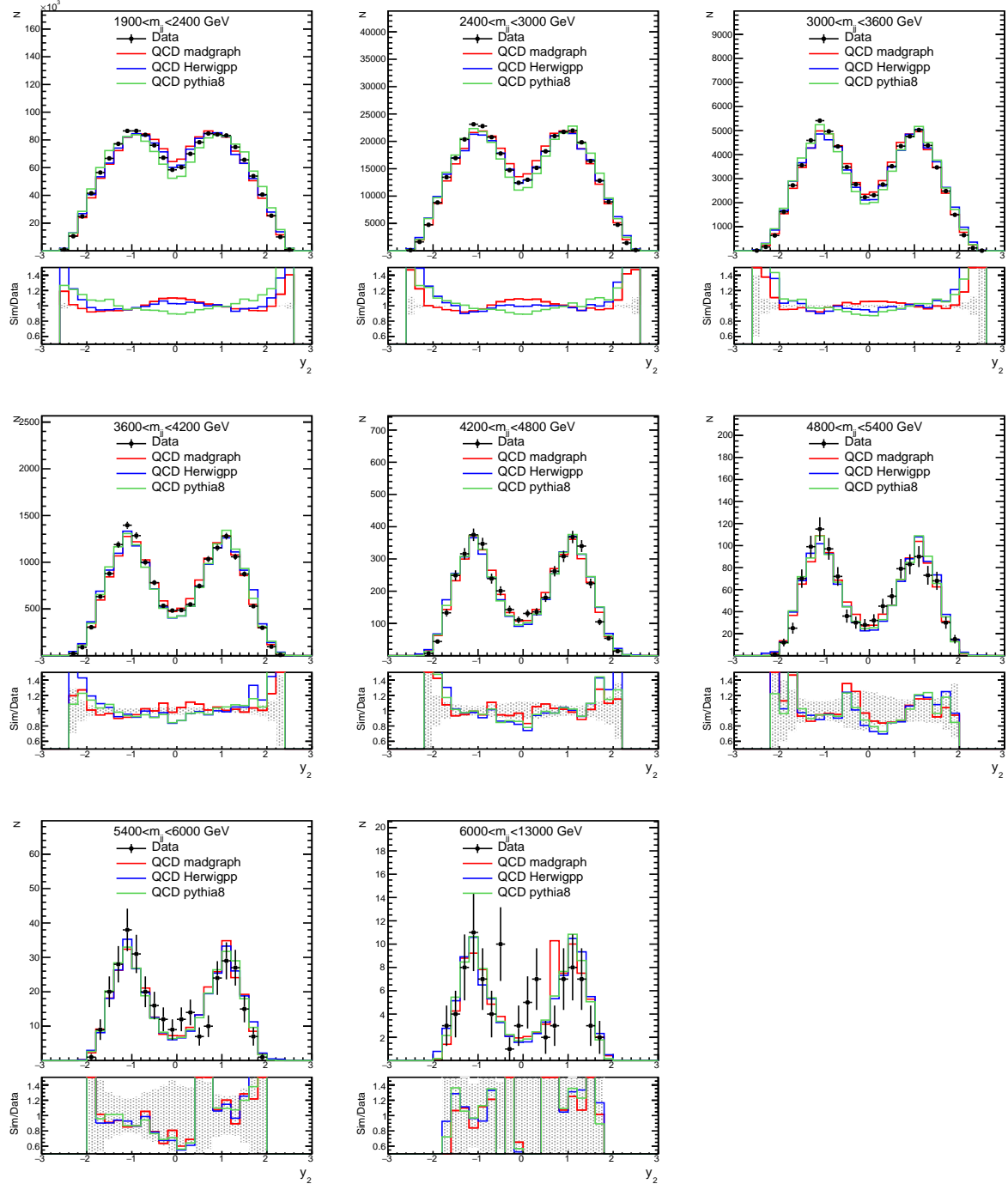


Figure 10: Comparisons of distributions in rapidity for 2nd-leading jets between data (points) and simulation (histograms).

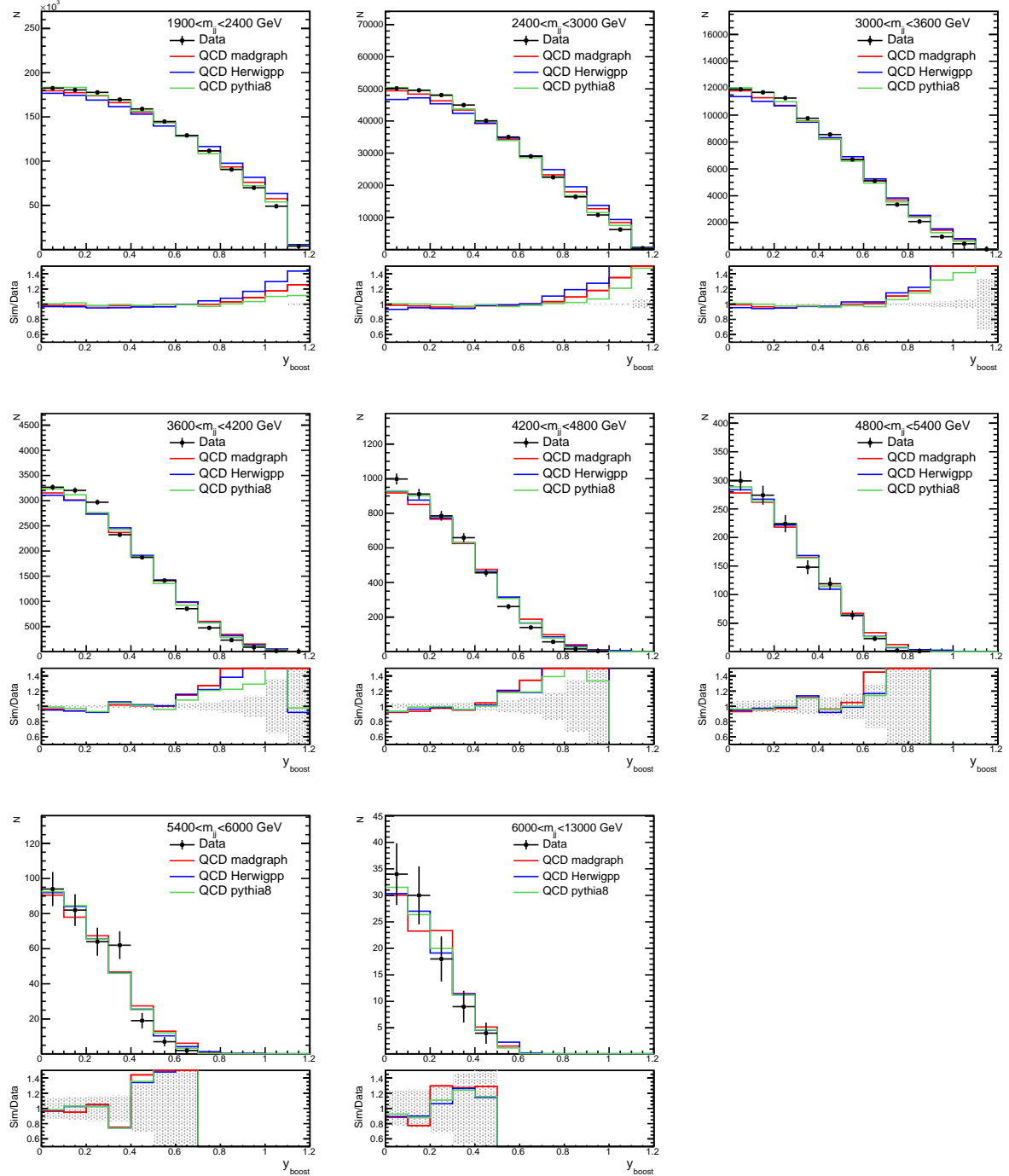


Figure 11: Comparisons of distributions in y_{boost} between data (points) and simulation (histograms).

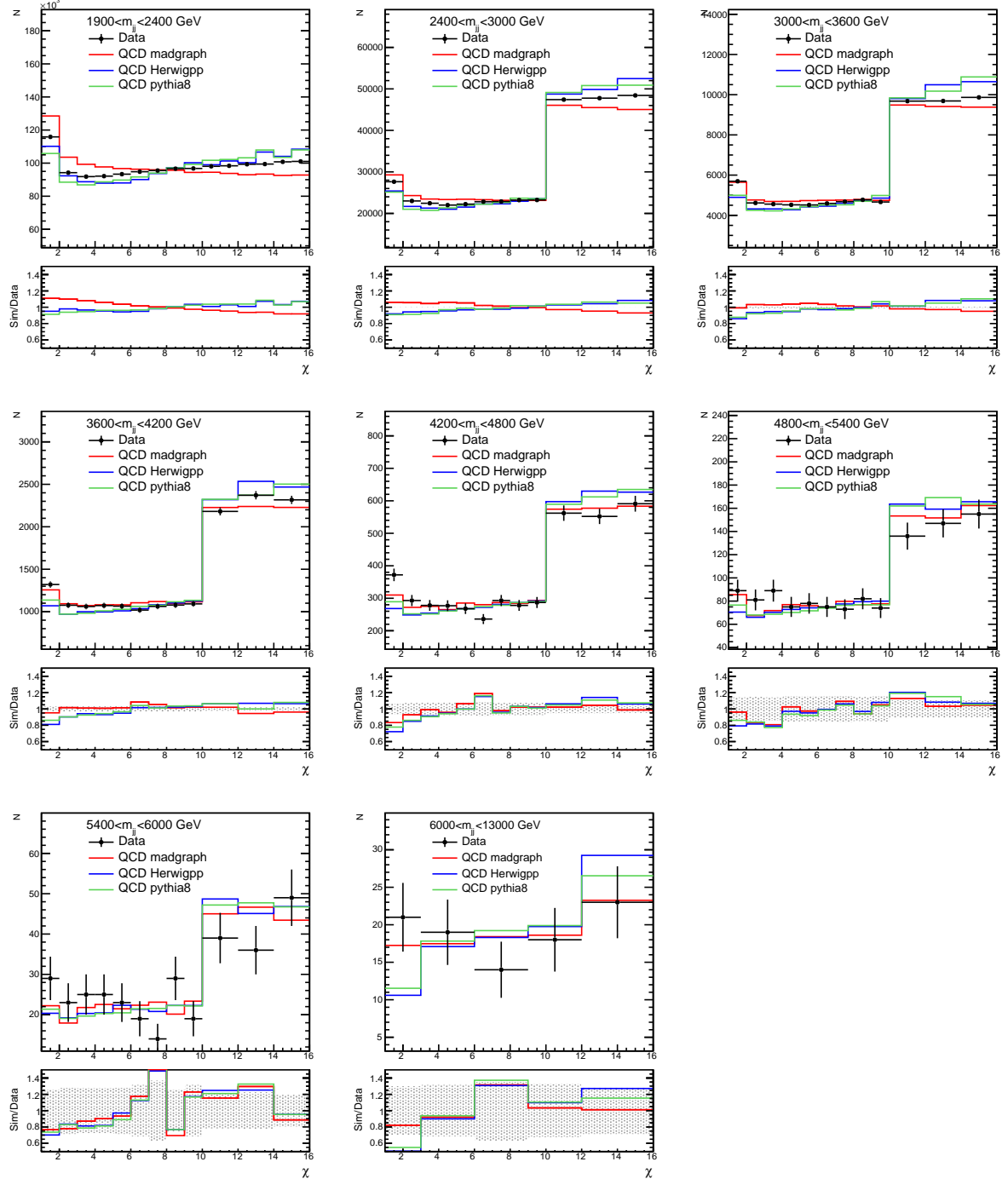


Figure 12: Comparisons of distributions in χ between data (points) and simulation (histograms).

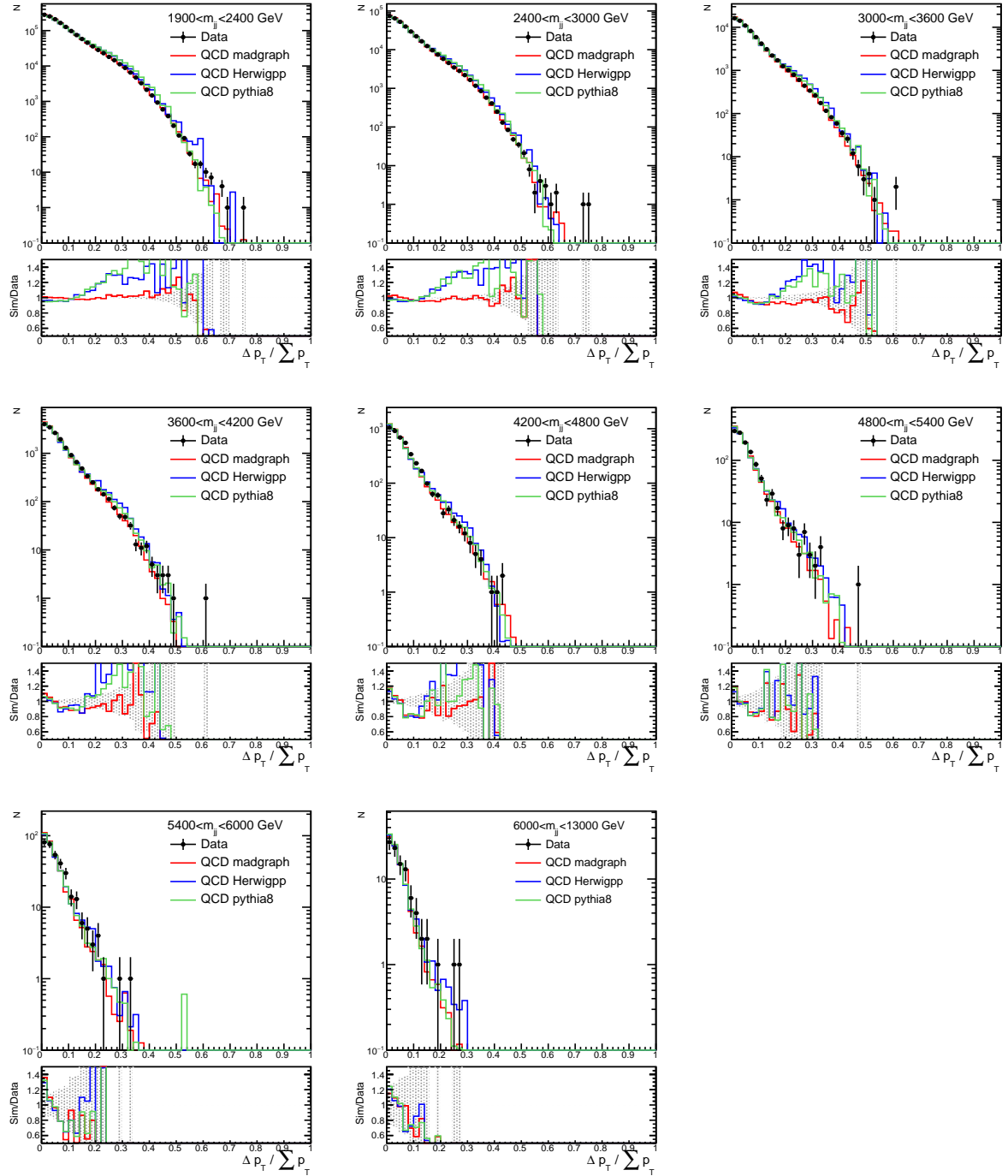


Figure 13: Comparisons of distributions in $\frac{p_{T,1} - p_{T,2}}{p_{T,1} + p_{T,2}}$ between data (points) and simulation (histograms).

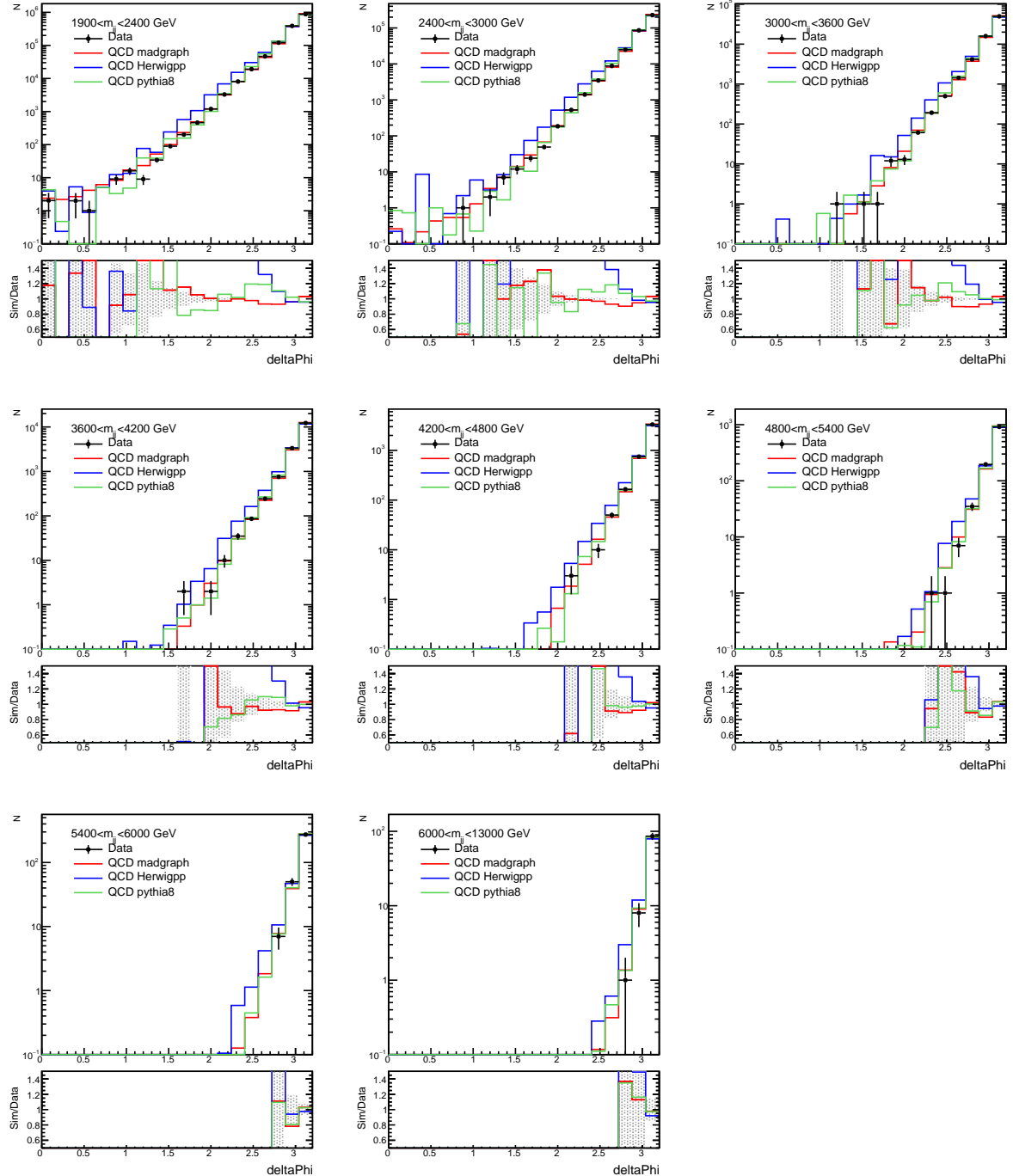


Figure 14: Comparisons of distributions in $\Delta\phi_{1,2}$ between data (points) and simulation (histograms).

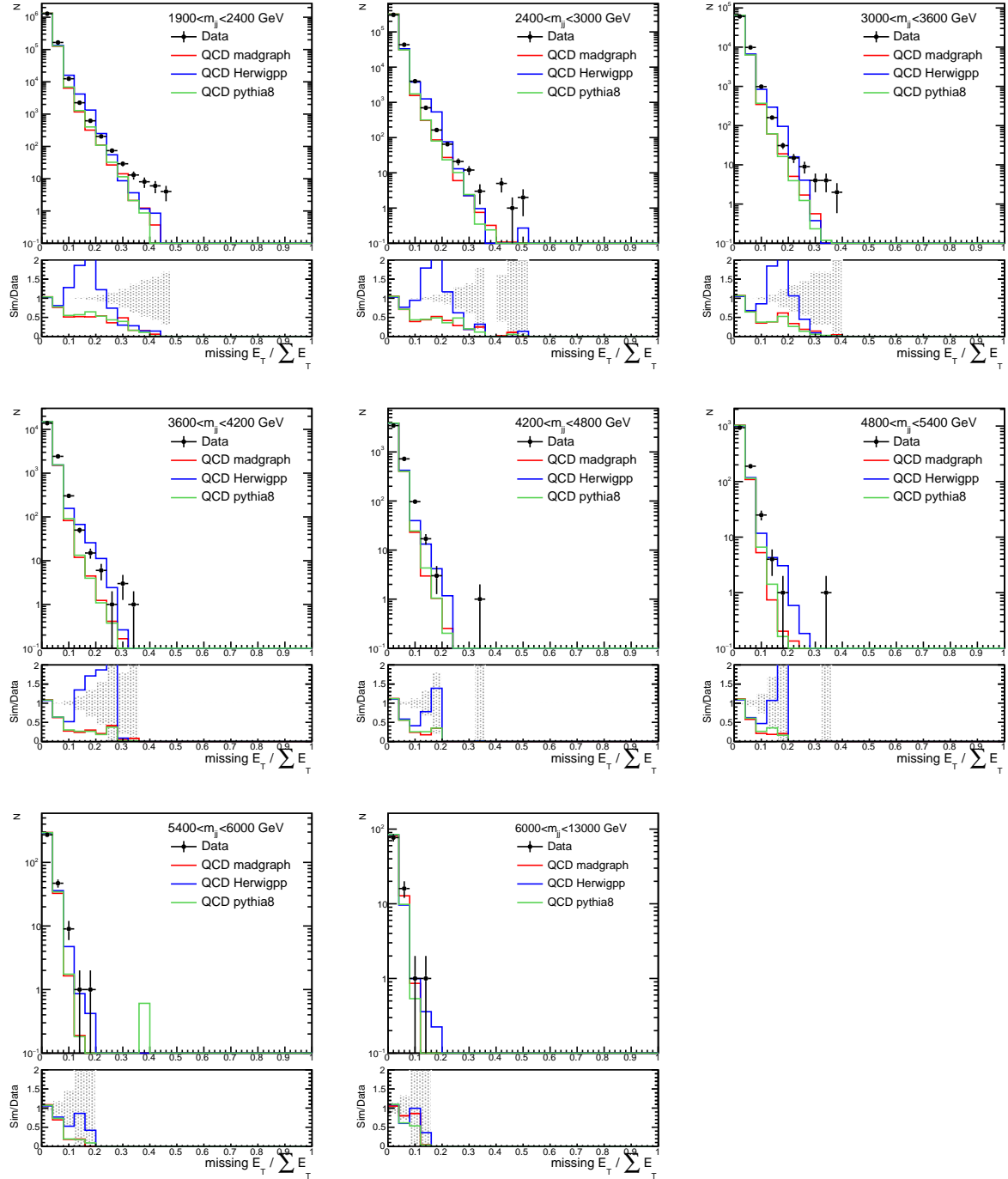


Figure 15: Comparisons of distributions in $E_T^{\text{miss}} / \sum E_T$ between data (points) and simulation (histograms).

216 4.4 Detector Effects and Unfolding

217 In this section, we investigate the effects of the imperfect detector measurements on the dijet
 218 angular distributions. The largest effects are expected to come from jet energy resolution, which
 219 arise primarily from energy fluctuations due to electronic noise, pile-up, energy sampling, and
 220 from non-uniformities and non-linearities in the detector response, and jet position resolution.

221 In Figure 16, Figure 17, Figure 18, Figure 19, Figure 20 and Figure 21 the jet p_T resolution from
 222 energy-corrected particle-flow jets from the full detector simulation and those from particle-
 223 level jets that were smeared in energy according to resolution functions that were derived by
 224 the JetMET POG [53, 57, 58] is shown in 6 different rapidity ranges. Two parametrizations
 225 of the detector resolution are compared, one with a simple Gaussian function and another
 226 with a double-sided Crystal-Ball function which adds tails to the Gaussian core resolution.
 227 The core and high end tail resolution for response values in rapidity range $0.5 < y < 1.0$ are
 228 well described by Gaussian and Crystal-Ball parameterizations. However, for response values
 229 in rapidity range $1.0 < y < 1.5$, $1.5 < y < 1.8$, $1.8 < y < 2.1$, and $2.1 < y < 2.5$, the
 230 parameterizations tend to have narrower cores than those derived from full simulation and for
 231 response values in rapidity range $0 < y < 0.5$, the parameterization tend to have wider cores
 232 than those from derived from full simulation. This may be expected as the parameters for the
 233 response functions were determined in Run 1 and for AK5 jets. To better describe the widths
 234 of the response observed in simulation, the width of the Gaussian were increased (decreased)
 235 by 10 – 30% (up to 5%), depending upon the generated jet p_T and y . The smeared jet p_T
 236 resolution in rapidity range with $0 < y < 0.5$, $1.0 < y < 1.5$, $1.5 < y < 1.8$, $1.8 < y < 2.1$, and
 237 $2.1 < y < 2.5$ with the updated parameterizations are shown in Figure 22, Figure 23, Figure 24,
 238 Figure 25 and Figure 26. The agreement is substantially improved. The low end tails has no
 239 impact on the analysis due to the steeply falling dijet mass spectrum. The jet p_T resolution
 240 parameterizations in this analysis are similar to those for the 2015 analysis. A comparison
 241 of the jet p_T resolutions from 76x simulation (which are used for the 2015 analysis) and 80x
 242 simulation (which are used for this analysis) are shown in Figure 27.

243 In Figures 28 and 29, the dijet angular distributions from the GEANT simulation, Gaussian and
 244 Crystal-Ball parametrization are compared and found to be in good agreement, indicating that
 245 the bulk of the detector effects on the dijet angular distribution can be attributed to jet energy
 246 smearing.

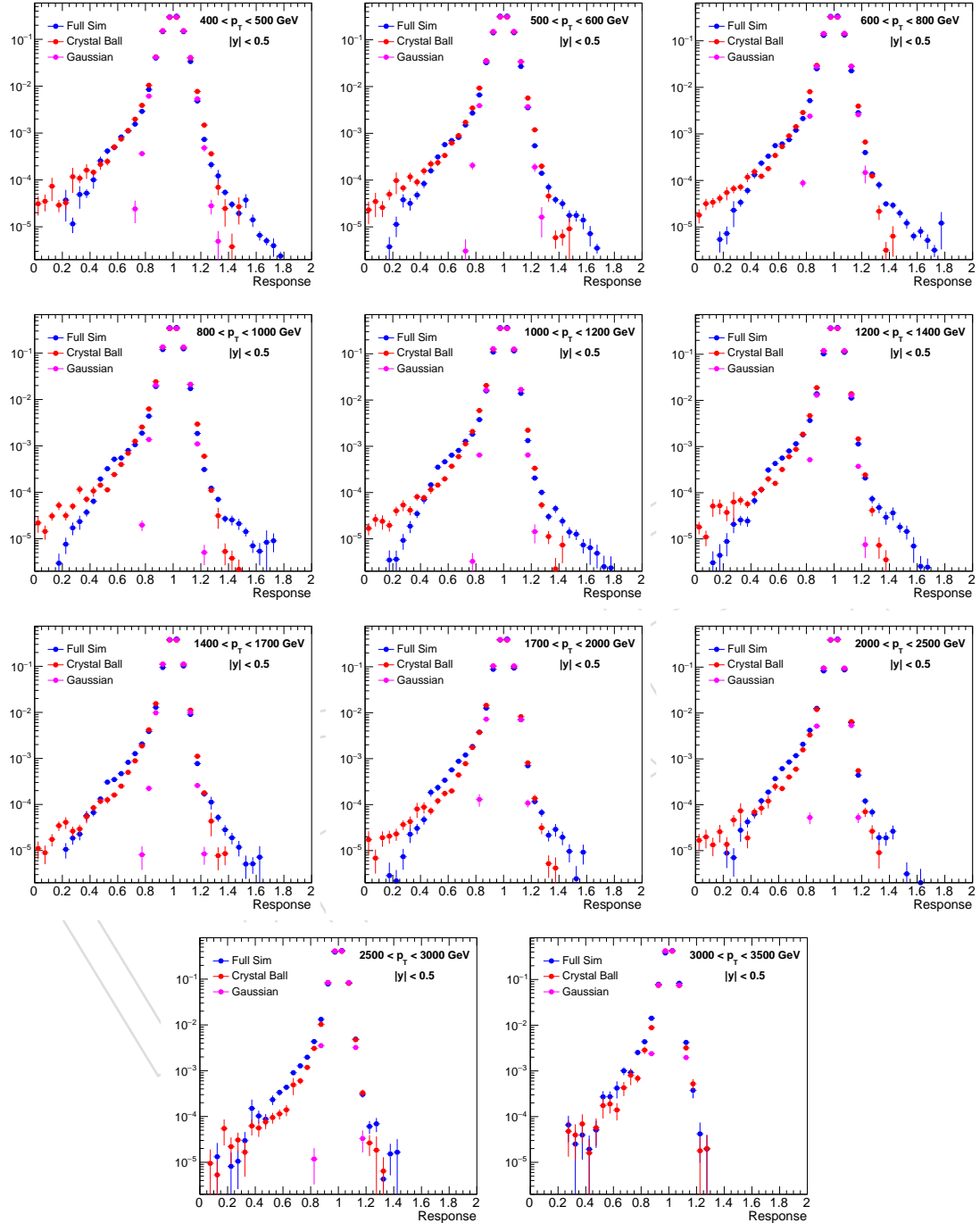


Figure 16: Jet p_T response from the GEANT detector simulation compared to the response from generated jets smeared with the default Gaussian and Crystal-Ball parametrizations in $0 < y < 0.5$ for several bins in jet p_T .

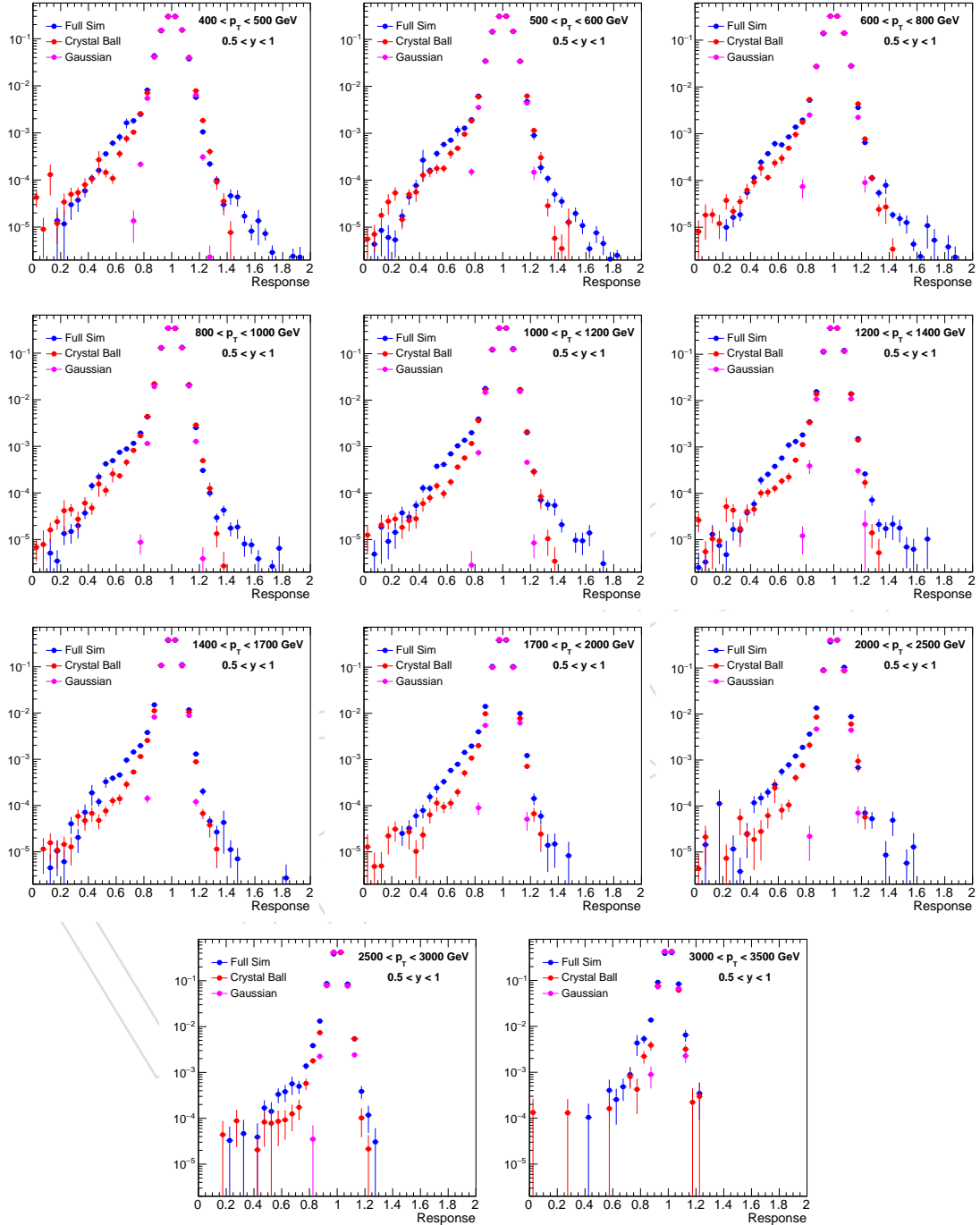


Figure 17: Jet p_T response from the GEANT detector simulation compared to the response from generated jets smeared with the default Gaussian and Crystal-Ball parametrizations in $0.5 < y < 1$ for several bins in jet p_T .

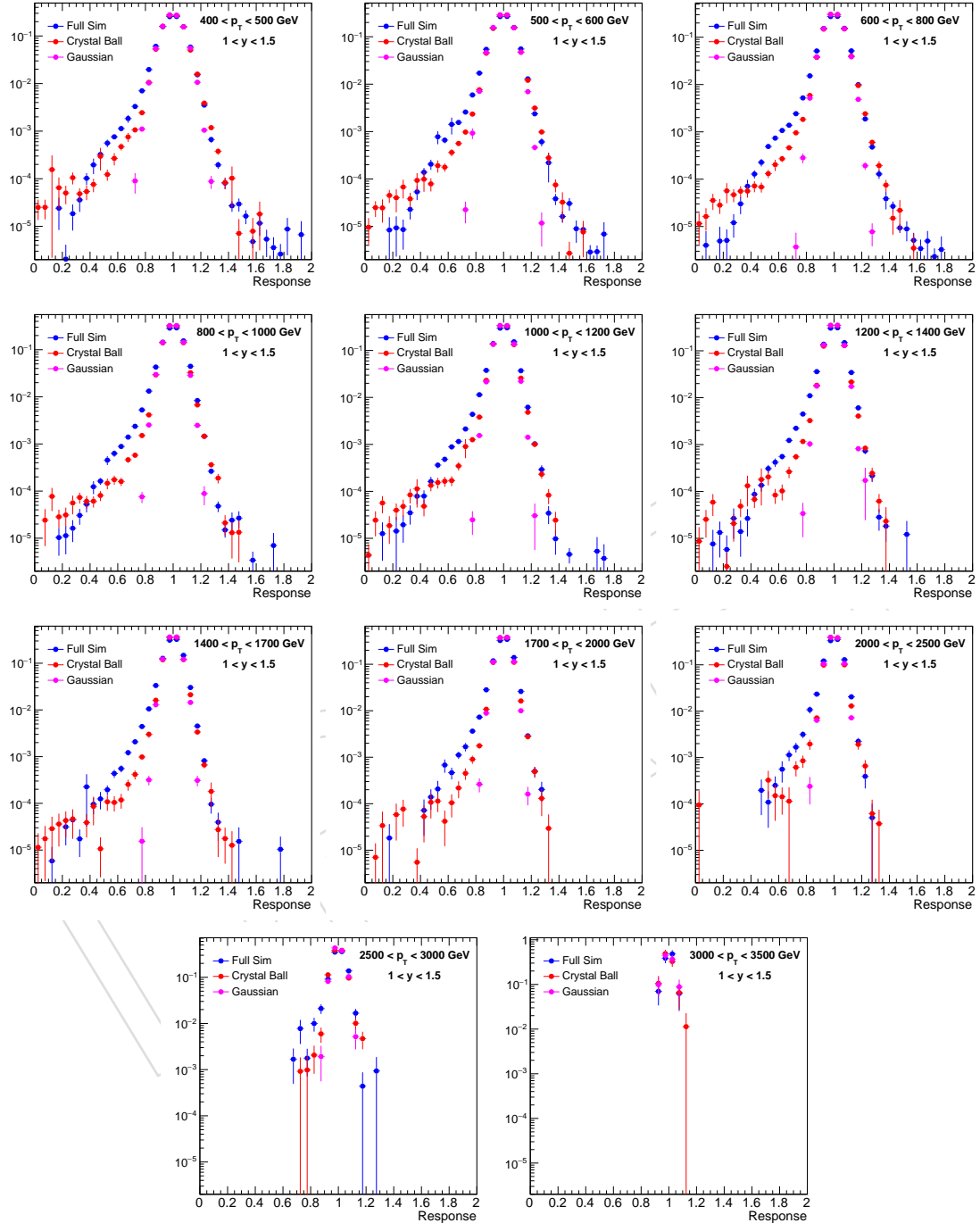


Figure 18: Jet p_T response from the GEANT detector simulation compared to the response from generated jets smeared with the default Gaussian and Crystal-Ball parametrizations in $1 < y < 1.5$ for several bins in jet p_T .

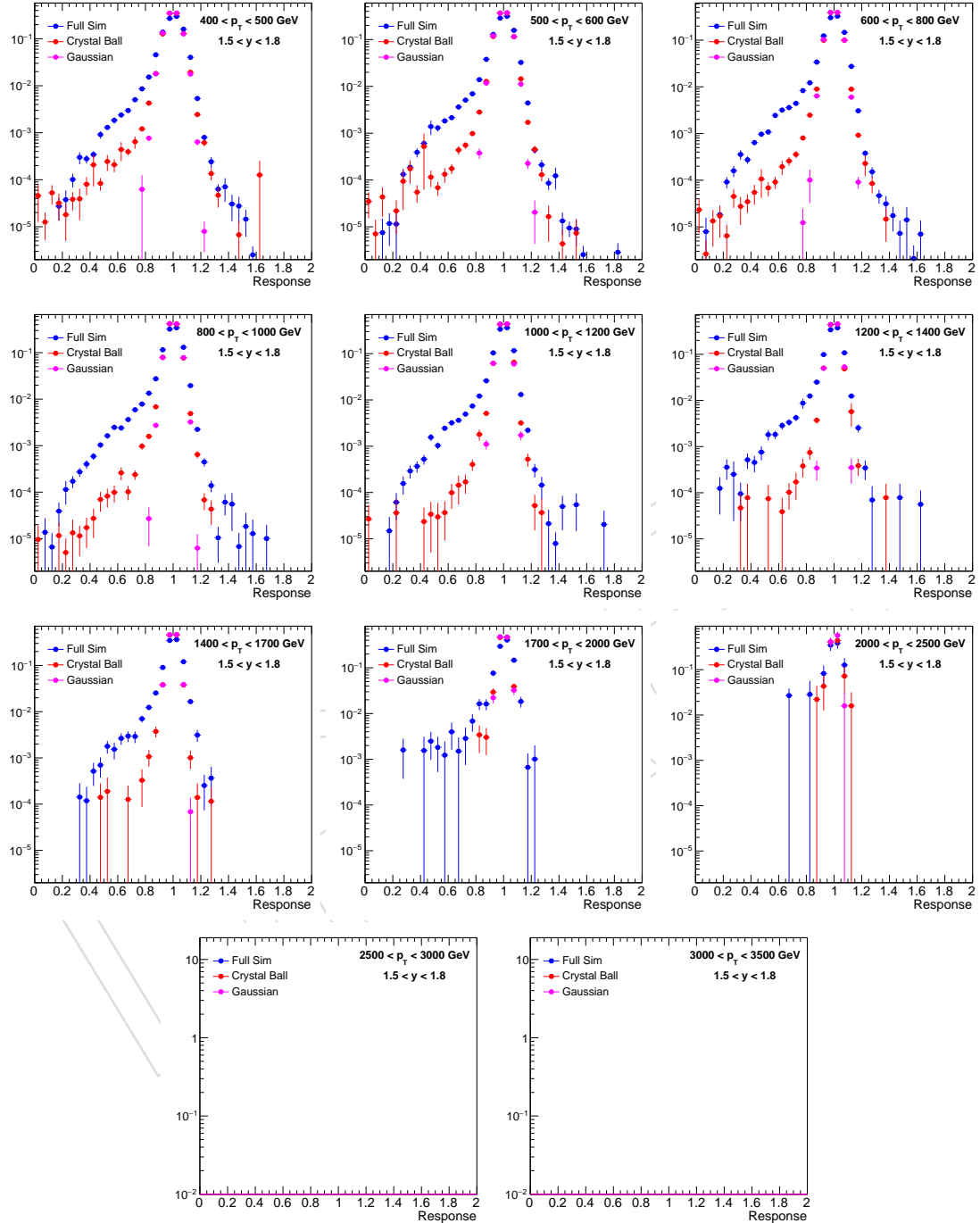


Figure 19: Jet p_T response from the GEANT detector simulation compared to the response from generated jets smeared with the default Gaussian and Crystal-Ball parametrizations in $1.5 < y < 1.8$ for several bins in jet p_T .

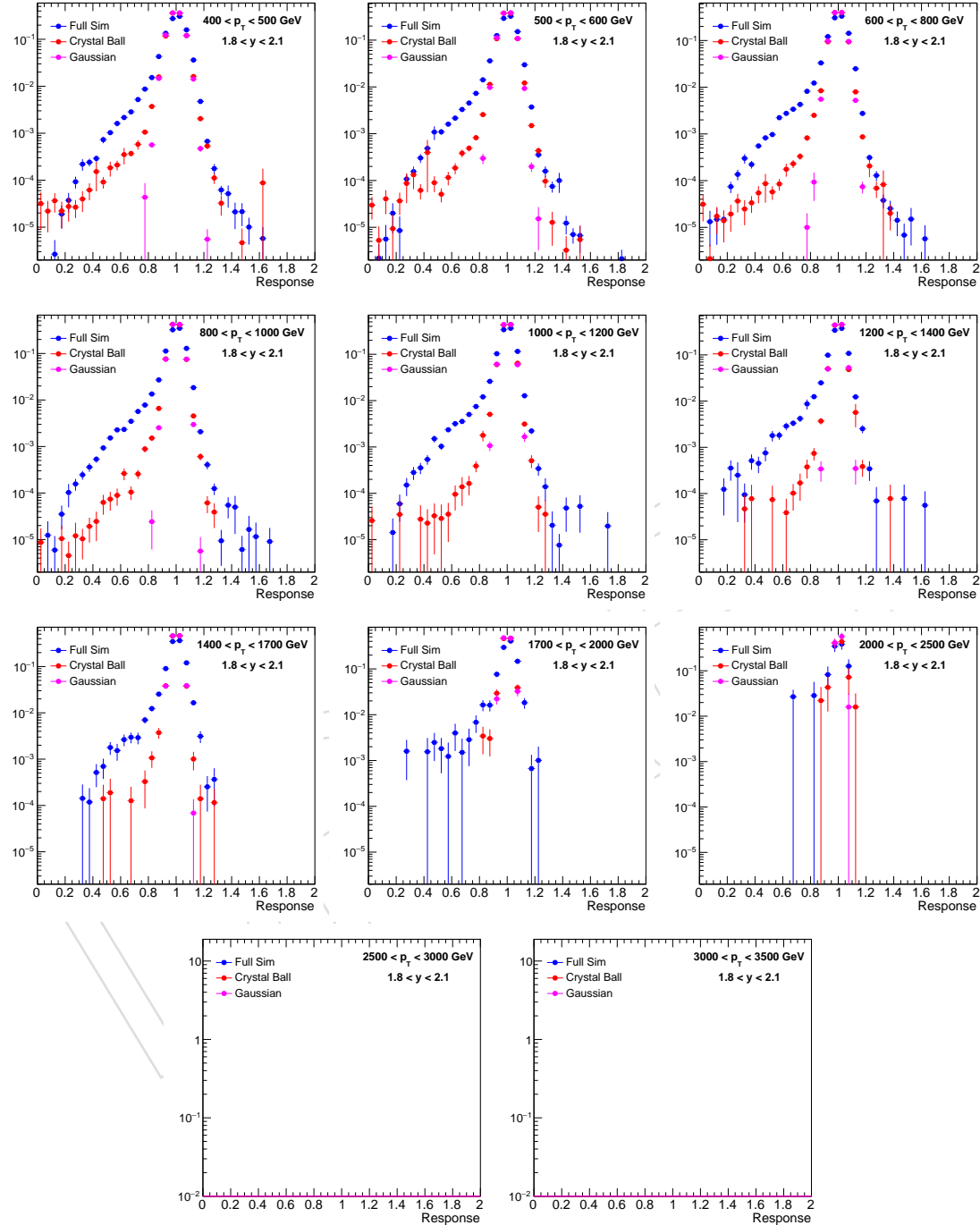


Figure 20: Jet p_T response from the GEANT detector simulation compared to the response from generated jets smeared with the default Gaussian and Crystal-Ball parametrizations in $1.8 < y < 2.1$ for several bins in jet p_T .

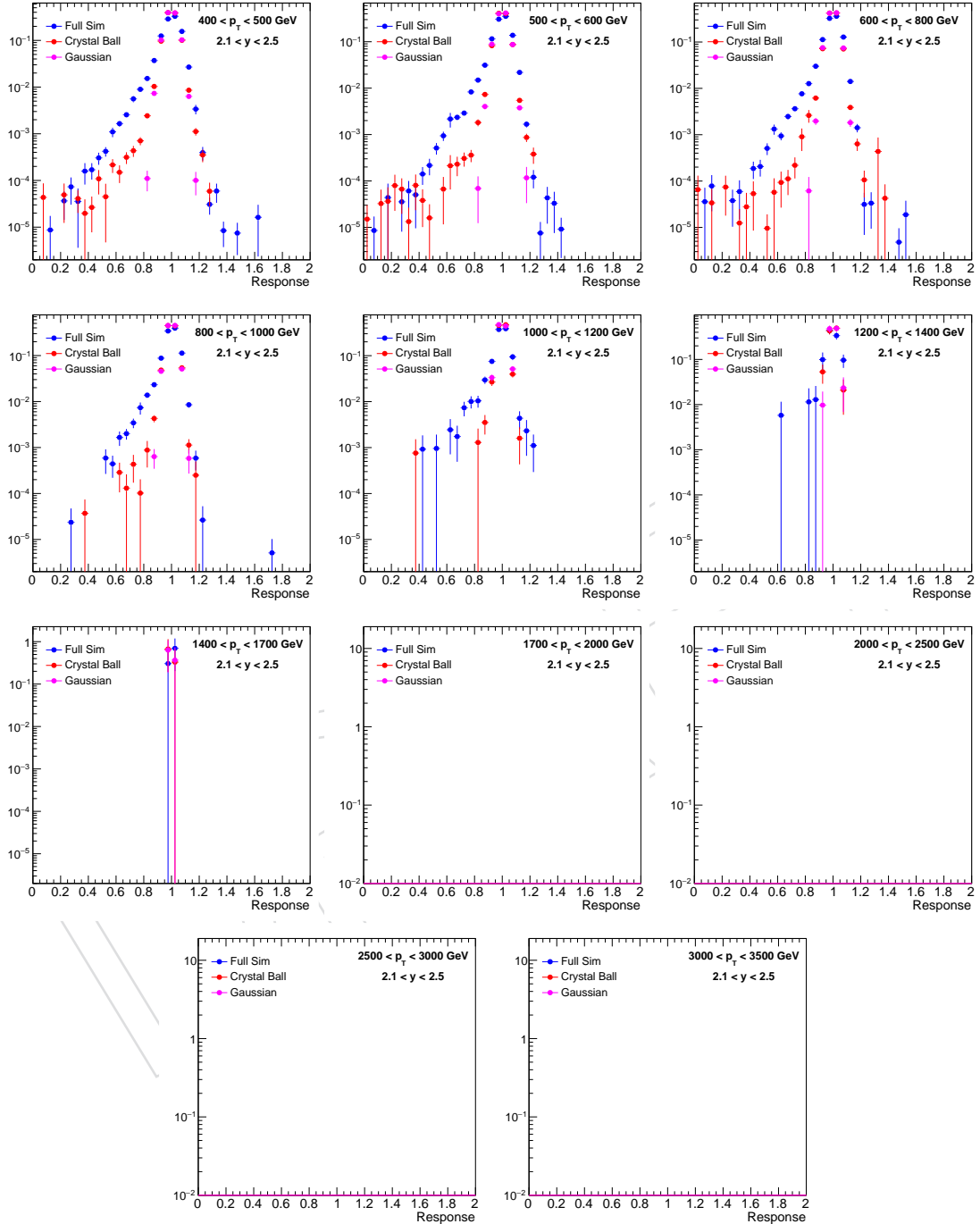


Figure 21: Jet p_T response from the GEANT detector simulation compared to the response from generated jets smeared with the default Gaussian and Crystal-Ball parametrizations in $2.1 < y < 2.5$ for several bins in jet p_T .

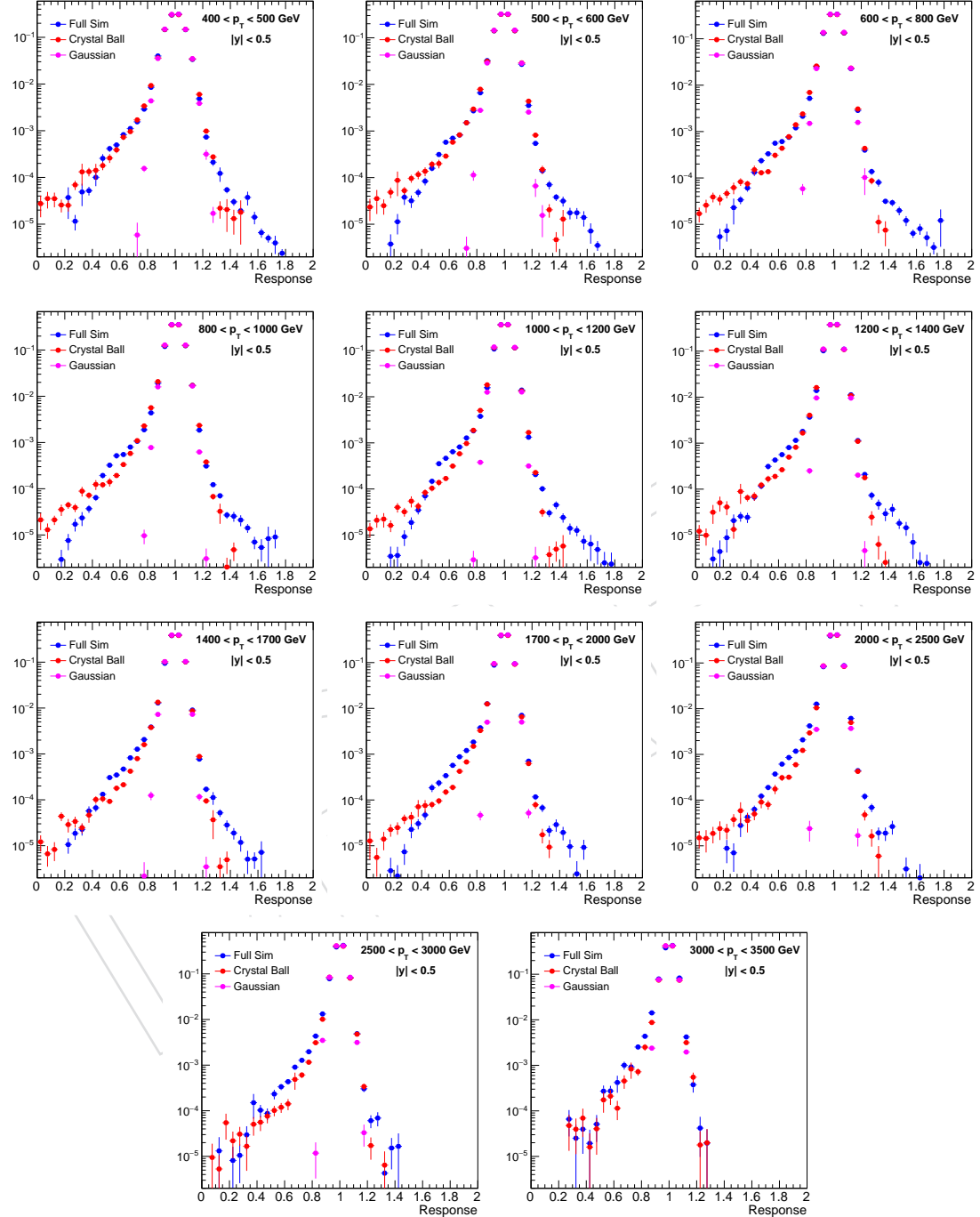


Figure 22: Same as Figure 16 but with additional scale factor added on top of the Gaussian widths.

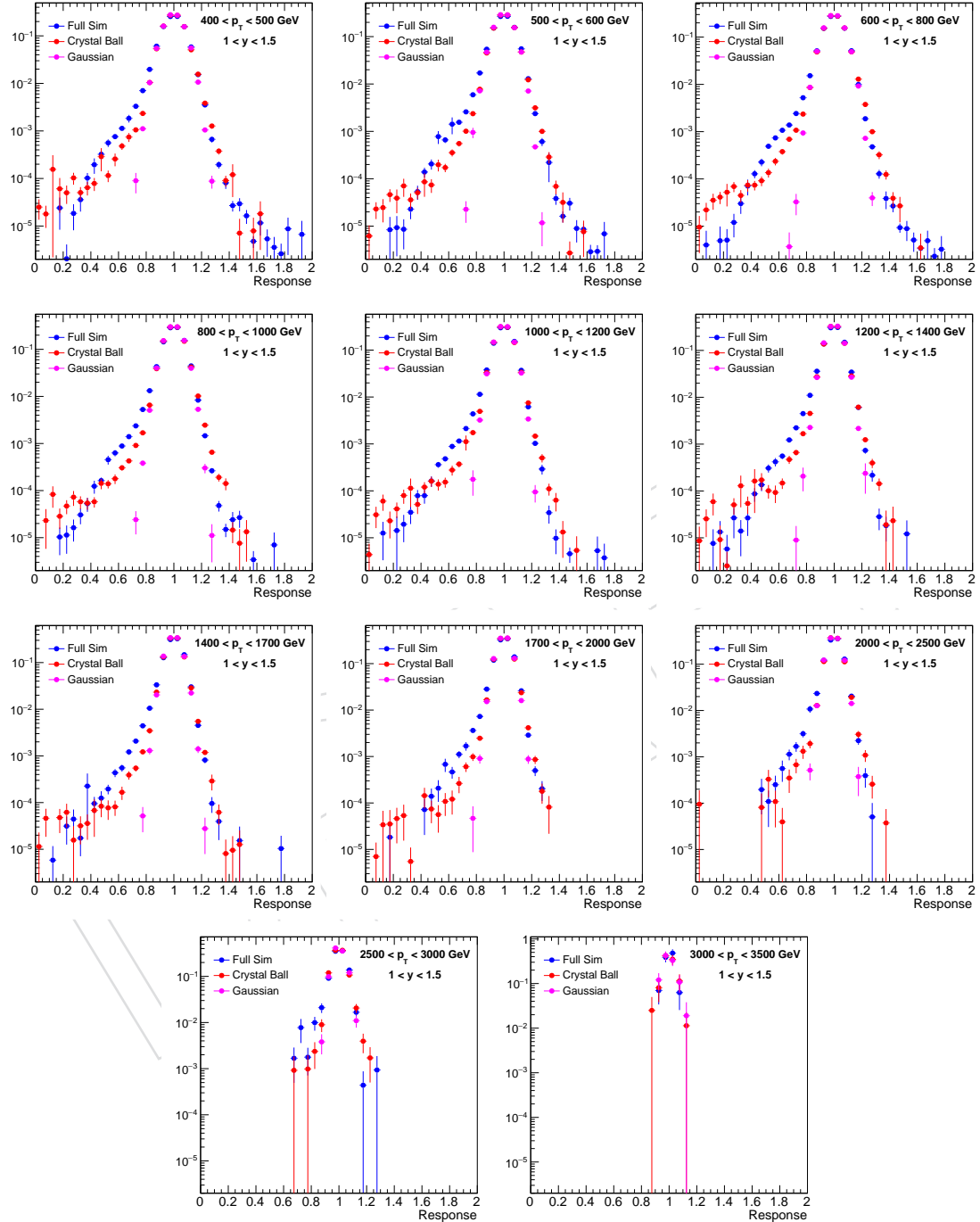


Figure 23: Same as Figure 18 but with additional scale factor added on top of the Gaussian widths.

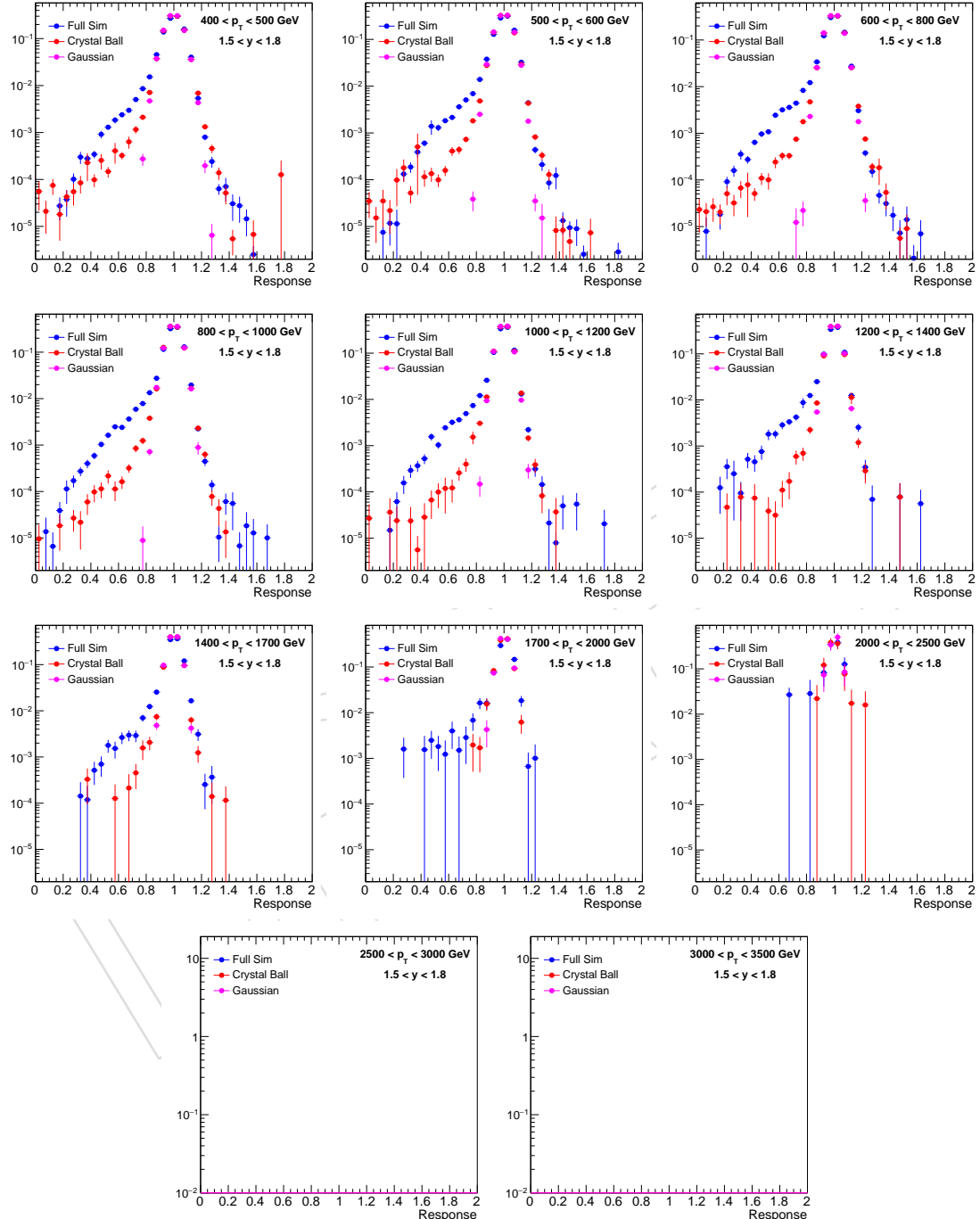


Figure 24: Same as Figure 19 but with additional scale factor added on top of the Gaussian widths.

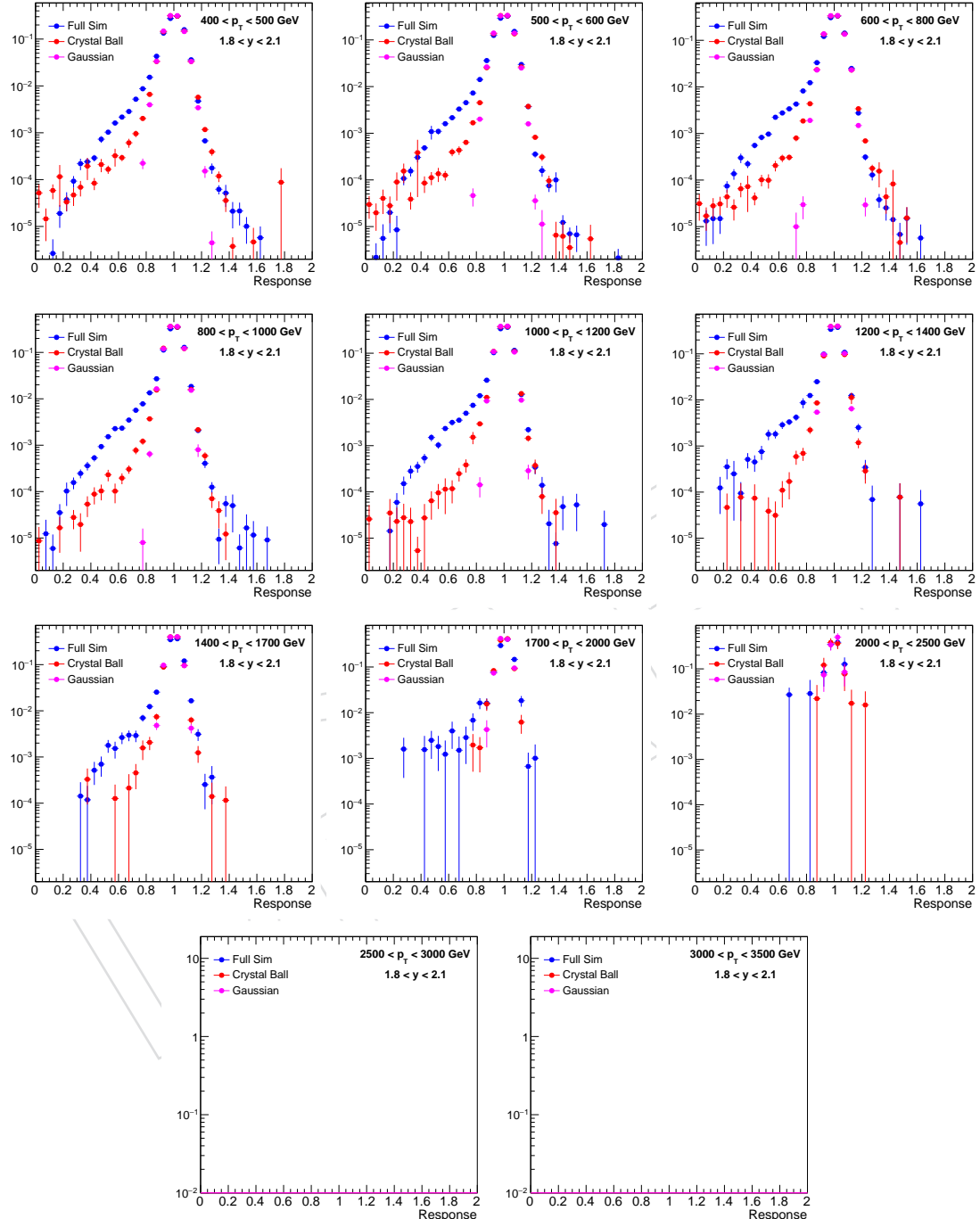


Figure 25: Same as Figure 20 but with additional scale factor added on top of the Gaussian widths.

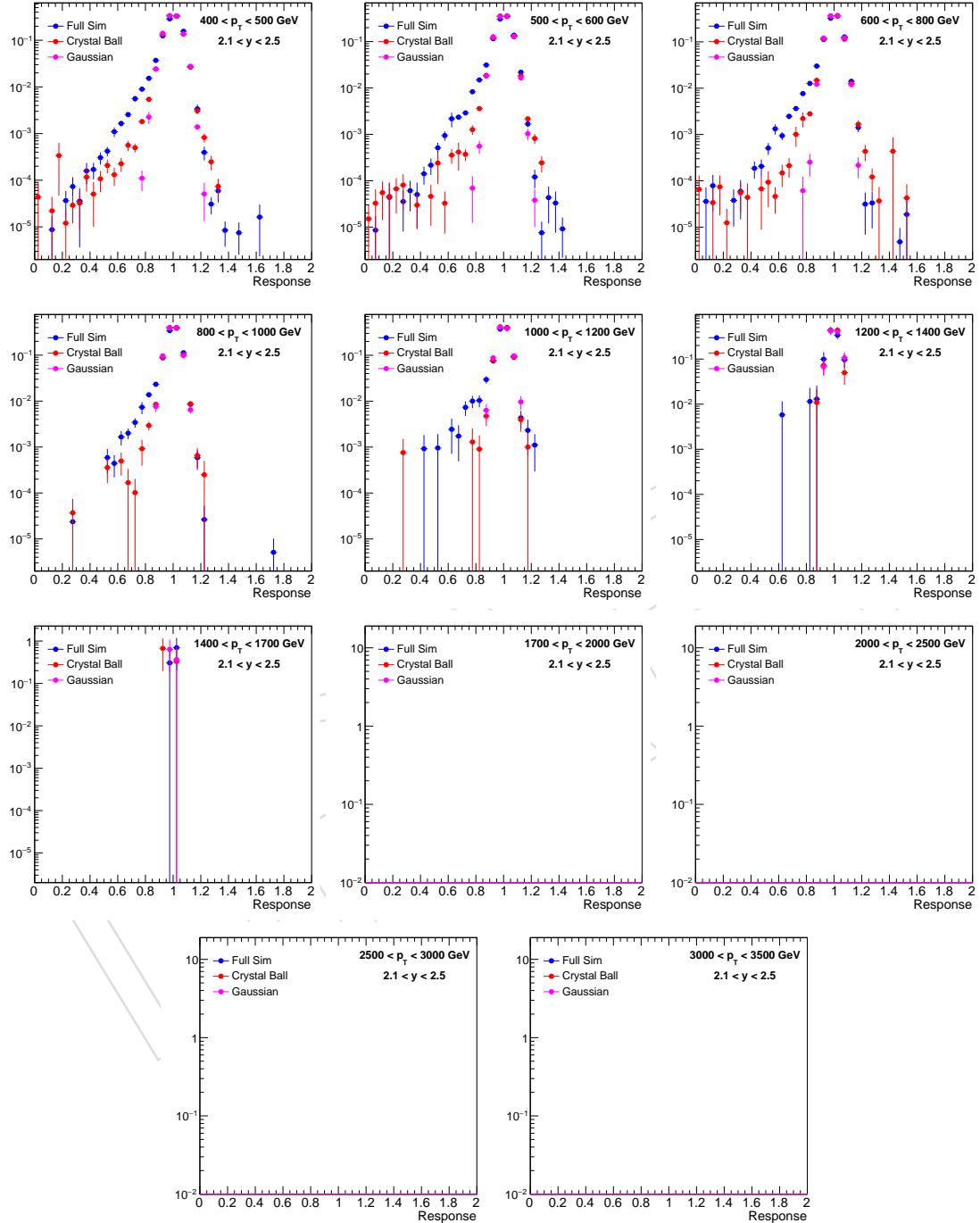


Figure 26: Same as Figure 21 but with additional scale factor added on top of the Gaussian widths.

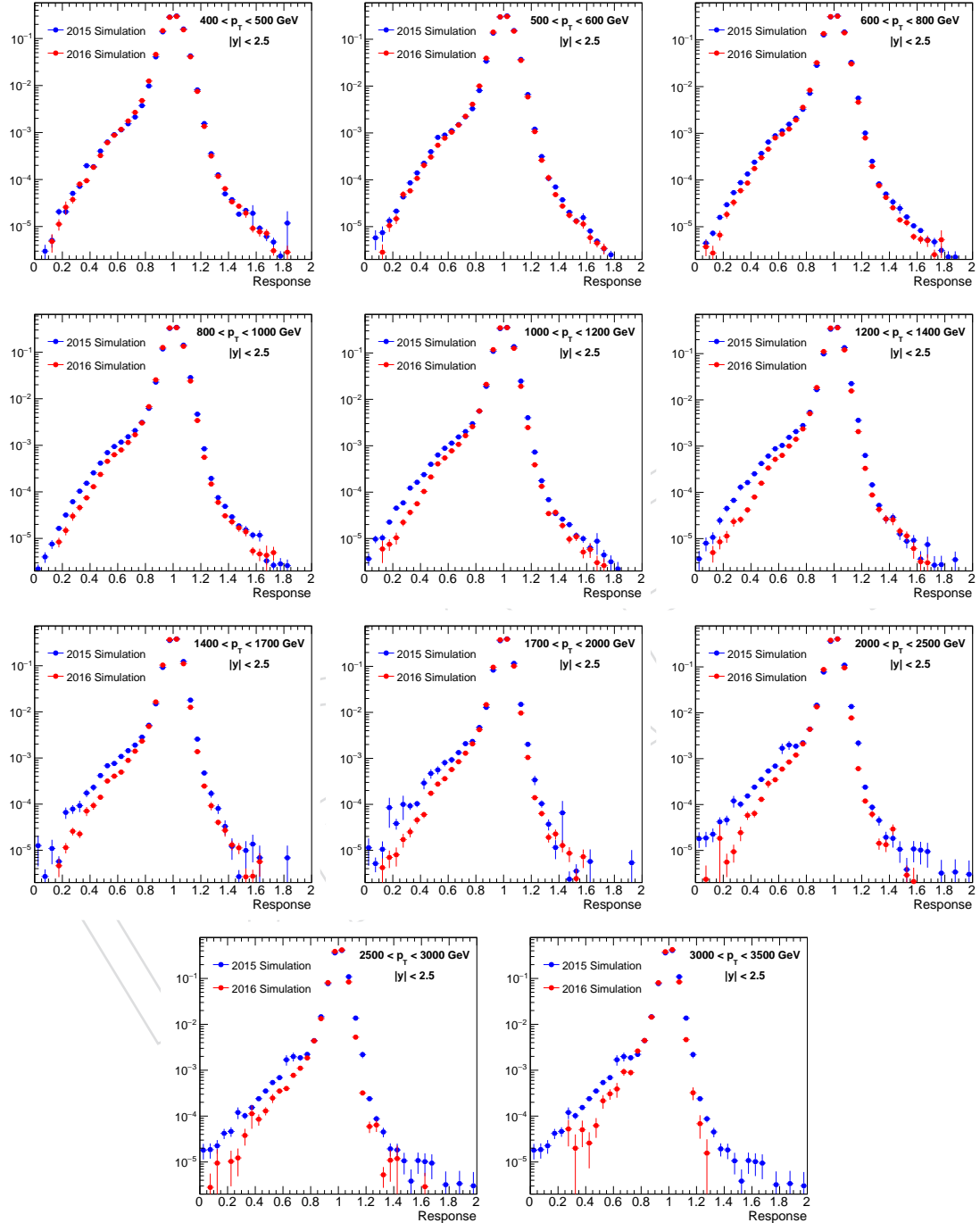


Figure 27: Comparison of the jet p_T resolutions from 76x simulation and 80x simulation.

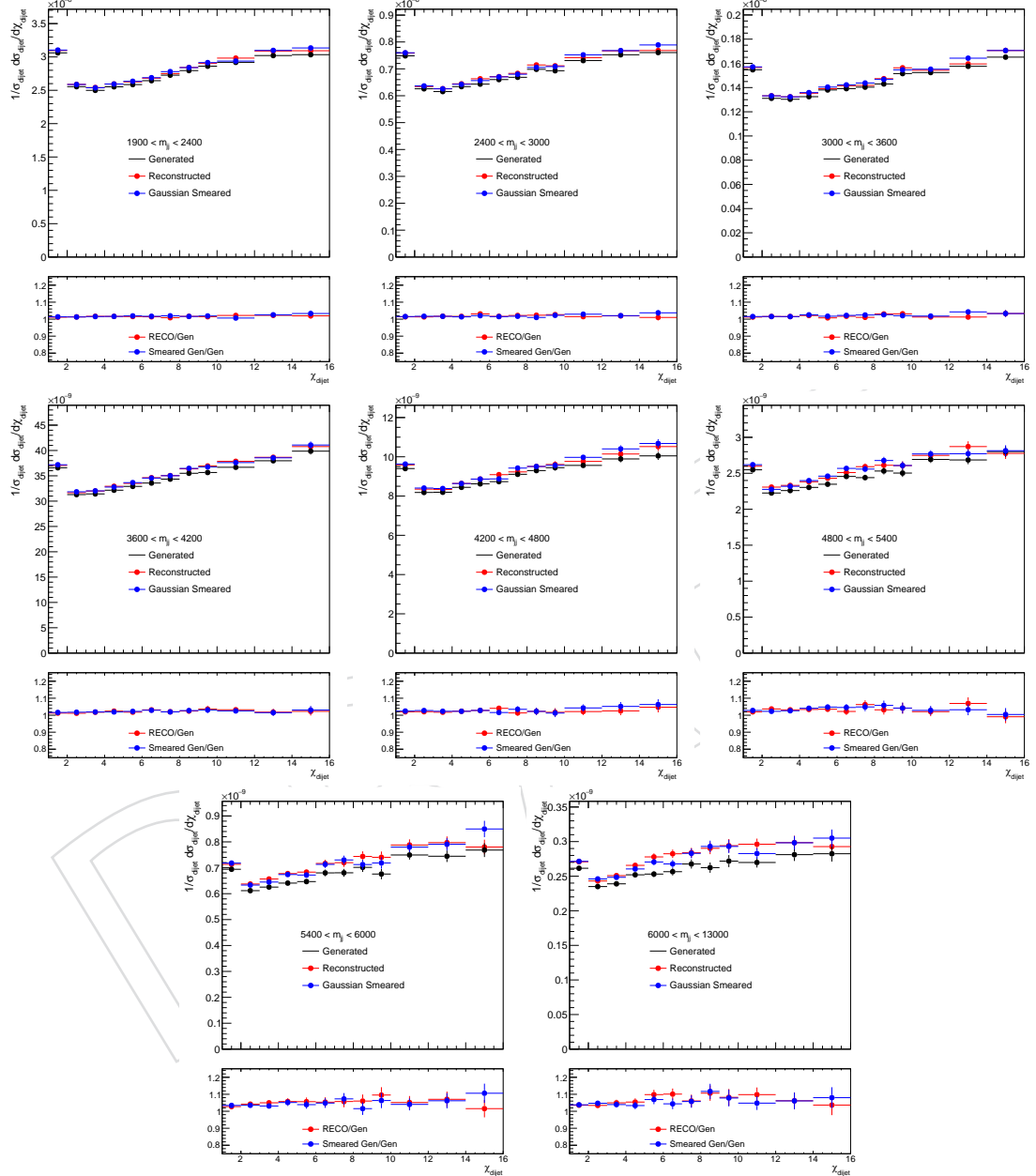


Figure 28: Dijet angular distributions (χ_{dijet}) from generated jets smeared with a Gaussian compared to those from JES-corrected particle-flow jets from the GEANT full simulation.

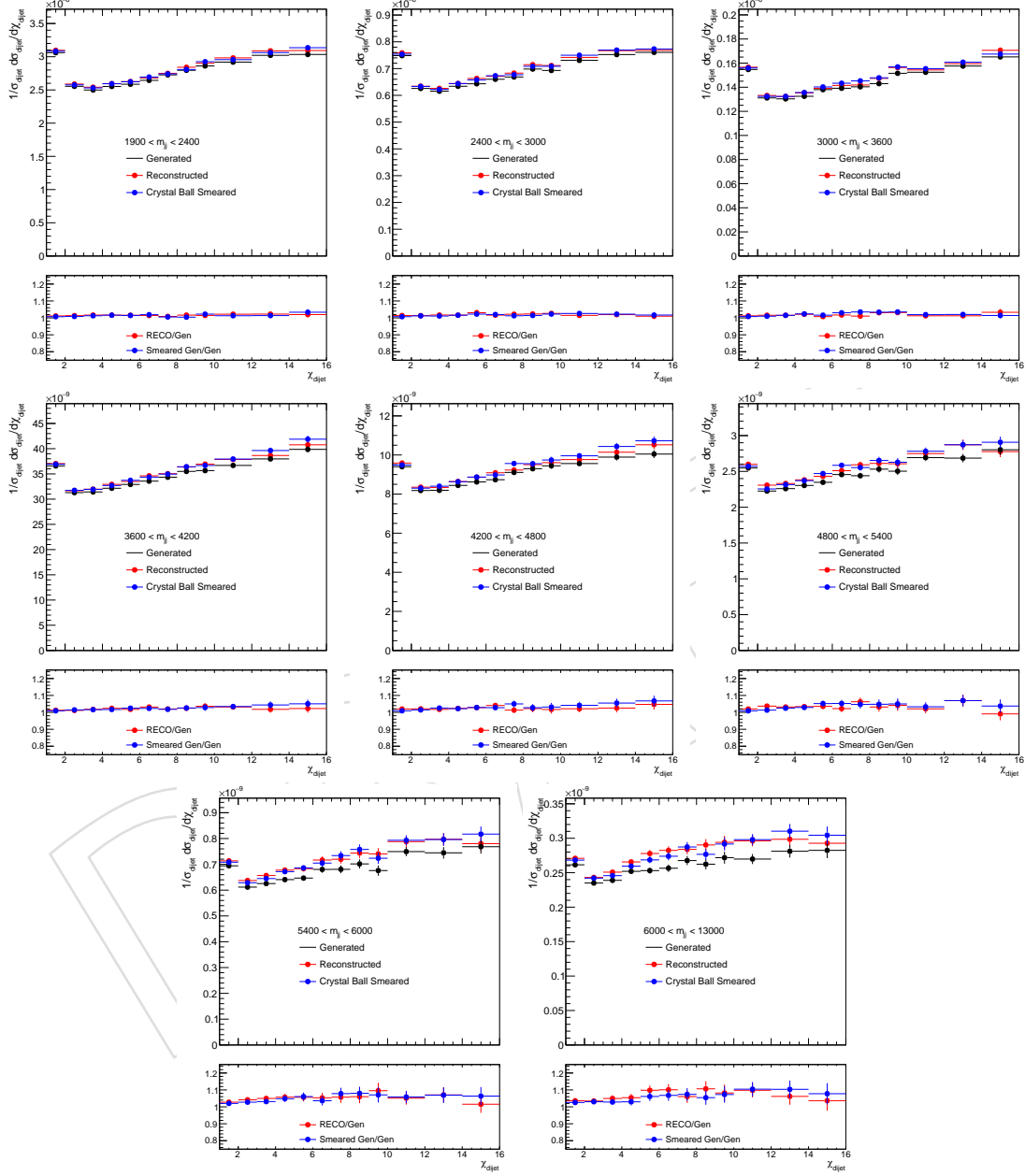


Figure 29: Dijet angular distributions (χ_{dijet}) from generated jets smeared with a Crystal-Ball compared to those from JES-corrected particle-flow jets from the GEANT full simulation.

- 247 The measured χ_{dijet} distributions were corrected for migration effects due to the finite jet p_T
248 resolution of the detector. Fluctuations in the jet response can cause event migrations between
249 bins in χ_{dijet} as well as in between bins of dijet mass, as fluctuations in the jet response can cause
250 low energy jets to be misidentified as leading jets. We therefore perform a two dimensional
251 unfolding in dijet mass and χ_{dijet} using a simple matrix inversion method implemented in the
252 RooUnfold package [59]. The matrix inversion procedure does not have any regularization. We
253 therefore perform the unfolding procedure using a iterative D'Agostini method [60] as a cross-
254 check. The iterative procedure is regularised by the number of iterations, which is set to four.
255 We find the difference between the matrix inversion unfolded distribution and the D'Agostini
256 method unfolded distribution are smaller than 5%.
- 257 The response matrix used for the unfolding was filled using particle-level jets that were gener-
258 ated using Pythia8 with large statistics and smeared using the double-sided Crystal-Ball func-
259 tion described earlier. The χ_{dijet} distributions and the M_{jj} spectrum for this smeared large
260 statistics sample are compared with the data and the full simulated Pythia, Herwig and Mad-
261 graph samples. As shown in Figure 30 and Figure 31, the distributions for the smeared large
262 statistics sample describe the data well. Response matrices were also created using Gaussian-
263 smeared generated jets and reconstructed jets from the full simulation. These were used to help
264 determine the systematic uncertainties associated with the unfolding. The response matrix in-
265 cludes an additional lower mass bin 1.9-2.4 TeV to account for migrations from this mass bin
266 into the lowest mass bin of the analysis. As the trigger is not fully efficient in this mass range,
267 the data in this bin was corrected as a function of mass and χ_{dijet} using the efficiencies shown
268 in Figure 4.

DRAFT

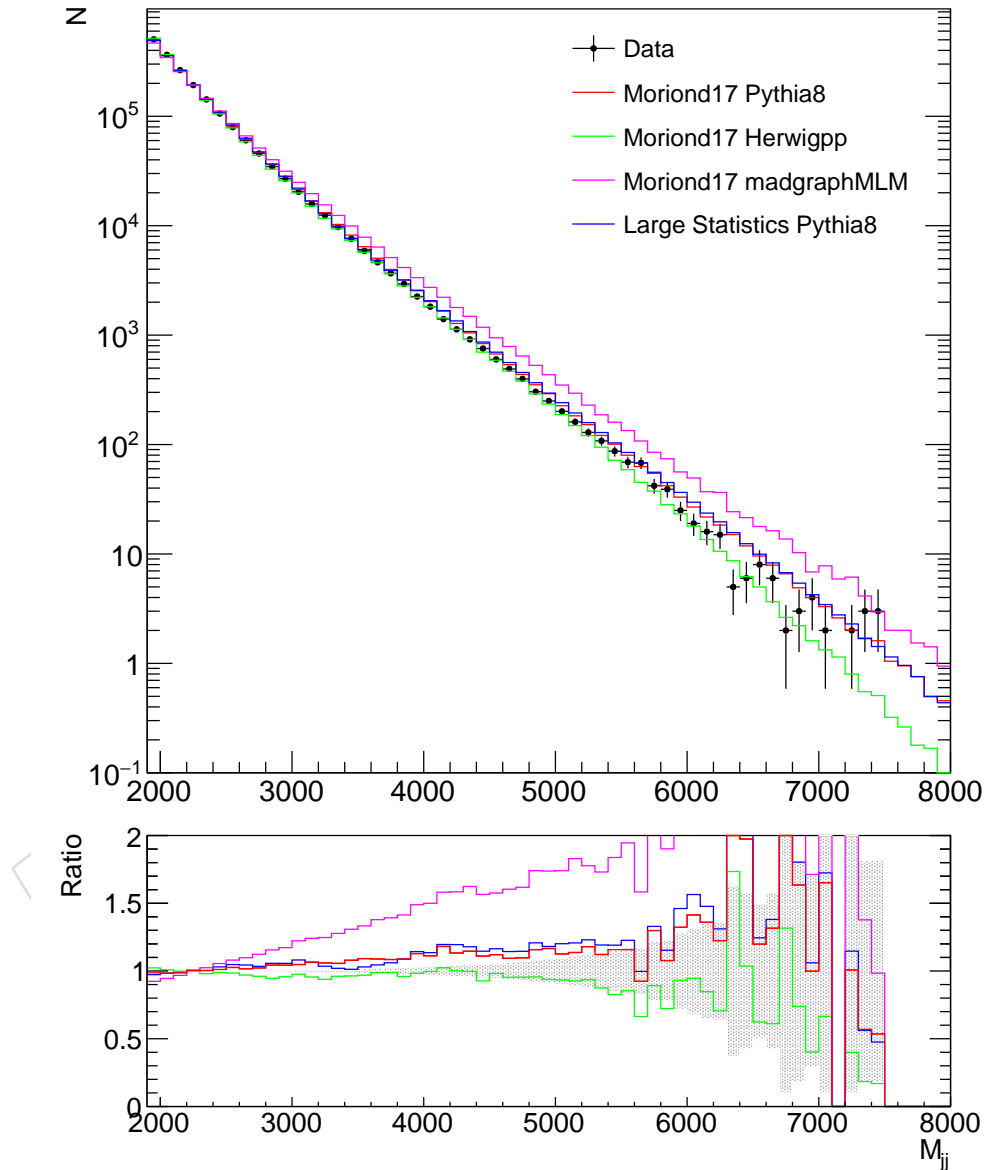


Figure 30: Comparisons of distributions in the dijet invariant mass between data (points) and the large statistics sample used to derive the response matrices.

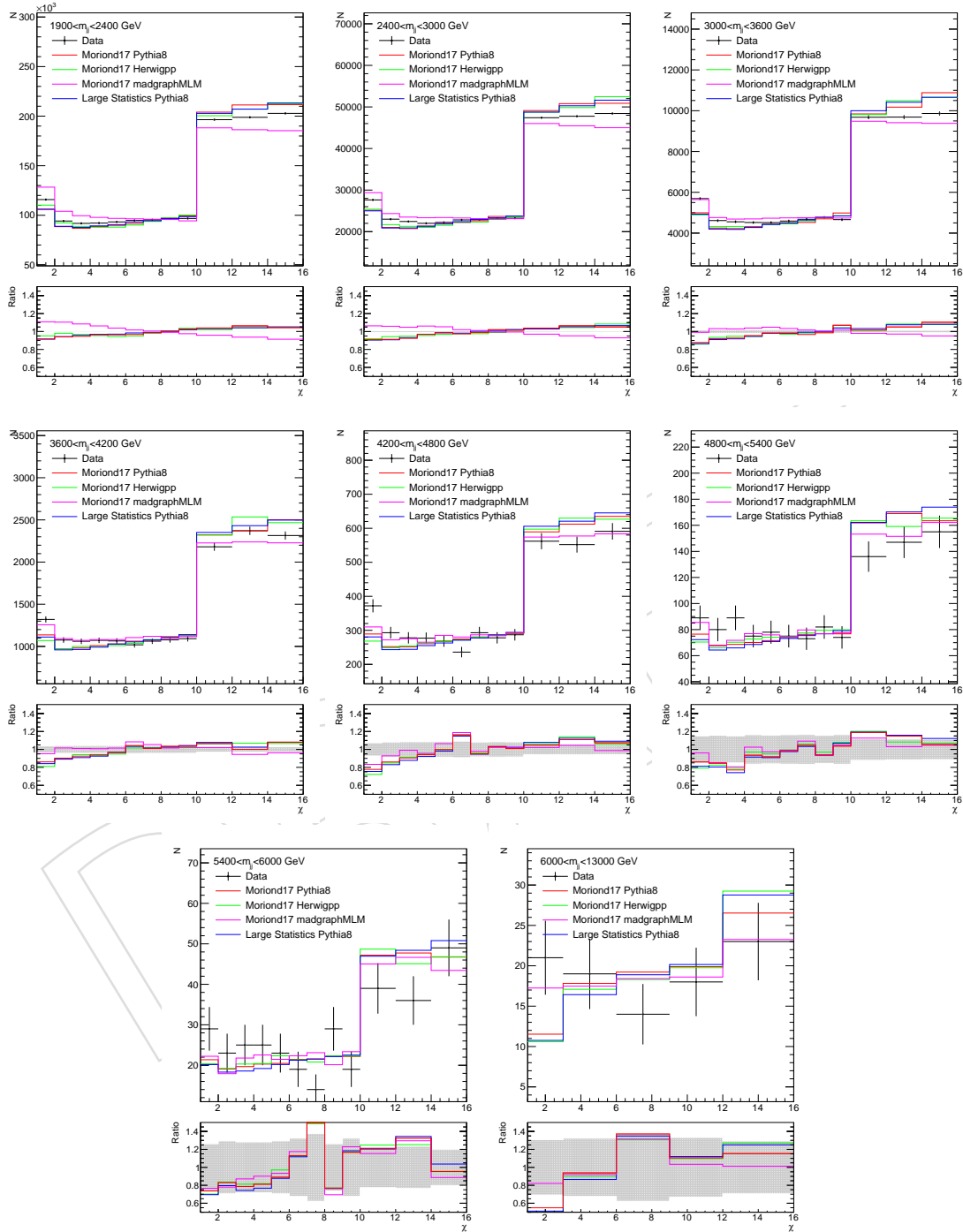


Figure 31: Comparisons of distributions in χ_{dijet} between data (points) and the large statistics sample used to derive the response matrices (histograms).

269 The jet energy resolution in data has been found to be worse than the resolution in MC. Detailed
 270 studies by the JetMET group show that the resolution is $\sim 6\%$ worse in the central region of the
 271 detector, and $\sim 13\%$ worse at $\eta = 2.5$. We therefore increased the width of the Gaussian-core
 272 in the Crystal-Ball parameterization by the measured data/MC scale factors when determining
 273 the final response matrix used in the unfolding. Figure 32 shows the response matrix as a
 274 function of dijet mass and integrated over χ_{dijet} .

275 A trivial closure test was performed by unfolding the same sample which was used to derive
 276 the response matrix with (trivially) perfect agreement as shown in Fig. 33. A closure test of
 277 the method was performed by splitting the simulated samples into independent training and
 278 testing samples. An unsmeering matrix was determined from the training sample and then
 279 used to unfold the χ_{dijet} distributions from the testing sample. The results from the closure test
 280 are shown in Fig. 34 and no significant discrepancies were observed.

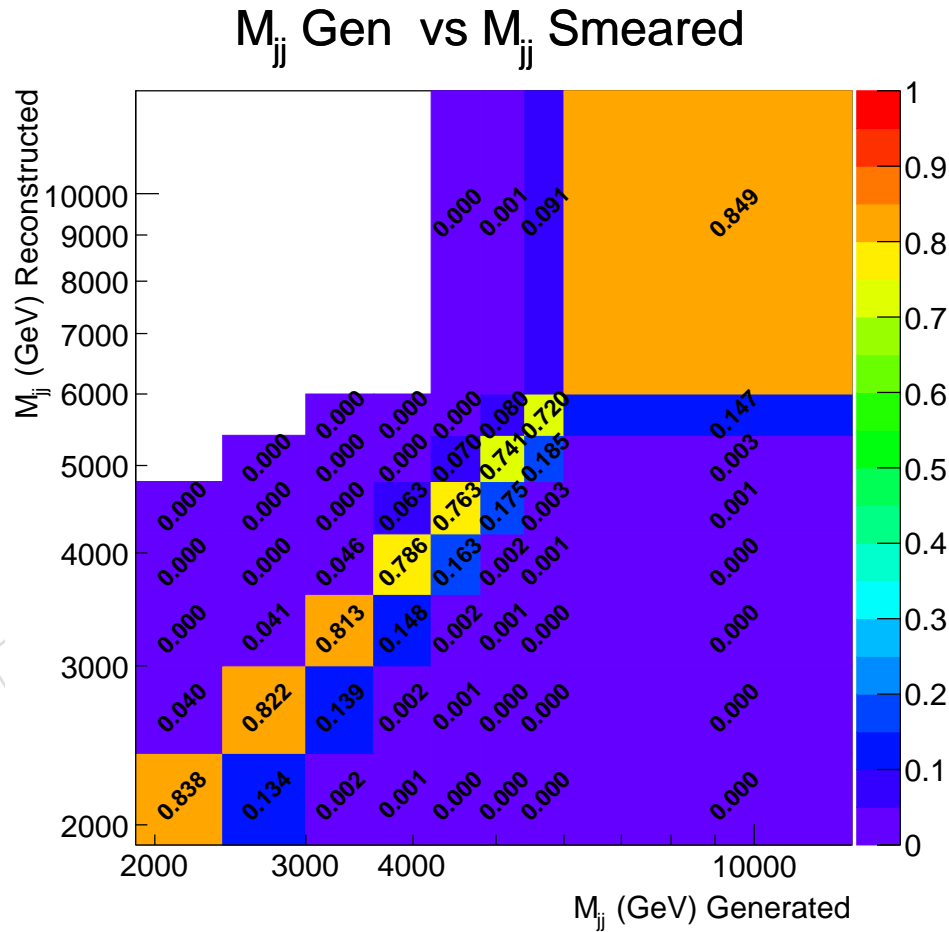


Figure 32: Response matrix from the Crystal-Ball parameterization of the jet energy resolution.

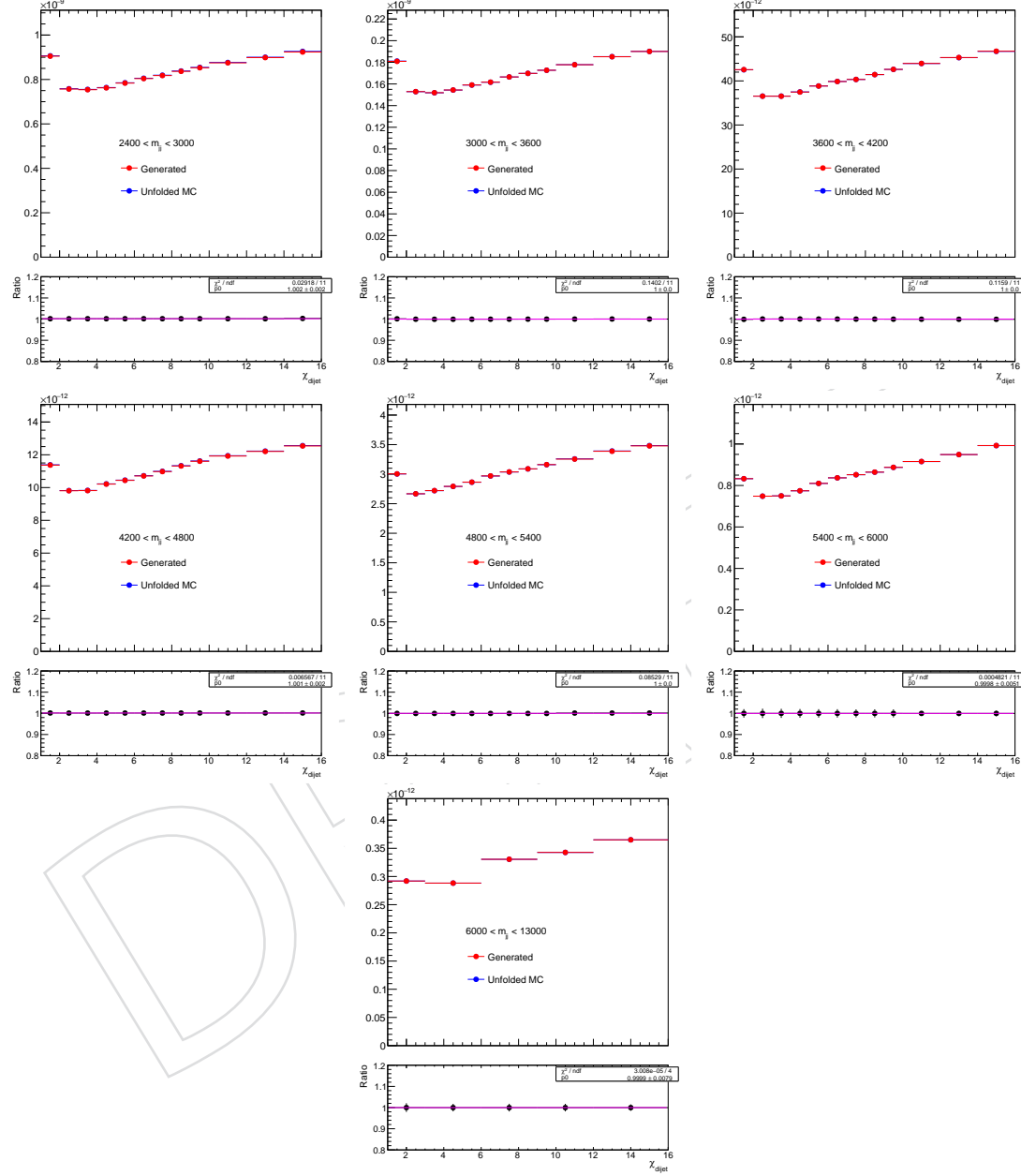


Figure 33: Comparisons of unfolded and generated χ_{dijet} distributions, where the unfolding correction was determined from the same MC sample. Also shown are the ratios of unfolded to generated χ_{dijet} distributions.

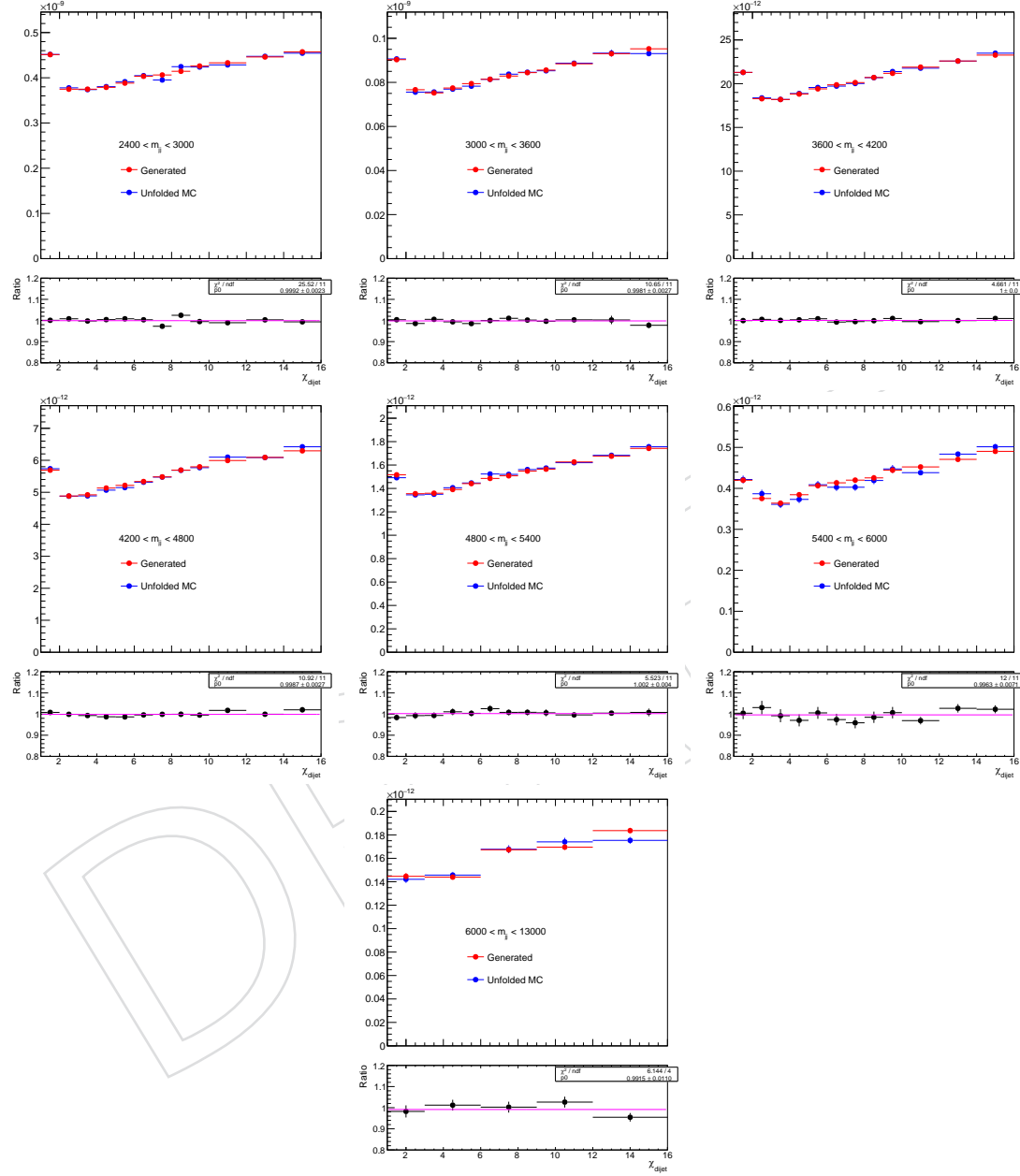


Figure 34: Comparisons of unfolded and generated χ_{dijet} distributions, where the unfolding correction was determined from an independent sample of events. Also shown are the ratios of unfolded to generated χ_{dijet} distributions.

- 281 Though a two dimensional unfolding procedure was performed, the magnitude of the correc-
282 tions can be understood from comparing the reconstructed and unfolded distributions in MC,
283 shown in Fig. 35.
- 284 Due to events migration between bins during the unfolding procedure, correlations of the sta-
285 tistical uncertainties between neighboring bins are included. In Fig. 36, we plot the fractional
286 statistical uncertainty of the data distribution before and after unfolding and observe an in-
287 crease due to the unfolding as expected. The covariance matrices for M_{jj} bins in each χ_{dijet} bin
288 are shown in Fig. 37. The corresponding correlation coefficients are shown in Fig. 38. The cor-
289 relation coefficient between χ_{dijet} bins are very small such that the correlations between χ_{dijet}
290 bins are negligible.
- 291 A comparison between the raw and unfolded data distributions are shown in Fig 39. The
292 unfolding correction factors change the shape of the χ_{dijet} distributions by less than 1% across
293 χ_{dijet} in the lowest M_{jj} range and less than 8% across χ_{dijet} in the highest M_{jj} range.

DRAFT

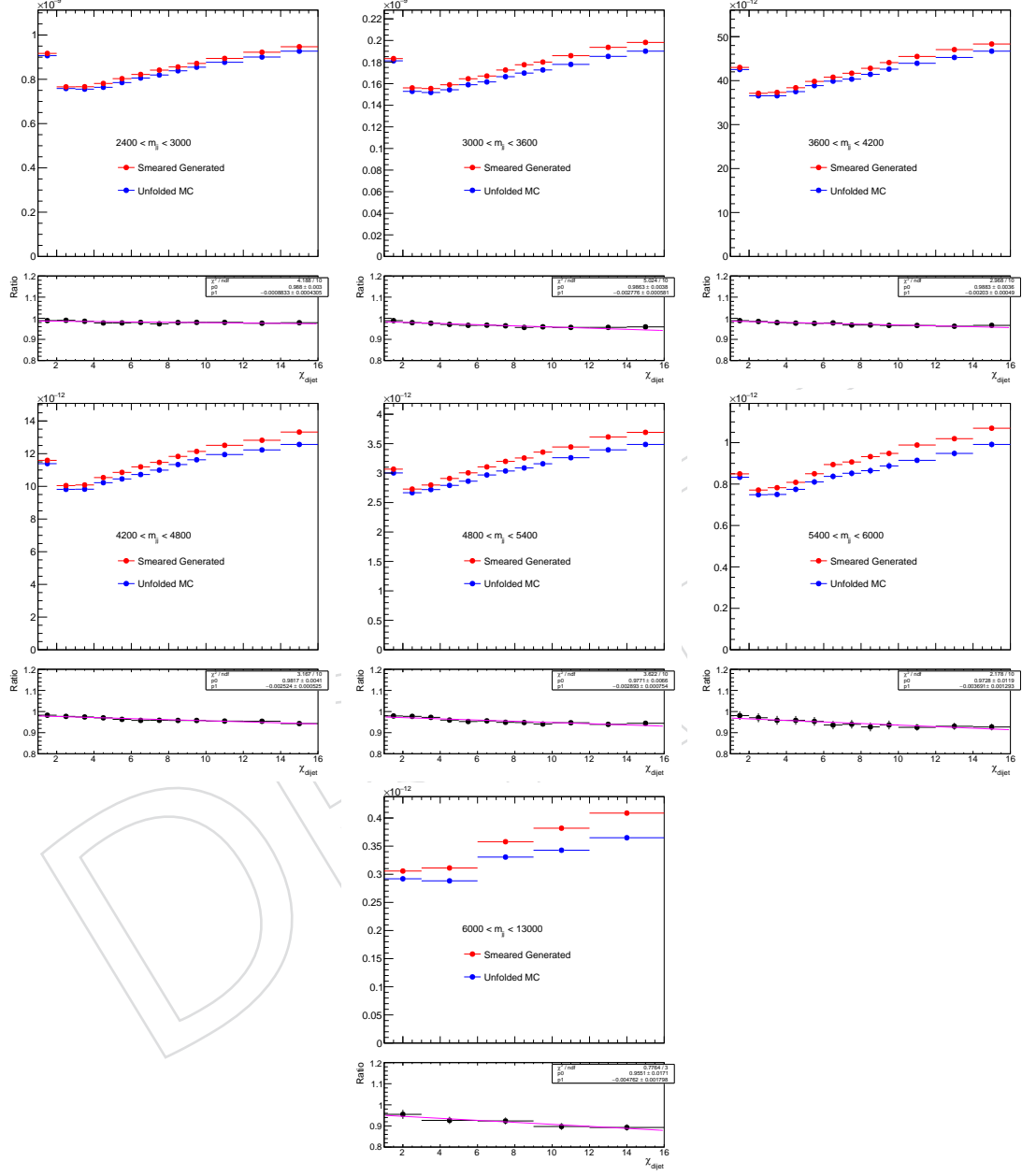


Figure 35: Smeared and unfolded χ_{dijet} distributions in the same MC sample. Also shown are the ratios of the unfolded to smeared χ_{dijet} distributions.

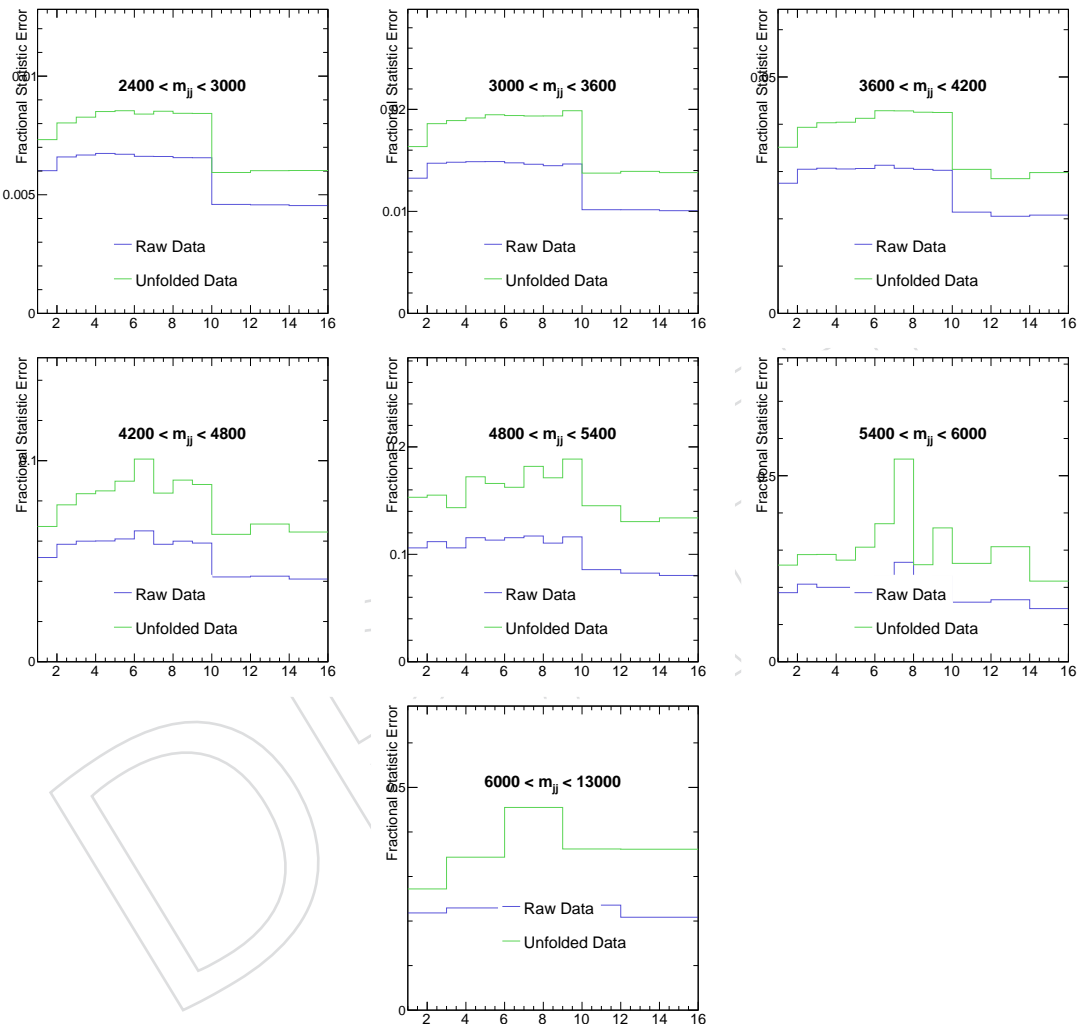
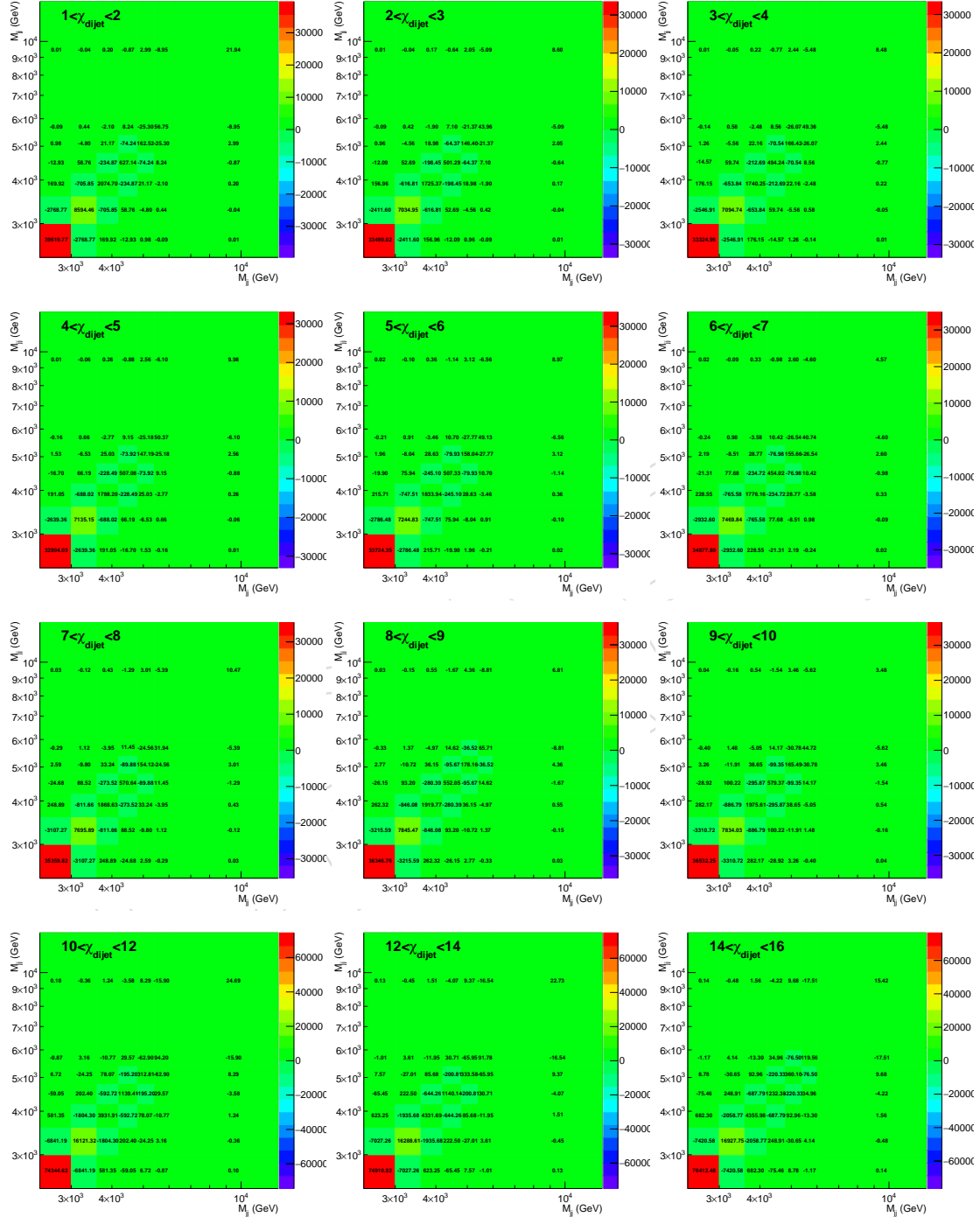
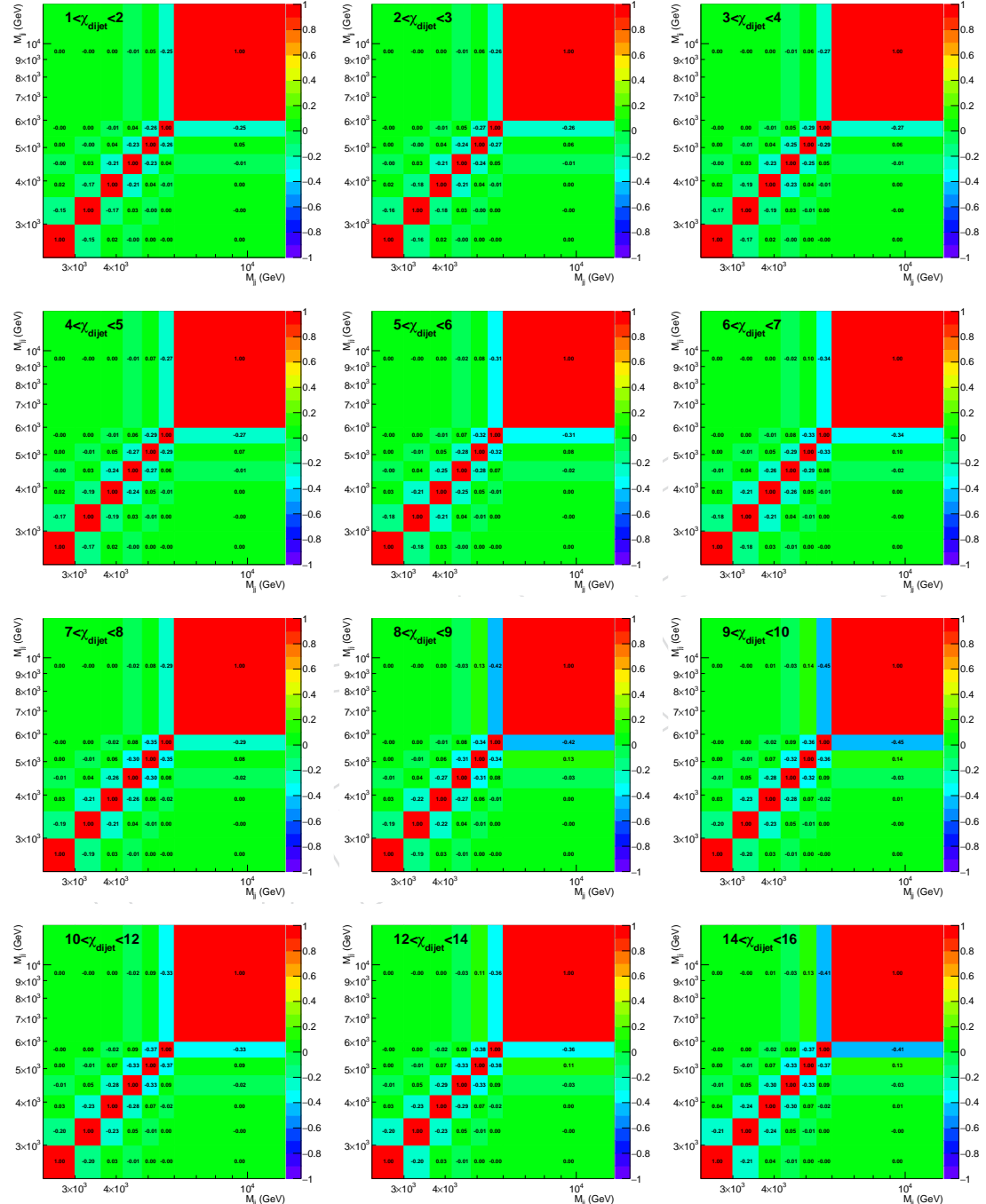


Figure 36: Relative upper statistical uncertainty of the raw data and unfolded data distribution.

Figure 37: Covariance matrices for M_{jj} bins.

Figure 38: Correlation coefficients for M_{jj} bins.

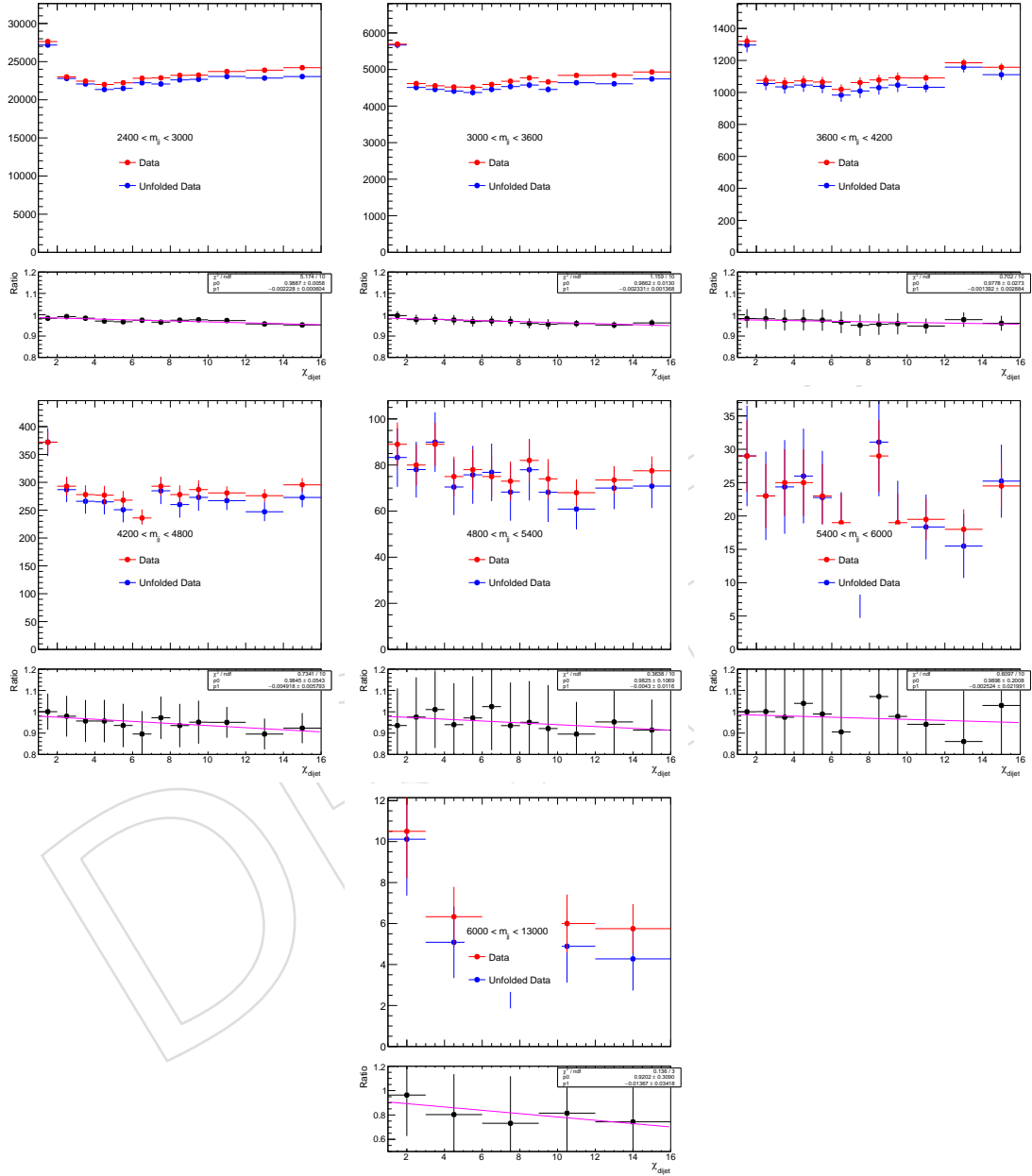


Figure 39: Raw and unfolded χ_{dijet} distributions for Data. Also shown are the ratios of the unfolded to raw χ_{dijet} distributions.

294 4.5 Systematic Uncertainties

295 The dominant sources of experimental uncertainty arises from the uncertainties in the jet en-
296 ergy scale (JES) and jet energy resolution (JER). The contributions to the total systematic uncer-
297 tainty from each of these sources are described below.

298 4.5.1 Uncertainty due to the Jet Energy Scale

299 To calculate the uncertainty introduced by the uncertainty on the jet energy scale, the energy
300 of the particle-flow jets is varied according the p_T and η dependent uncertainties on the various
301 sources of uncertainty on the jet energy scale [53]. The χ_{dijet} distributions are evaluated with
302 the energy of all jets increased (decreased) according to p_T and η dependent uncertainties. Then
303 the ratio between the χ_{dijet} distributions for the original particle-flow jets and the ones with
304 increased (decreased) jet energy is taken, as shown in Figure 40, 41, 42 and 43. All sources are
305 combined to an overall uncertainty labeled "sum in quadrature" in Figure 44 which turns out
306 to be larger than a simple overall variation of the jet energy scale ignoring the correlations of
307 the various sources.

308 4.5.2 Uncertainty due to the Jet Energy Resolutions

309 For the jet energy resolution uncertainty, variations in the Gaussian core of the jet energy resolu-
310 tion function are considered [53]. The size of the of the variations are from 1% to 5% depending
311 on pseudorapidity according to the recipe from JER group. To evaluate the effect of the jet en-
312 ergy resolution uncertainty on the dijet angular distributions, the generated jets are smeared
313 in energy using Gaussians with widths given by the measured MC jet energy resolution. Ad-
314 dditional jet collections are obtained by smearing the generated jets with jet energy resolution
315 varied by 1% to 5% depending on pseudorapidity from the nominal values. The uncertainty is
316 obtained from the ratios of the χ_{dijet} distributions obtained with the 1% to 5% shift in the JER
317 to those obtained from the nominal JER. These ratios are shown in Fig. 45.

318 The unsmeering factor is derived taking into account the full jet energy resolution parametriza-
319 tion including tails. However, the size of the jet resolution tails has been constrained from data
320 only to a limited extent [53]. Figure 46 shows the effects of the smearing with and without tails.
321 We assign 50% of this difference as an additional uncertainty.

322 Another source of systematic uncertainty considered comes from the fact that the smeared
323 generator jets, used to derive the unfolding corrections, do not fully describe the detector ef-
324 fects. Therefore, the difference between smeared generated jets and JES-corrected reconstructed
325 particle-flow jets from the GEANT simulation, as shown in Figure 47, is treated as an uncer-
326 tainty.

327 Finally, we study the impact of using two different generators to derive the unfolding correction
328 in Fig. 48. This probes the impact of possible mismodeling of the jet kinematics. he observed
329 differences are much small.

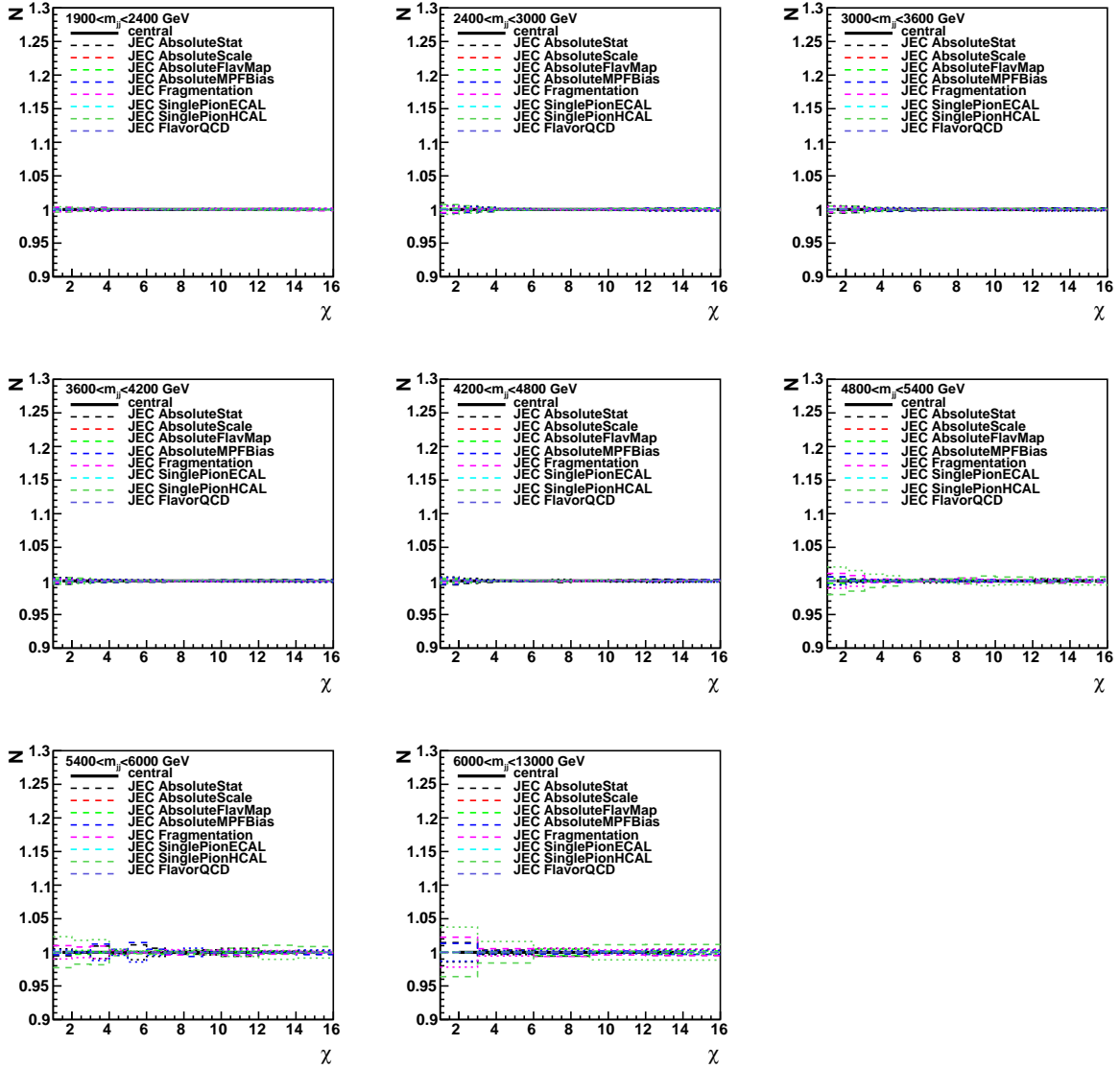


Figure 40: The effect of the jet energy correction uncertainty on the dijet angular distribution (χ_{dijet}).

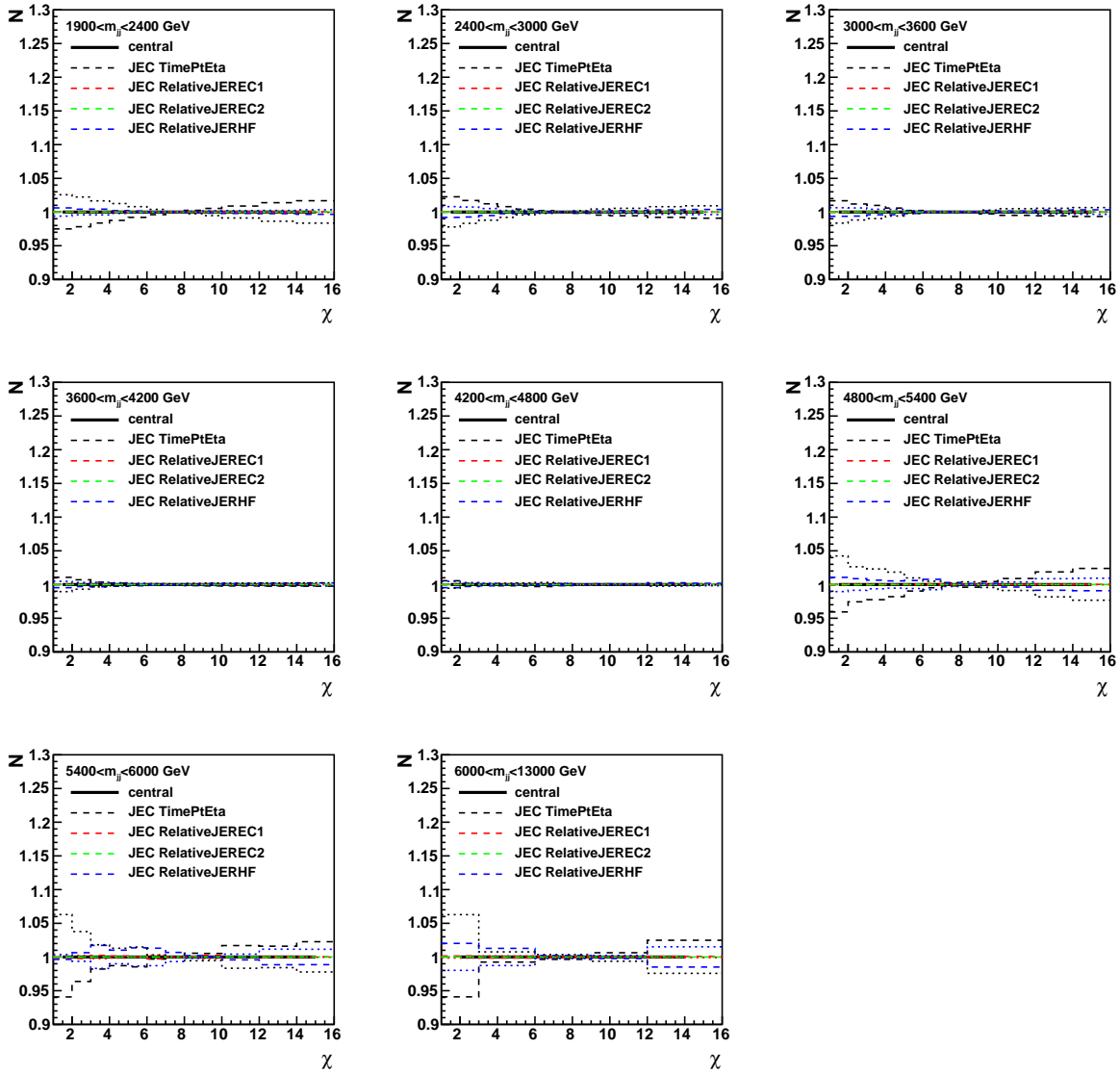


Figure 41: The effect of the jet energy correction uncertainty on the dijet angular distribution (χ_{dijet}).

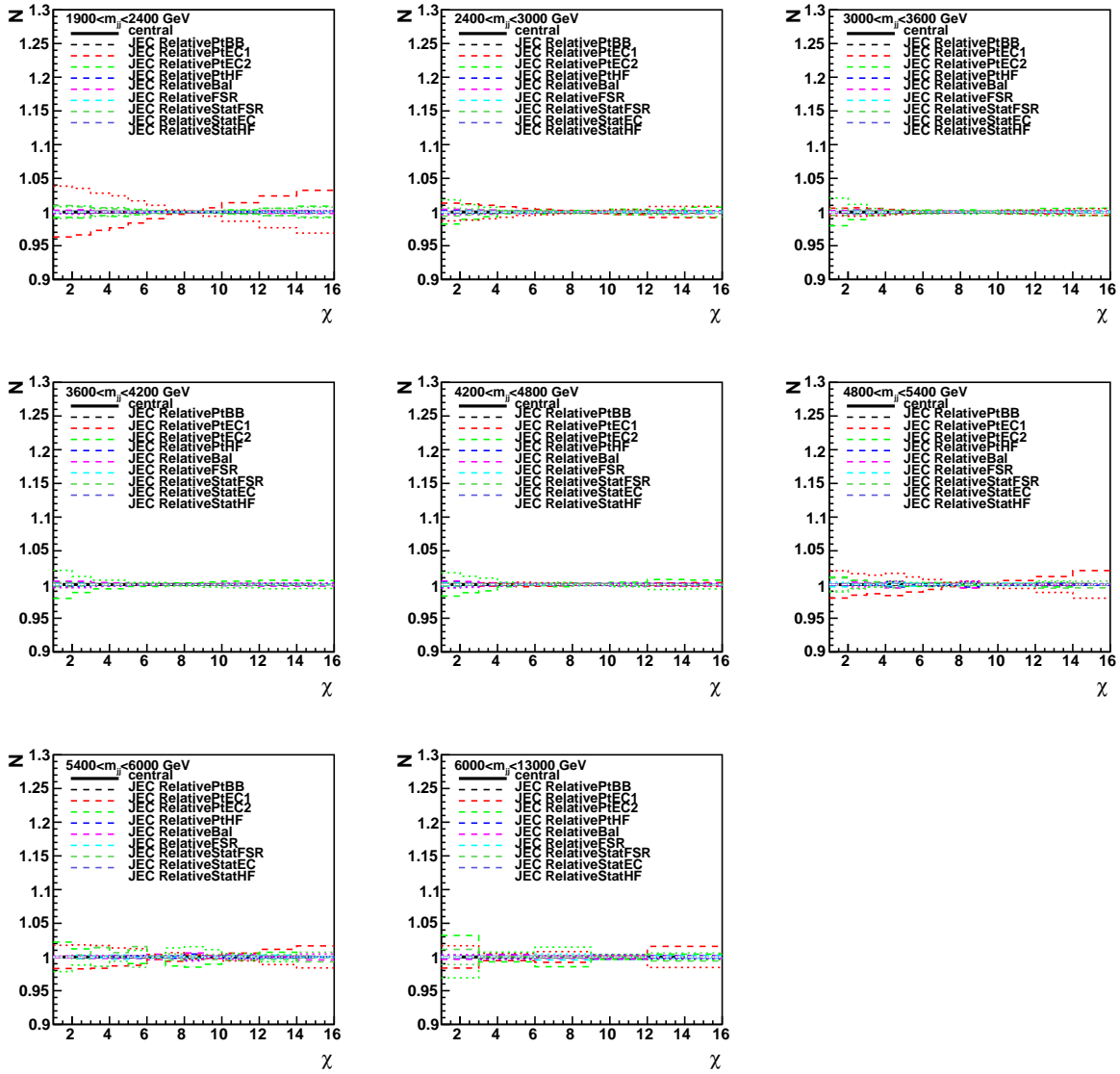


Figure 42: The effect of the jet energy correction uncertainty on the dijet angular distribution (χ_{dijet}).

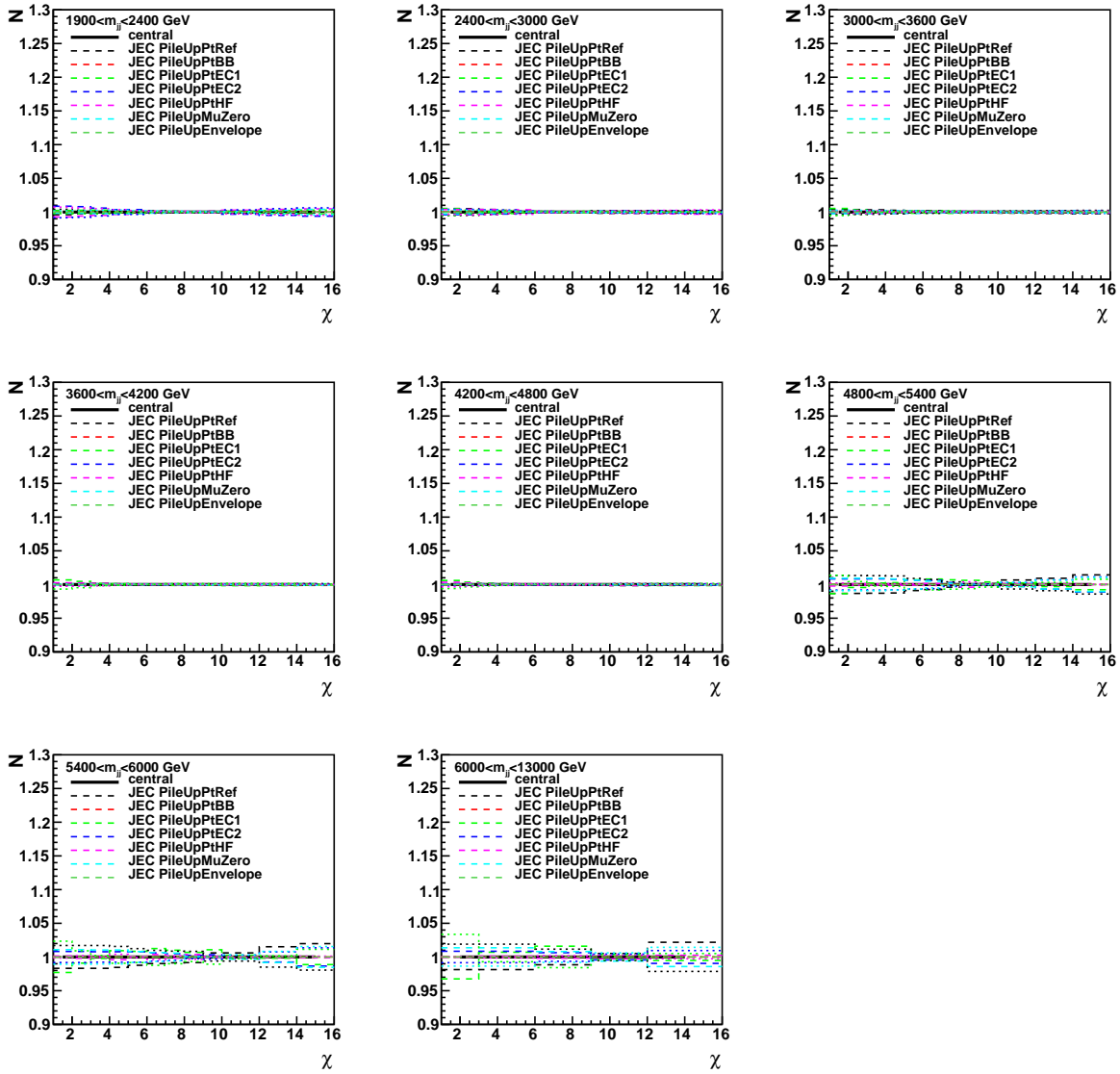


Figure 43: The effect of the jet energy correction uncertainty on the dijet angular distribution (χ_{dijet}).

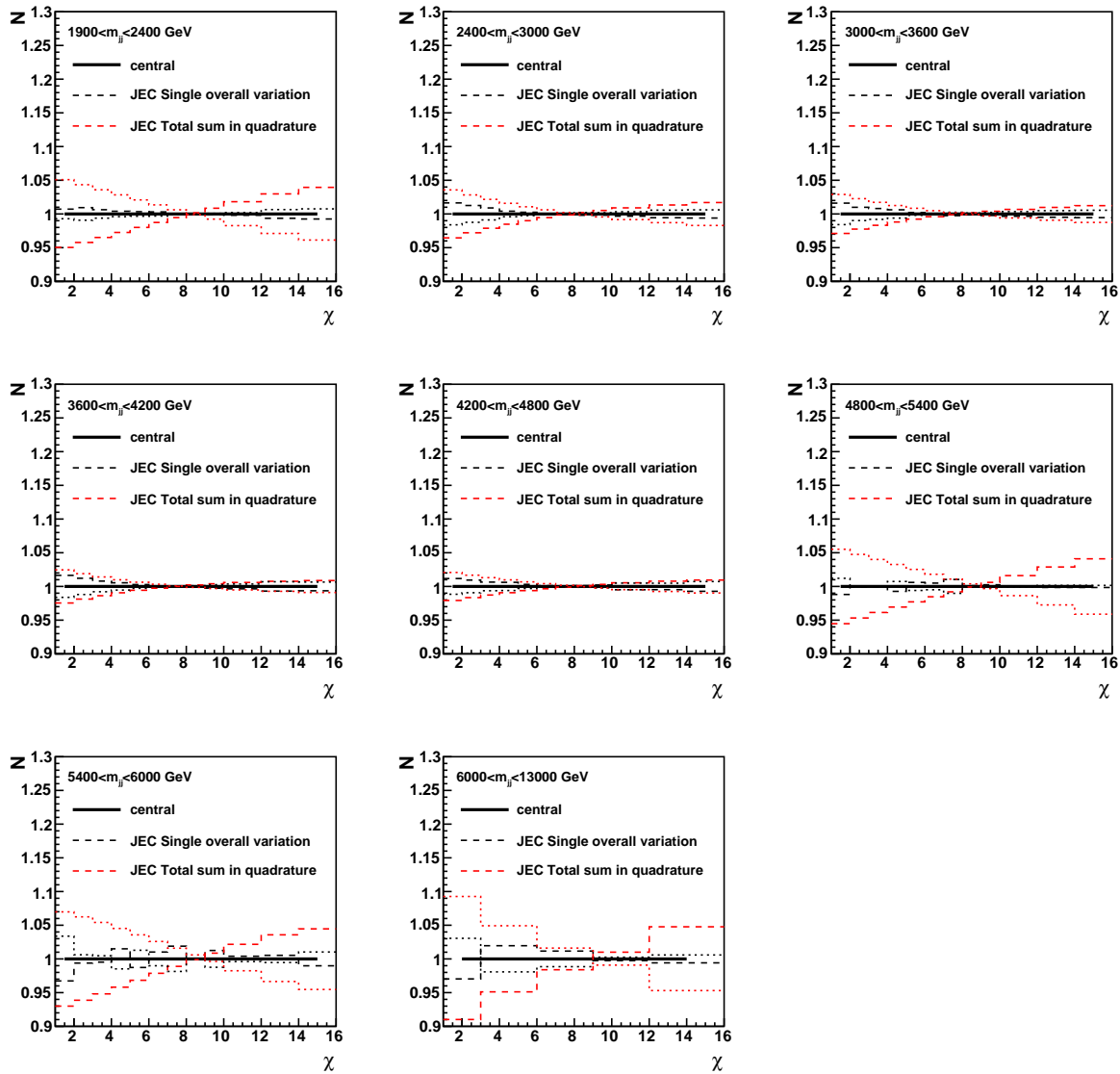


Figure 44: The effect of the jet energy correction uncertainty on the dijet angular distribution (χ_{dijet}).

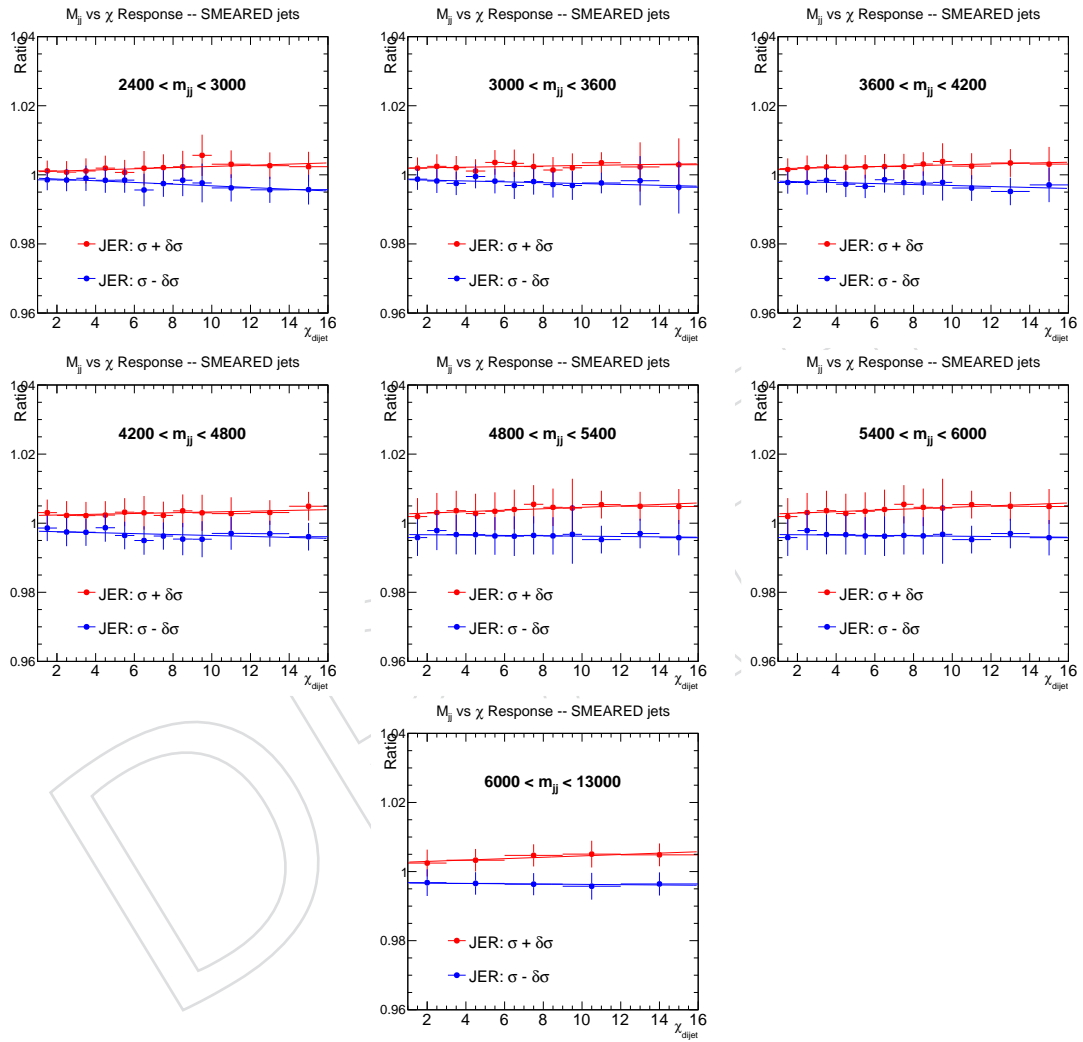


Figure 45: The effect of jet energy resolution uncertainty on the dijet angular distribution (χ_{dijet}).

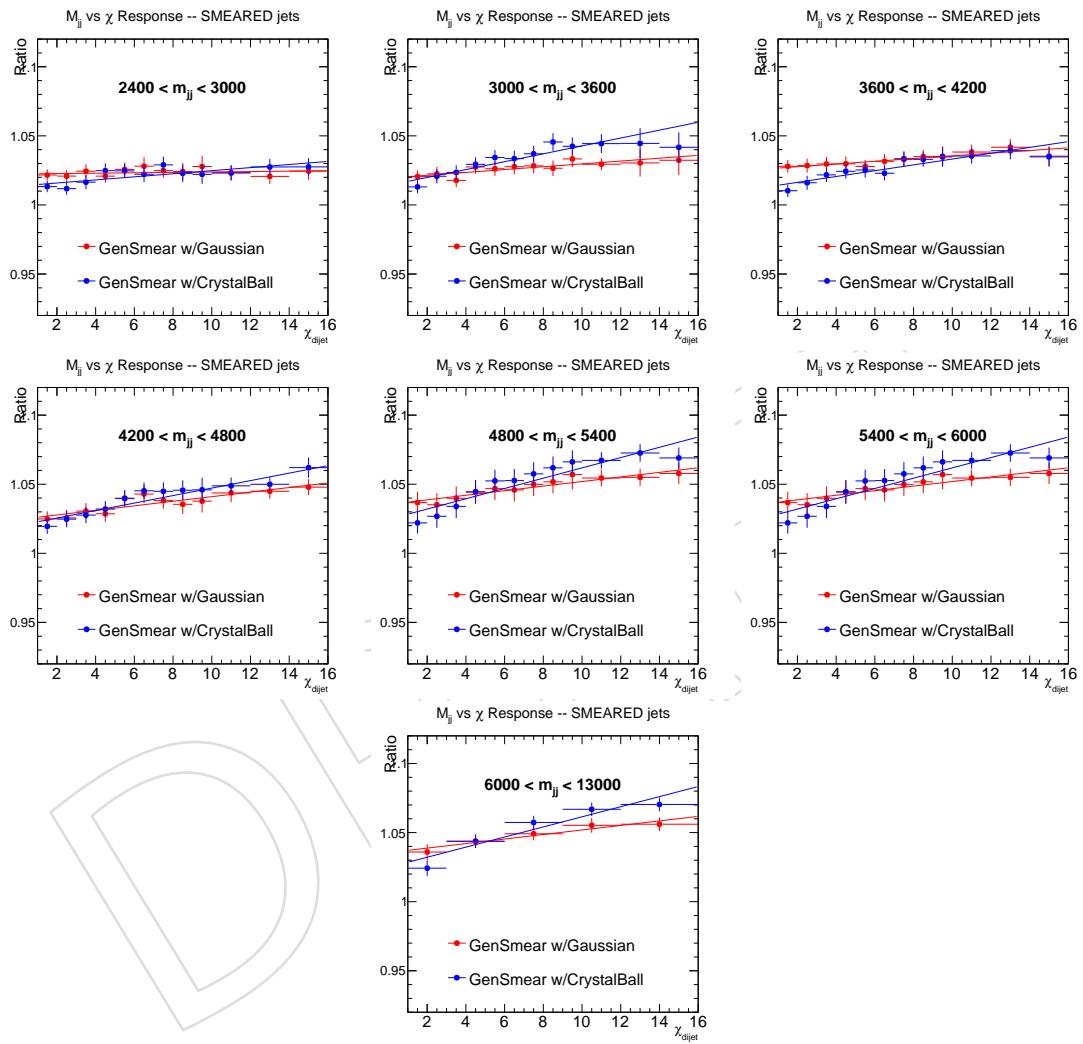


Figure 46: Effect of the jet energy resolution gaussian core (red) and tails (blue) on the smearing correction.

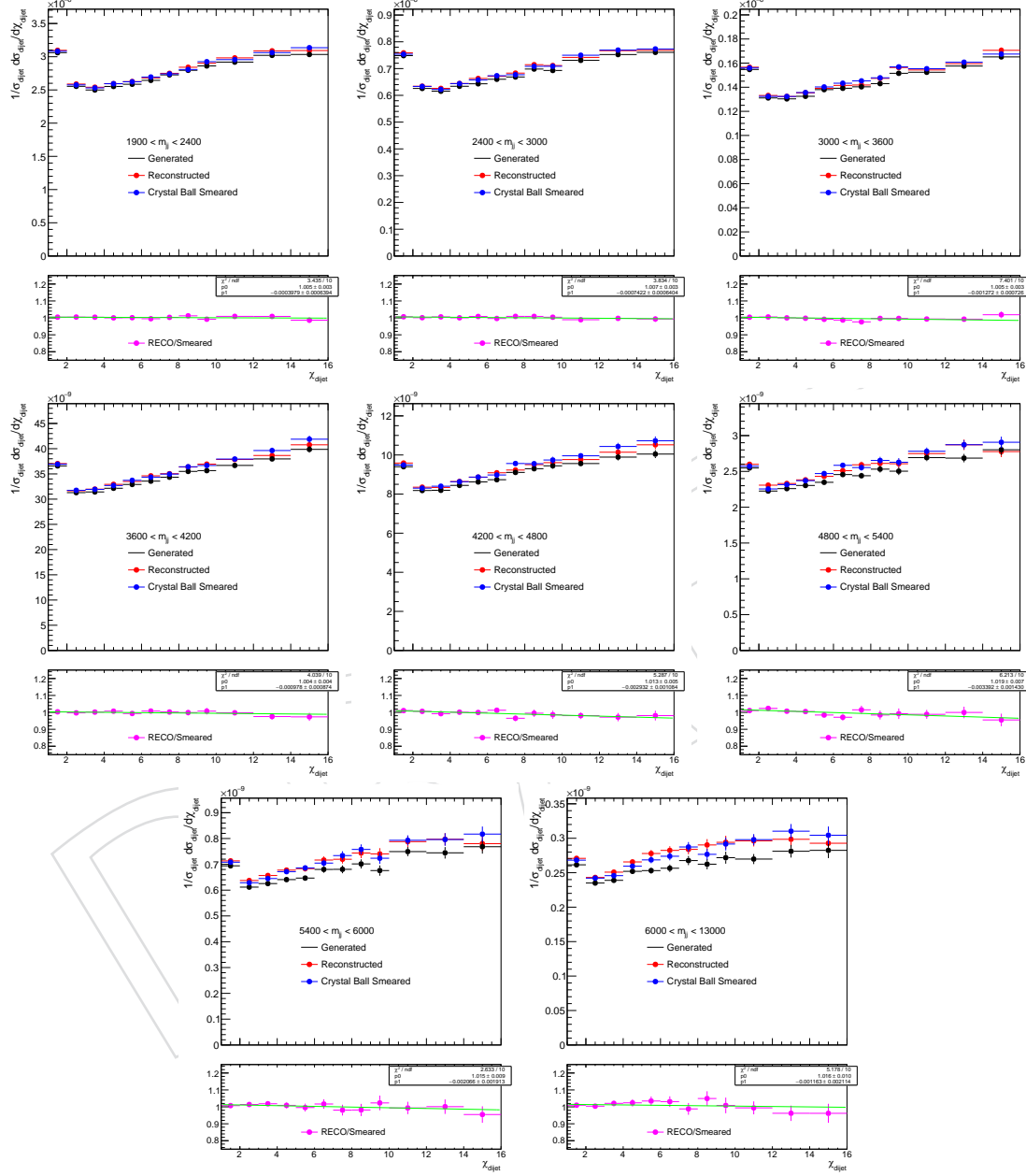


Figure 47: Dijet angular distributions (χ_{dijet}) from generated jets smeared with a Crystal-Ball compared to those from JES-corrected particle-flow jets from the GEANT full simulation.

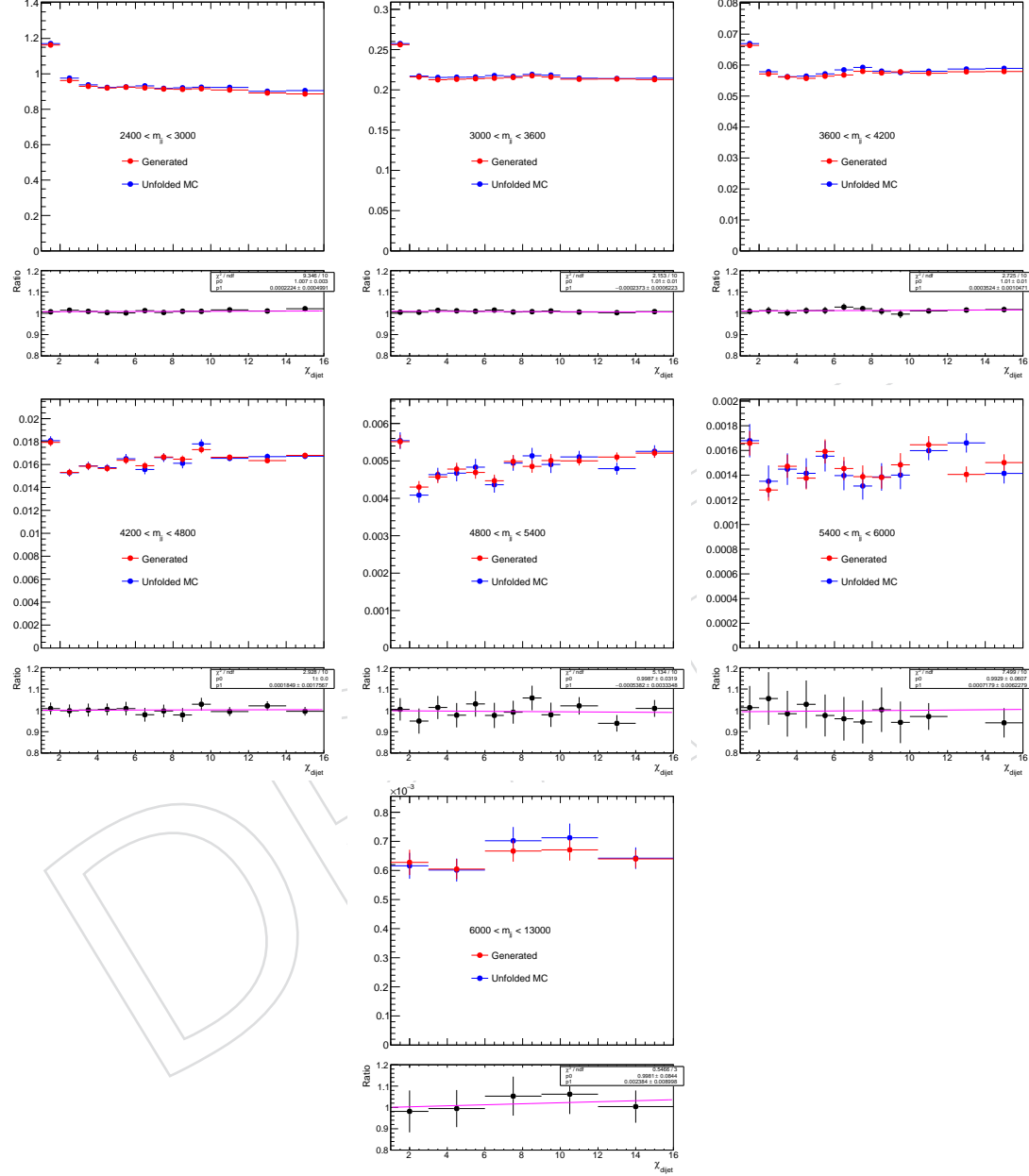


Figure 48: Ratios of unfolded and generated χ_{dijet} distributions from MADGRAPH where the response matrix used for the unfolding was derived from an independent sample of events generated by PYTHIA.

330 **4.5.3 Impact of pile up**

331 At the LHC, the collisions overlapping in the same bunch-crossing is known as pile up. The
 332 impact of pile up is studied for the variable χ with the base event selection. The detector
 333 simulation includes the simulation of pileup. The amount of pileup vertices is similar to the
 334 distribution data, though not perfect. Therefore a reweighting is applied to the simulated sam-
 335 ples to match the pileup distribution of the 2016 data. We evaluate the sensitivity to pileup
 336 for this analysis by comparing the angular distributions with and without pileup reweighting
 337 in Fig. 49. This procedure is very similar to varying the cross section for pileup interactions
 338 according to its measured value, though yielding a slightly larger uncertainty estimate.

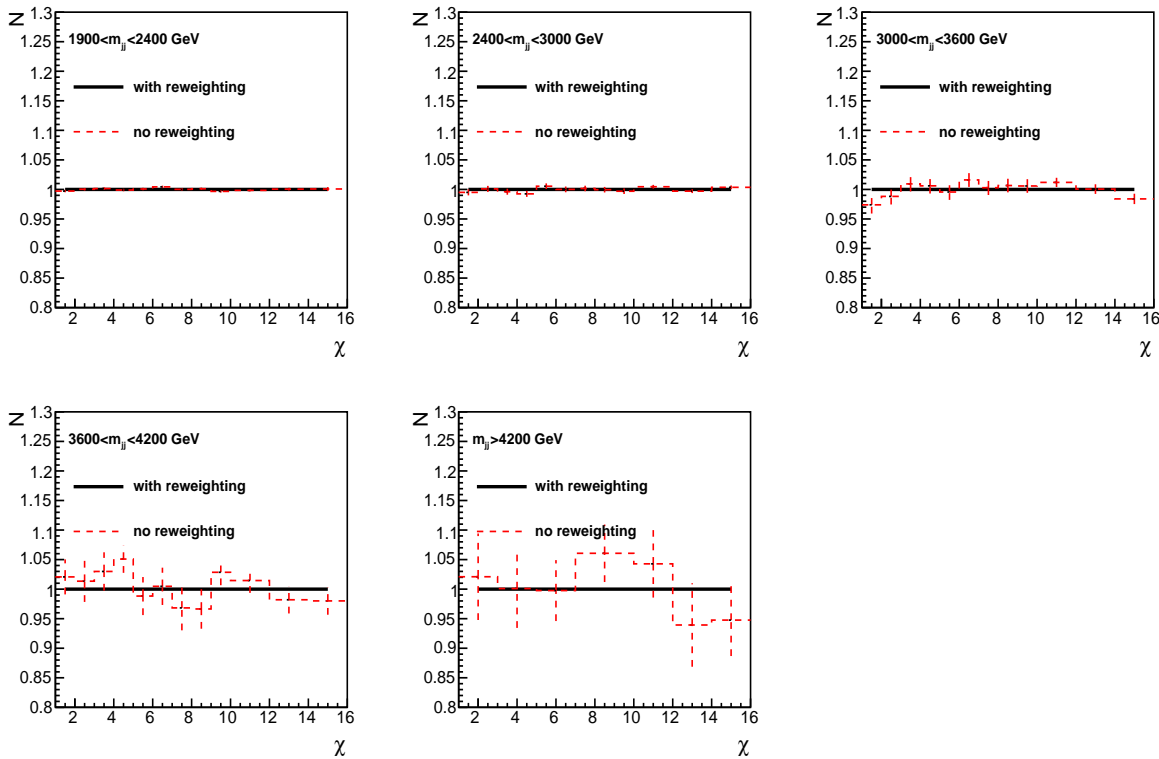


Figure 49: The ratio of the angular distributions with and without pileup reweighting. (From 8 TeV Data. NO CHANGE IN SIZE OF EFFECT EXPECTED for 2016 Data).

339 From the ratio of the angular distributions shown in Figure 49, the effect of pileup is found to
 340 be negligible.

341 5 Theory predictions

342 5.1 QCD predictions

343 We use the NLOJET++ [61] program to calculate predictions for the angular distributions to
 344 next-to-leading order (NLO). This program is also integrated into the fastNLO package [62],
 345 which is used to calculate parton distribution function (PDF) and scale uncertainties with fast
 346 performance. A detailed description of the procedure is given in Ref [63]. The calculation is
 347 performed using CT14 NLO PDFs [64] with the same α_S used in the matrix element calculation
 348 and in the PDFs. The factorization scale μ_F and renormalization scales μ_R are set to the average
 349 p_T of the two leading jets ($\mu_F = \mu_R = \langle p_T \rangle$).

350 We use the same analysis phase space as defined in Section 2.

351 5.1.1 Electroweak corrections

352 Electroweak corrections for dijet production have been derived in Ref. [65], the authors of
 353 which provided us with the corresponding 13 TeV corrections for the χ_{dijet} distributions. These
 354 corrections change the predictions of the normalized χ_{dijet} distributions by up to 1% (5%) at
 355 low (high) M_{jj} in Run 2.

356 5.1.2 Non-perturbative corrections

357 To make meaningful comparisons, theory and data need to be compared at the particle-level.
 358 The NLO calculations, however, are performed at parton-level only. Therefore we derive non-
 359 perturbative corrections using Monte Carlo generators and apply them to the NLO predictions.

$$\sigma_{\text{NLO+Non-Pert.}}^{\text{QCD}} = \sigma_{\text{NLO}}^{\text{QCD}} \cdot (\text{non-perturbative corrections}) \quad (3)$$

360 We use PYTHIA8 and HERWIG++ to study the effect from different generators. The non-
 361 perturbative corrections are defined as the combination of the corrections due to hadronization
 362 (PartonLevel:MPI in PYTHIA8, LHCHandler:MultipleInteractionHandler in Herwig++) and to
 363 multiple parton interactions (HadronLevel:Hadronize in PYTHIA8, LHCHandler:HadronizationHandler
 364 in Herwig++). The corrections are obtained using generator jets with and without non-perturbative
 365 effects enabled in the generators. The resulting correction factors are shown in Figure 50. They
 366 are consistent with one within the generated MC statistics for each mass bin. Therefore no
 367 correction is applied and no uncertainty is assigned.

368 5.1.3 Systematic uncertainties

369 The scale uncertainties are obtained by varying both μ_F and μ_R in six combinations: (μ_f, μ_r)
 370 $= (\langle p_T \rangle / 2, \langle p_T \rangle / 2), (\langle p_T \rangle / 2, \langle p_T \rangle), (\langle p_T \rangle, \langle p_T \rangle / 2), (2\langle p_T \rangle, 2\langle p_T \rangle), (2\langle p_T \rangle, \langle p_T \rangle)$ and $(\langle p_T \rangle, 2\langle p_T \rangle)$. They are presented in Figure 51 (pink dashed line). The scale uncertainty varies from
 372 8.5% in the lowest mass bin, to 19% in the highest mass bin.

373 The uncertainty in the calculation due to the PDF uncertainty were evaluated using the set of
 374 uncertainty eigenvectors provided with the CT14 PDF set. They are presented in Figure 51
 375 (blue dash line)

376 The statistical uncertainty for the NLO prediction is within $\pm 1\%$ and neglected.

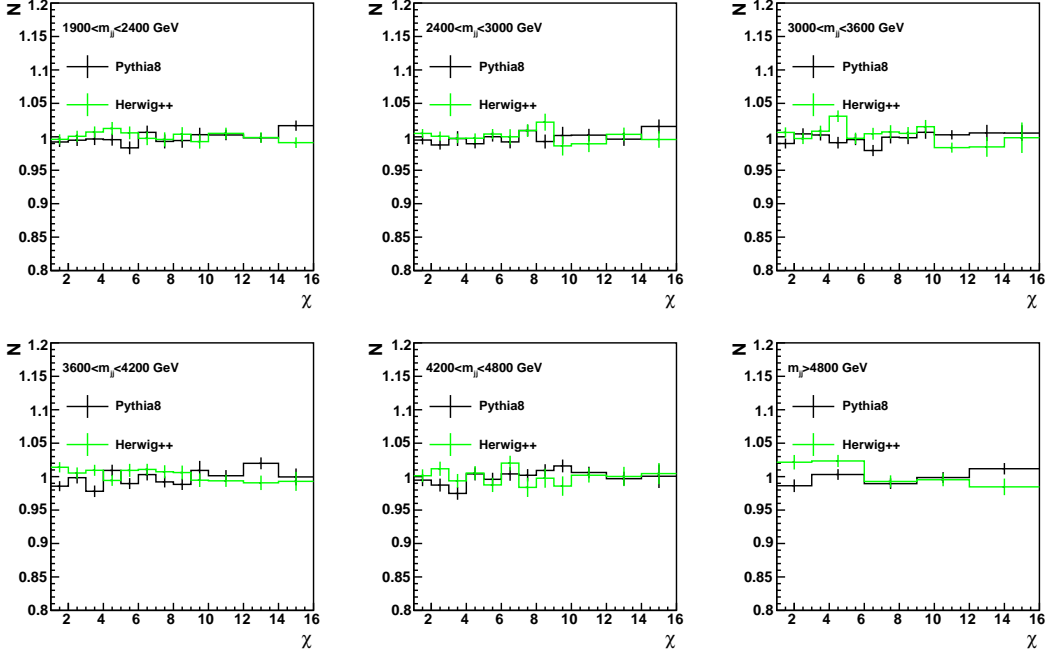


Figure 50: Non-perturbative corrections derived from PYTHIA8 (black) and HERWIG++ (green).

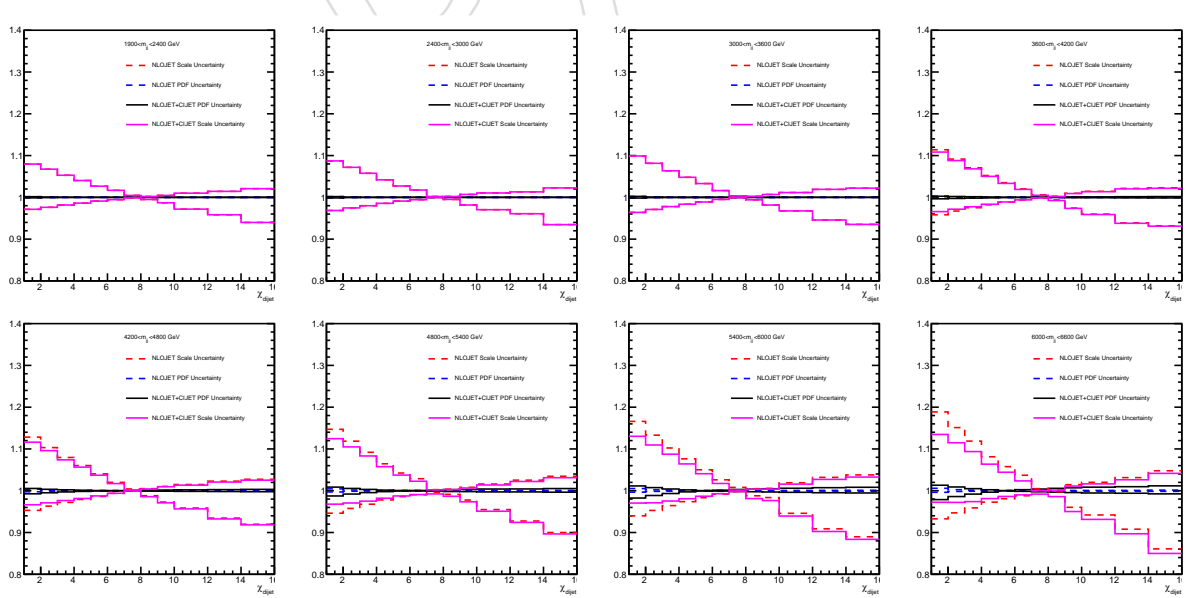


Figure 51: Scale and PDF uncertainty of the QCD NLO and CI ($\Lambda_{LL}^- = 18 \text{ TeV}$) NLO predictions.

³⁷⁷ **5.2 Contact Interaction predictions**

³⁷⁸ This section describes the calculation of a generic new physics model with a Contact Interaction
³⁷⁹ (CI) additional to QCD interactions. A Contact Interaction is introduced for quarks at an energy
³⁸⁰ scale Λ . The corresponding effective Lagrangian for color-singlet contact interactions between
³⁸¹ quarks is

$$L_{qq} = \frac{g^2}{2\Lambda^2} [\eta_{LL}(\bar{q}_L \gamma^\mu q_L)(\bar{q}_L \gamma_\mu q_L) + \eta_{RR}(\bar{q}_R \gamma^\mu q_R)(\bar{q}_R \gamma_\mu q_R) + 2\eta_{RL}(\bar{q}_R \gamma^\mu q_R)(\bar{q}_L \gamma_\mu q_L)]. \quad (4)$$

³⁸² Color-octet contact interactions of similar form are not regarded in this analysis. Different
³⁸³ combinations of η_{LL} , η_{RR} and η_{RL} allow to construct different contact interaction models which
³⁸⁴ are summarized in Table 3.

Table 3: Mapping of contact interaction model and parameters.

model	η_{LL}	η_{RR}	η_{RL}
Λ_{LL}^+	1	0	0
Λ_{LL}^-	-1	0	0
Λ_{RR}^+	0	1	0
Λ_{RR}^-	0	-1	0
Λ_V^+	1	1	1
Λ_V^-	-1	-1	-1
Λ_A^+	1	1	-1
Λ_A^-	-1	-1	1
$\Lambda_{(V-A)}^+$	0	0	1
$\Lambda_{(V-A)}^-$	0	0	-1

³⁸⁵ Note that the models with positive (negative) η_{LL} or η_{RR} lead to destructive (constructive) in-
³⁸⁶ terference with the QCD terms and a lower (higher) cross section. In all CI models discussed in
³⁸⁷ this paper, NLO QCD corrections are employed to calculate the cross sections. In proton-proton
³⁸⁸ collisions the Λ_{LL}^\pm and Λ_{RR}^\pm models result in identical tree level cross sections and NLO correc-
³⁸⁹ tions, and consequently lead to the same sensitivity. For Λ_{VV}^\pm and Λ_{AA}^\pm , as well as for $\Lambda_{(V-A)}^\pm$,
³⁹⁰ the CI predictions are identical at tree level, but exhibit different NLO corrections and yield
³⁹¹ different sensitivity. For calculating the CI terms, as well as the interference between the CI
³⁹² terms and QCD terms at LO and NLO in QCD, the CIJET program version 1.0 [66] is employed.

³⁹³ Scale uncertainty and PDF uncertainty for CI predictions are calculated in a similar way as
³⁹⁴ for QCD predictions and combined with those for QCD. The scale uncertainty in combined CI
³⁹⁵ ($\Lambda_{LL}^- = 18$ TeV) + QCD is 14% in the highest mass bin. The PDF uncertainty in combined CI
³⁹⁶ ($\Lambda_{LL}^- = 18$ TeV) + QCD is 2% in the highest mass bin.

³⁹⁷ **5.3 ADD predictions**

The LO predictions for the ADD model in the GRW convention are calculated with PYTHIA8 using the NNPDF2.3 LO PDFs and the parameters given in Table 4. In order to obtain the best estimate for the QCD plus ADD process, we add the difference $\sigma_{\text{NLO+EW corr}}^{\text{QCD}} - \sigma_{\text{LO}}^{\text{QCD}}$ bin-by-bin to the ADD prediction:

$$\sigma^{\text{QCD+ADD}} = (\sigma_{\text{NLO+EW corr}}^{\text{QCD}} - \sigma_{\text{LO}}^{\text{QCD}} + \sigma_{\text{LO}}^{\text{QCD+ADD}}) \quad (5)$$

Table 4: Pythia8 parameters for the generation of ADD virtual graviton exchange.

parameter	value	description
HardQCD:all	off	custom dijet processes
ExtraDimensionsLED:dijets	on	use extra dimensions
ExtraDimensionsLED:CutOffmode	0	GRW convention
ExtraDimensionsLED:LambdaT	Λ_T	energy scale parameter
ExtraDimensionsLED:nQuarkNew	5	outgoing mass-less quark flavours
ExtraDimensionsLED:opMode	1	use GRW convention

398 The limits set on the GRW predictions can be translated to the HLZ convention with $M_S =$
 399 $\Lambda_T(2/(n_{ED} - 2))^{1/4}$ for $n_{ED} > 2$. For $n_{ED} = 2$ the HLZ prediction can be assembled from the
 400 GRW predictions using $M_S = \Lambda_T(\ln(M_S^2/s))^{1/4}$.

401 5.4 QBH prediction

402 We use QBH 3.0 generator [67] to simulate the QBH productions at matrix element level. We
 403 interface QBH generator with Pythia8 to add non-perturbative effect (such as multiple parton
 404 interactions and hadronizations) to the matrix element level predictions. QBH generator pa-
 405 rameters are given in Table 5. The QBH production cross sections are added to NLO QCD
 406 predictions with EWK corrections.

Table 5: QBH parameters for QBH productions

parameter	value	description
setQscale	true	QCD scale for PDFs to be inverse gravitational radius
setLHAglue	10042	CTEQ6L1 PDF
setPlanckdef	3	definition of Planck Scale to be PDF definition
setSM	false	Allow violation of standard model global symmetry
setHiggs	true	Include higgs as QBH decay product
setGraviton	true	Include Graviton as QBH decay product
setChiral	false	Neutrinos are only left-handed
setMajorana	false	Neutrinos are Dirac particles

407 5.5 Dark Matter prediction

Interactions of quarks and dark matter particles with vector and axial-vector mediators in a simplified model [46, 47] are generated using MADDM version 2.0.6 [68, 69]. As described in Section 1, the Lagrangians of the simplified dark matter models for spin-1 mediator are as following

$$L_{\text{vector}} = -g_{\text{DM}} Z'_\mu \bar{\chi} \gamma^\mu \chi - g_q \sum_{q=u,d,s,c,b,t} Z'_\mu \bar{q} \gamma^\mu q, \quad (6)$$

$$L_{\text{axial-vector}} = -g_{\text{DM}} Z'_\mu \bar{\chi} \gamma^\mu \gamma_5 \chi - g_q \sum_{q=u,d,s,c,b,t} Z'_\mu \bar{q} \gamma^\mu \gamma_5 q, \quad (7)$$

408 where Z' stands for the mediators and χ stands for dark matter particles. The dark matter
 409 predictions are simulated at fixed g_{DM} and m_{DM} values, where $g_{\text{DM}} = 1.0$ and $m_{\text{DM}} = 1 \text{ GeV}$.
 410 For mediator masses with 2.0, 2.5, 3.0, 3.5, 4.0, 4.5, 5.0, 6.0, and 7.0 TeV, samples with $g_q = 0.01$,
 411 0.05, 0.1, 0.2, 0.3, 0.5, 0.75, 1.0, 1.5, 2.0, 2.5, and 3 are generated.

412 The simulated mediator width as a function of its coupling to quarks g_q is shown in Figure 52.
 413 Scenarios with $g_q > 0.5$ are of particular interest to this search as they predict resonances
 414 with a width larger than 15% to which the sensitivity of dijet resonance searches are limited.
 415 The inclusive cross section (before acceptance) as a function of mediator mass is shown in
 416 Fig. 53. The acceptance of this analysis as a function of mediator mass is shown in Fig. 54. The
 417 difference in the cross sections, and the acceptance in the analysis phase space, between vector
 418 and axial-vector mediators are negligible for our samples with $g_{DM} = 1.0$ and $m_{DM} = 1$ GeV.
 419 The effect for the PDF uncertainty on the acceptance for the DM signals are evaluated using the
 420 NNPDF3.0 LO PDF set. For a mediator with 2.0 TeV mass and 50% width, the PDF acceptance
 421 uncertainty for the first chi bin in the 2.4–3.0 mass bin is 0.7%. For a mediator with 5.0 TeV
 422 mass and 50% width, the PDF acceptance uncertainty for the first chi bin in the 4.8–5.4 mass
 423 bin are 6.2%. For a mediator with 6.0 TeV mass and 50% width, the PDF acceptance uncertainty
 424 for the first chi bin in the 6.0–13.0 mass bin are 14.0%. Since the PDF acceptance uncertainties
 425 are negligible compared to other uncertainty sources for the simulated samples with mediator
 426 mass smaller than 6 TeV, we will only include the PDF acceptance uncertainty for the 6 and 7
 427 TeV mass mediator samples.

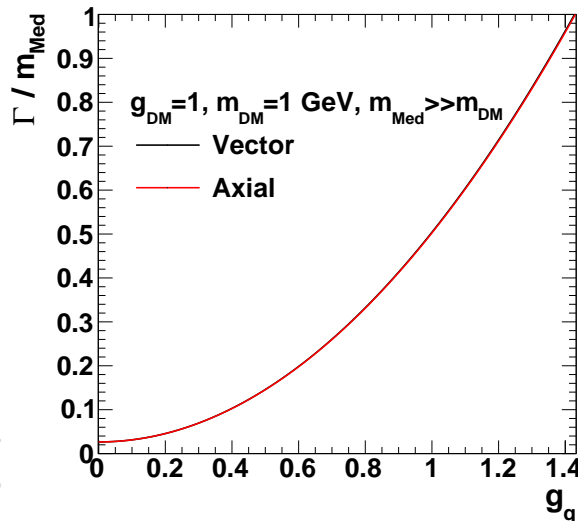


Figure 52: Resonance width predicted by the DM benchmark model with $g_{DM} = 1$, $m_{DM} = 1$ GeV and a vector or axial vector mediator with mass $M_{Med} \gg m_{DM}$.

428 To take into account the NLO QCD and EW corrections to standard model dijet production
 429 when probing the DM models, the cross section difference $\sigma_{NLO+EW\,corr}^{QCD} - \sigma_{LO}^{QCD}$ is evaluated for
 430 each m_{jj} and χ_{dijet} bin and added to the dark matter predictions. This procedure provides a SM
 431 + dark matter prediction wherein the QCD terms are corrected to NLO with EW corrections
 432 while the dark matter terms are calculated at LO.

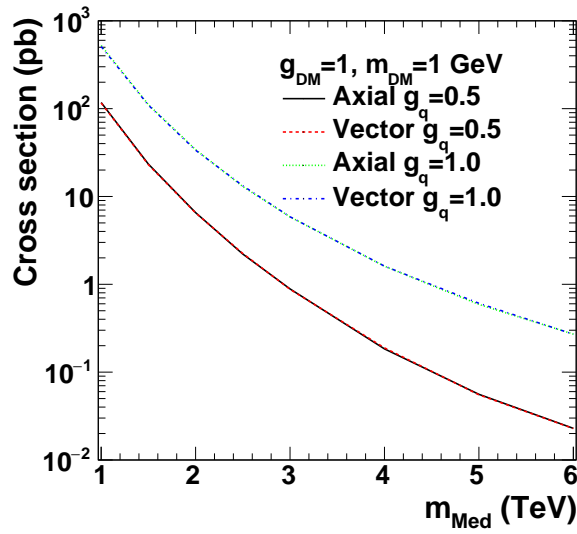


Figure 53: Inclusive cross section (before acceptance) for the DM benchmark model with $g_{\text{DM}} = 1, m_{\text{DM}} = 1 \text{ GeV}$ and an axial vector mediator with mass $M_{\text{Med}} >> m_{\text{DM}}$.

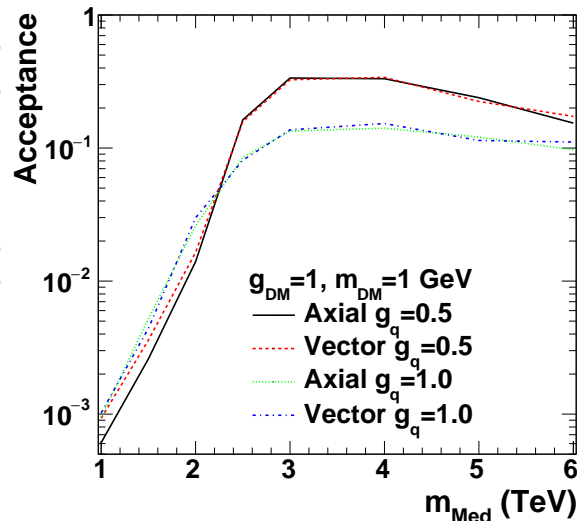


Figure 54: Acceptance ($|y_{\text{boost}}| < 1.11, \chi_{\text{dijet}} < 16, M_{\text{jj}} > 2.4 \text{ TeV}$) for the DM benchmark model with $g_{\text{DM}} = 1, m_{\text{DM}} = 1 \text{ GeV}$ and an axial vector mediator with mass $M_{\text{Med}} >> m_{\text{DM}}$.

433 6 Results

434 A summary of the statistical and systematic uncertainties can be found in Table 6.

Table 6: Summary of leading experimental and theoretical uncertainties on the normalized χ_{dijet} distributions. While in the statistical analysis each uncertainty is represented by a change of the χ_{dijet} distribution correlated among all χ_{dijet} bins, this table summarizes each uncertainty by a representative number to demonstrate the relative contributions. For the lowest and highest dijet mass bins, the relative shift of the lowest χ_{dijet} bin from its nominal value is quoted. In the highest dijet mass bin, the dominant experimental contribution is the statistical uncertainty while the dominant theoretical contribution is the scale uncertainty.

Uncertainty	$2.4 < M_{\text{jj}} < 3.0 \text{ TeV}$	$M_{\text{jj}} > 6.0 \text{ TeV}$
Statistical	0.7%	27%
Jet energy scale	3.6%	9.2%
Jet energy resolution (core)	1.0%	1.0%
Jet energy resolution (tails)	1.0%	1.5%
Unfolding, modeling	0.2%	1.5%
Unfolding, detector simulation	0.5%	1.0%
Pileup	<1%	<1%
Total experimental	4.1%	29%
QCD NLO scale (6 variations of μ_R and μ_F)	+8.5% −3.0%	+19% −5.8%
PDF (CT14 eigenvectors)	0.2%	0.6%
Non-perturbative effects	<1%	<1%
Total theoretical	8.5%	19%

435 A comparison of the statistical and systematic uncertainties for the 4.8-13.0 TeV mass bin in
 436 2015 analysis and 4.8-5.4 and 6.0-13.0 TeV mass bins can be found in Table 7. The experimental
 437 uncertainties in 2016 analysis are bigger than those in 2015 analysis.

Table 7: Comparison of leading experimental and theoretical uncertainties on the normalized χ_{dijet} distributions in 2015 analysis and 2016 analysis.

Uncertainty	$M_{\text{jj}} > 4.8 \text{ TeV} (2015)$	$4.8 < M_{\text{jj}} < 5.4 \text{ TeV} (2016)$	$M_{\text{jj}} > 6.0 \text{ TeV} (2016)$
Statistical	26%	14%	27%
Jet energy scale	3.6%	5.5%	9.2%
Jet energy resolution (core)	1.1%	1.0%	1.0%
Jet energy resolution (tails)	0.5%	1.5%	1.5%
Unfolding, modeling	0.8%	0.3%	1.5%
Unfolding, detector simulation	0.8%	2.1%	1.0%
Pileup	<1%	<1%	<1%
Total experimental	26%	15%	29%
QCD NLO scale (6 variations of μ_R and μ_F)	+13% −4.9%	+13% −4.9%	+19% −5.8%
PDF (CT14 eigenvectors)	0.4%	0.4%	0.6%
Non-perturbative effects	<1%	<1%	<1%
Total theoretical	13%	13%	19%

- 438 In Figure 55, the corrected dijet angular distributions, normalized to the total number of events
 439 within each M_{jj} region, are shown. The number of events in each mass bin are given in Table 2.
 440 The error bars in the final distributions reflect the statistical and systematic uncertainties added
 441 in quadrature.
- 442 The data are compared to pQCD predictions at next-to-leading order (NLO) with EWK cor-
 443 rections. The factorization and renormalization scales are added in quadrature with the PDF
 444 uncertainties and the non-perturbative correction uncertainty.

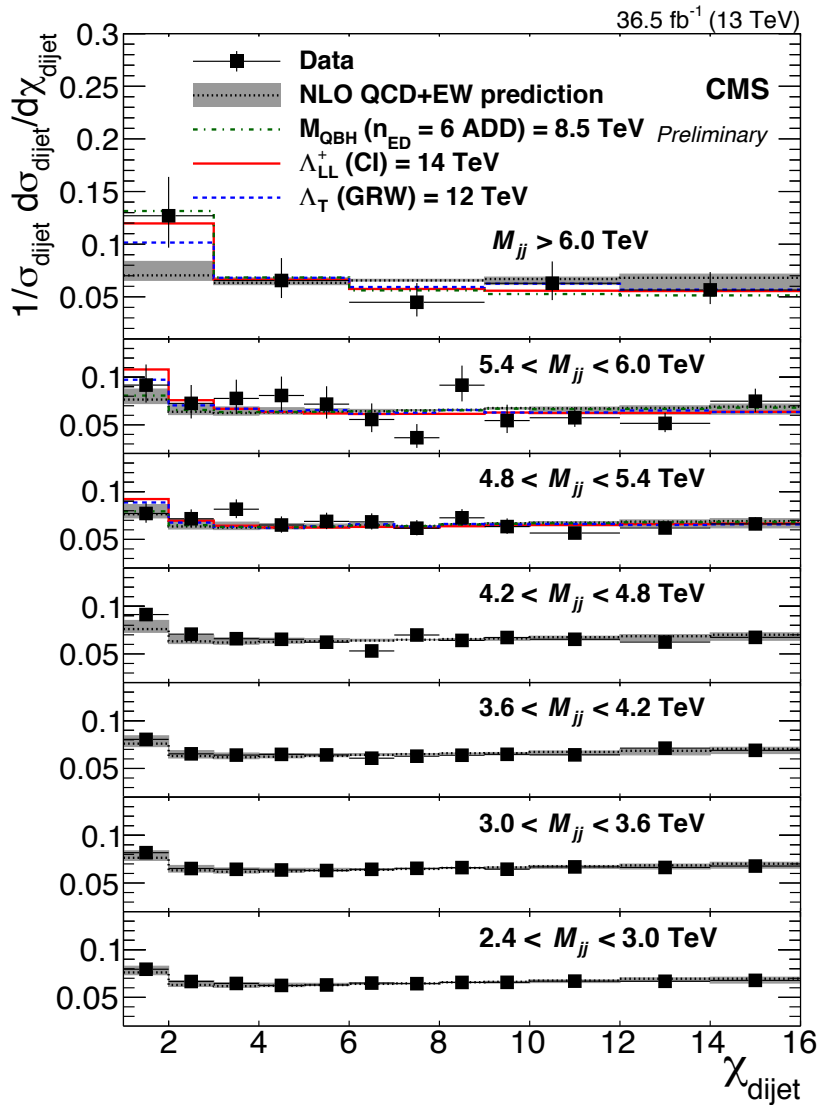


Figure 55: Normalized χ_{dijet} distributions for 35.9 fb^{-1} of integrated luminosity. The corrected data distributions are compared to NLO predictions with non-perturbative corrections (black dotted line). Theoretical uncertainties are indicated as a gray band. The error bars represent statistical and experimental systematic uncertainties combined in quadrature. The ticks on the error bars represent experimental systematic uncertainties only. The prediction for QCD+CI with Λ_{LL}^+ (LO) = 14 TeV is shown (red solid line), and so is the prediction for QCD+ADD with Λ_T (GRW) = 13 TeV (blue dashed line).

- 445 Figure 56 shows a comparison of unfolded data and raw data.

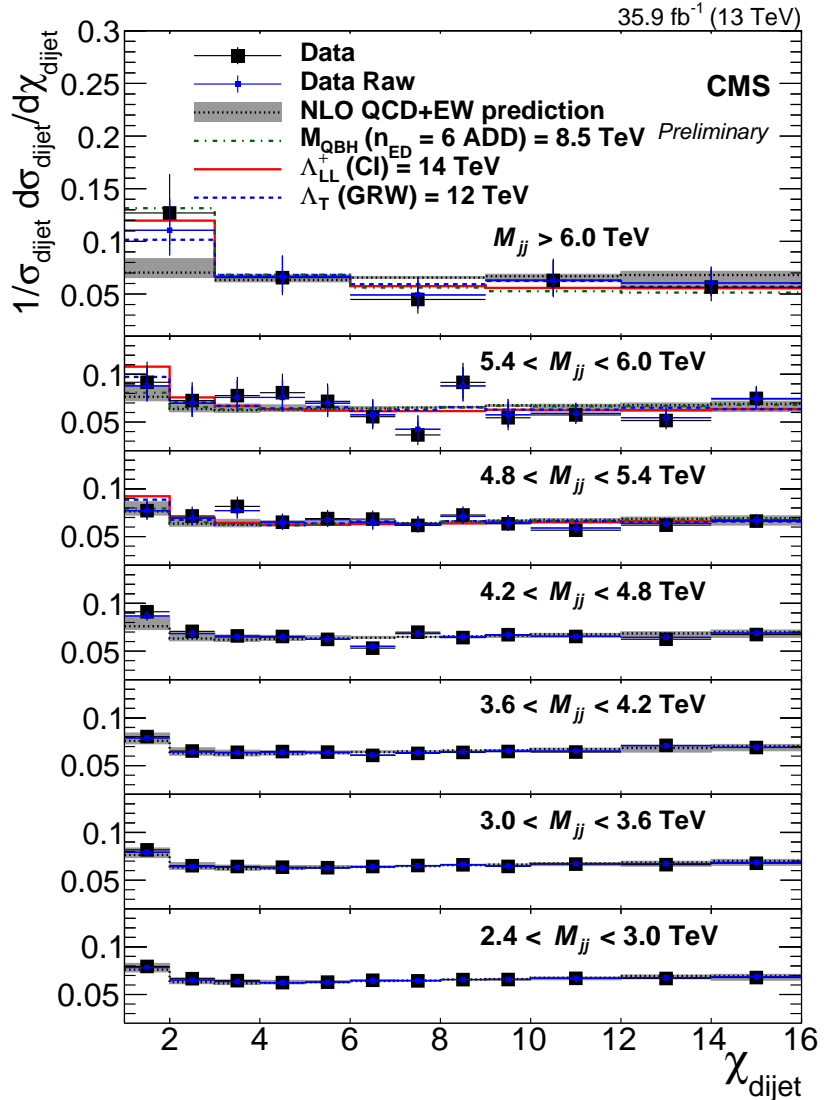


Figure 56: Comparison of unfolded data and raw data.

⁴⁴⁶ In Figure 57 we also provide a comparison of the detector-level data with a detector-level LO
⁴⁴⁷ Pythia8 QCD simulation and 2015 data. The 2016 and 2015 data agree very well, demonstrating
⁴⁴⁸ similar detector resolution/response in 2015 and 2016. Since this simulation does not include
⁴⁴⁹ NLO QCD correction it is not expected to model the data perfectly.

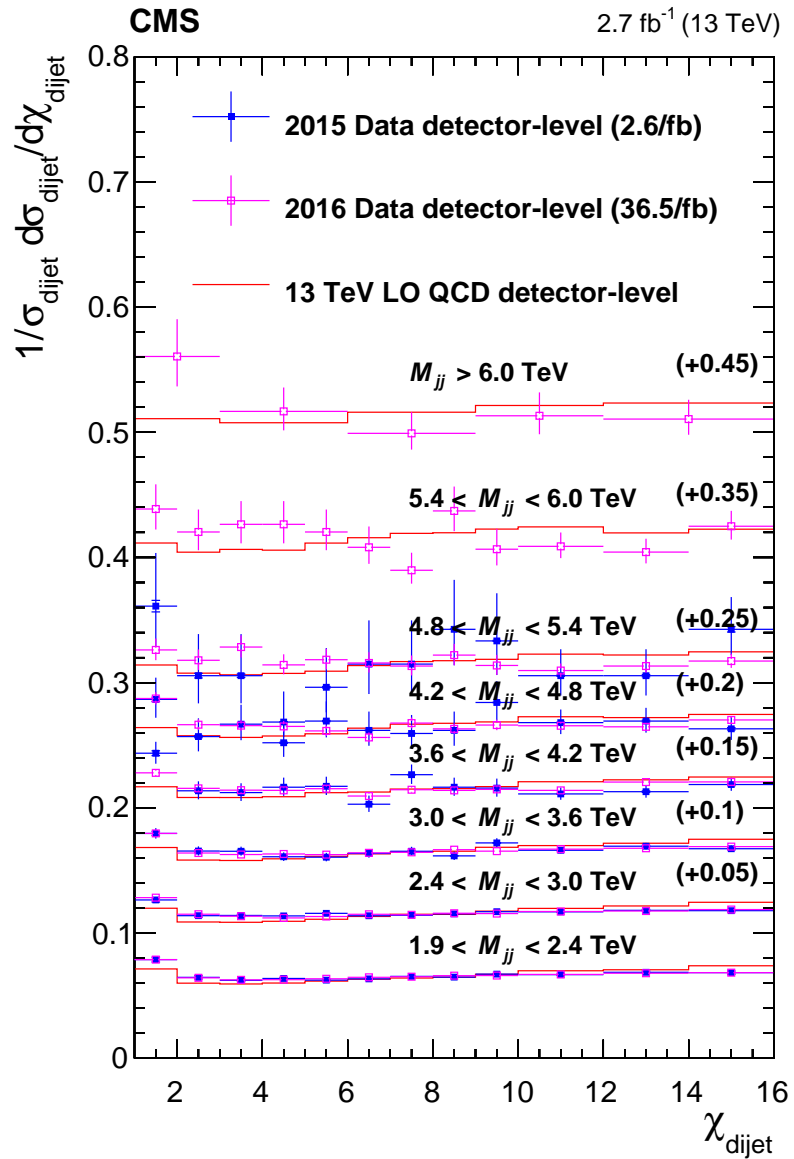


Figure 57: Comparison of 2016 data with LO detector level prediction and 2015 data.

450 7 Search for new physics

451 In this section we explore the sensitivity of this analysis to new physics. In particular, we
 452 extract limits on new physics models with contact interactions (quark compositeness models),
 453 virtual graviton exchanges (ADD model) or quantum black hole productions beyond expected
 454 QCD interactions. First we describe the method of statistical evaluation. Then the observed
 455 and expected limits are presented.

456 7.1 Method of statistical evaluation

We perform a statistical test discriminating between the QCD only hypothesis and the QCD plus New Physics (QCD+NP) hypothesis as a function of the energy scale Λ based on the log-likelihood-ratio

$$457 Q = \text{test statistics} = -2 \ln\left(\frac{L_{QCD+NP}}{L_{QCD}}\right), \quad (8)$$

Here the likelihood functions L_{QCD+NP} and L_{QCD} are modeled as a product of Poisson likelihood functions for each bin in χ and M_{jj} .

$$458 L(x_i \text{ for } i \in \text{bins} | \lambda_i \text{ for } i \in \text{bins}) = \prod_{i \in \text{bins}} \frac{\lambda_i^{x_i}}{x_i!} \cdot e^{-\lambda_i}, \quad (9)$$

459 The λ_i correspond to the entries in each bin of the QCD (QCD+NP) model, the x_i to the entries
 460 of the (pseudo-)data. In each M_{jj} bin the prediction is normalized to the number of data events.
 461 The information on the expected yield from QCD (QCD+NP) in each mass bin is thus not used,
 462 but only the dijet angular distribution shape of QCD (QCD+NP). The systematic uncertainties
 463 are treated as nuisance parameters in the log-likelihood function. The nuisance parameter
 464 for the jet energy scale uncertainty is splitted to 16 nuisance parameters according to the in-
 465 dependent sources of the jet energy scale uncertainty. In contrary to the 2015 data analysis,
 466 the log-likelihoods are maximized with respect to the nuisance parameters, resulting in up to
 467 30% better limits, due to the constraints from low M_{jj} ranges with high data statistics on the
 468 systematic uncertainties.

The asymptotic approximation [70] of the CL_s criterion [71, 72] based on the quantity

$$469 CL_s = \frac{P_{QCD+NP}(Q \geq Q_{obs})}{1 - P_{QCD}(Q \leq Q_{obs})} \quad (10)$$

470 is used to set limits on the new physics scale or mass. The QCD+NP model is excluded at 95%
 471 confidence level if $CL_s < 0.05$. This method prevents exclusion that could result from statistical
 472 fluctuations in situations where one has no sensitivity but may result in a coverage probability
 473 of the corresponding exclusion limits exceeding the nominal confidence level of 95%. While we
 474 marginalized (integrated over) nuisance parameters in the 2015 analysis ("LEP test ststistics"),
 475 we now fit the nuisance parameters and use a profile likehihood ("LHC test statistics").

476 The uncertainties of the measurement are taken into account as follows. Note that only shape
 477 changing systematic uncertainties which do not change the yield are taken into account since
 478 the normalized angular distributions are measured. The systematic uncertainties are modeled
 479 using 3 histograms with varied scales of $-1\sigma, 0\sigma, +1\sigma$ of the expected uncertainty, interpolated
 480 using cubic splines with linear extrapolation beyond $\pm 1\sigma$. The scale is varied according to a
 Gaussian prior probability density function, resulting in combination in a Gaussian distribu-
 481 tion convoluted with the shape variation induced to the χ_{dijet} distributions. The variation is
 482 truncated at 0 events in less than 1% of the cases.

481 The leading systematic uncertainties, namely the jet energy scale and the μ_F , μ_R scales, are
 482 taken into account. For the scale uncertainty the maximum variations of the shape of the χ_{dijet}
 483 distribution are used to model the uncertainty. The $+1\sigma$ (-1σ) histogram is chosen to have
 484 the maximal positive (negative) slope. Note that the choice of the Gaussian prior probability
 485 density function is ambiguous in this case, as the scale uncertainty is just a rough estimator
 486 for higher order perturbative effects and therefore its distribution is unknown. The jet energy
 487 scale uncertainty has been derived independently for each scale of Λ , as it differs from the
 488 effect observed on the QCD distribution. In this way, the effect of event migration between
 489 mass bins is taken into account. As the quark compositeness signal is only prominent in the
 490 higher mass bins, event migrations change the prediction in each mass bin, and has to be taken
 491 into account.

492 We use 'combine' package to calculate the shape limits. An example of datacard (used to cal-
 493 culate limit for V-A+ contact interaction with scale 1.4 TeV) is shown as following:

```
494 imax 5 number of channels
495 jmax 2 number of backgrounds
496 kmax 4 number of nuisance parameters
497 -----
498 shapes * bin0 datacard_shapelimit13TeV_cs_ct14nlo_14000_V-A+_chi2016.root
499           $PROCESS#chi3600_4200_rebin1 $PROCESS#chi3600_4200_rebin1_$SYSTEMATIC
500 shapes * bin1 datacard_shapelimit13TeV_cs_ct14nlo_14000_V-A+_chi2016.root
501           $PROCESS#chi4200_4800_rebin1 $PROCESS#chi4200_4800_rebin1_$SYSTEMATIC
502 shapes * bin2 datacard_shapelimit13TeV_cs_ct14nlo_14000_V-A+_chi2016.root
503           $PROCESS#chi4800_5400_rebin1 $PROCESS#chi4800_5400_rebin1_$SYSTEMATIC
504 shapes * bin3 datacard_shapelimit13TeV_cs_ct14nlo_14000_V-A+_chi2016.root
505           $PROCESS#chi5400_6000_rebin1 $PROCESS#chi5400_6000_rebin1_$SYSTEMATIC
506 shapes * bin4 datacard_shapelimit13TeV_cs_ct14nlo_14000_V-A+_chi2016.root
507           $PROCESS#chi6000_13000_rebin1 $PROCESS#chi6000_13000_rebin1_$SYSTEMATIC
508 -----
509 -----
510 bin 0 1 2 3 4
511 observation 16162.4196777 4052.87298584 1094.68076324 313.176316261 80.103738784
512 -----
513 bin 0 0 0 1 1 1 2 2 2 3 3 3 4 4 4
514 process cs_ct14nlo_14000_V-A+ cs_ct14nlo_14000_V-A+_ALT QCD
515           cs_ct14nlo_14000_V-A+ cs_ct14nlo_14000_V-A+_ALT QCD
516           cs_ct14nlo_14000_V-A+ cs_ct14nlo_14000_V-A+_ALT QCD
517           cs_ct14nlo_14000_V-A+ cs_ct14nlo_14000_V-A+_ALT QCD
518           cs_ct14nlo_14000_V-A+ cs_ct14nlo_14000_V-A+_ALT QCD
519 process -1 0 1 -1 0 1 -1 0 1 -1 0 1
520 rate 16162.4198608 16162.4194946 6.48261643967e-20
521           4052.87297058 4052.87298584 1.69165324736e-20
522           1094.68075562 1094.68076324 4.64662456275e-21
523           313.176315308 313.176317215 1.30458242019e-21
524           80.1037368774 80.1037397385 4.9434771055e-22
525 -----
526 jer shape 1 1 - 1 1 - 1 1 - 1 1 - 1 1 -
527 jes1 shape 1 1 - 1 1 - 1 1 - 1 1 - 1 1 -
528 jes2 shape 1 1 - 1 1 - 1 1 - 1 1 - 1 1 -
```

```

529 jes3 shape 1 1 - 1 1 - 1 1 - 1 1 - 1 1 -
530 jes4 shape 1 1 - 1 1 - 1 1 - 1 1 - 1 1 -
531 jes5 shape 1 1 - 1 1 - 1 1 - 1 1 - 1 1 -
532 jes6 shape 1 1 - 1 1 - 1 1 - 1 1 - 1 1 -
533 jes7 shape 1 1 - 1 1 - 1 1 - 1 1 - 1 1 -
534 jes8 shape 1 1 - 1 1 - 1 1 - 1 1 - 1 1 -
535 jes9 shape 1 1 - 1 1 - 1 1 - 1 1 - 1 1 -
536 jes10 shape 1 1 - 1 1 - 1 1 - 1 1 - 1 1 -
537 jes11 shape 1 1 - 1 1 - 1 1 - 1 1 - 1 1 -
538 jes11 shape 1 1 - 1 1 - 1 1 - 1 1 - 1 1 -
539 jes12 shape 1 1 - 1 1 - 1 1 - 1 1 - 1 1 -
540 jes13 shape 1 1 - 1 1 - 1 1 - 1 1 - 1 1 -
541 jes14 shape 1 1 - 1 1 - 1 1 - 1 1 - 1 1 -
542 jes15 shape 1 1 - 1 1 - 1 1 - 1 1 - 1 1 -
543 jes16 shape 1 1 - 1 1 - 1 1 - 1 1 - 1 1 -
544 pdf shape 1 1 - 1 1 - 1 1 - 1 1 - 1 1 -
545 scale shape 1 1 - 1 1 - 1 1 - 1 1 - 1 1 -
546 -----

```

- 547 The asymptotic CLS analysis is performed in a similar way as in the ATLAS paper. We have
 548 the signal+background ($\mu=1$) and the background-only hypothesis ($\mu=0$) in the datacards,
 549 build a two hypothesis model (like in HiggsJPC:twoHypothesisHiggs), and compute for each
 550 signal hypothesis the observed and expected signal strength limit.
- 551 Figure 58 and 59 summarizes the information entering into the statistical analysis, namely the
 552 data distribution, the simulated background and signal distributions, as well the the systematic
 553 uncertainties.

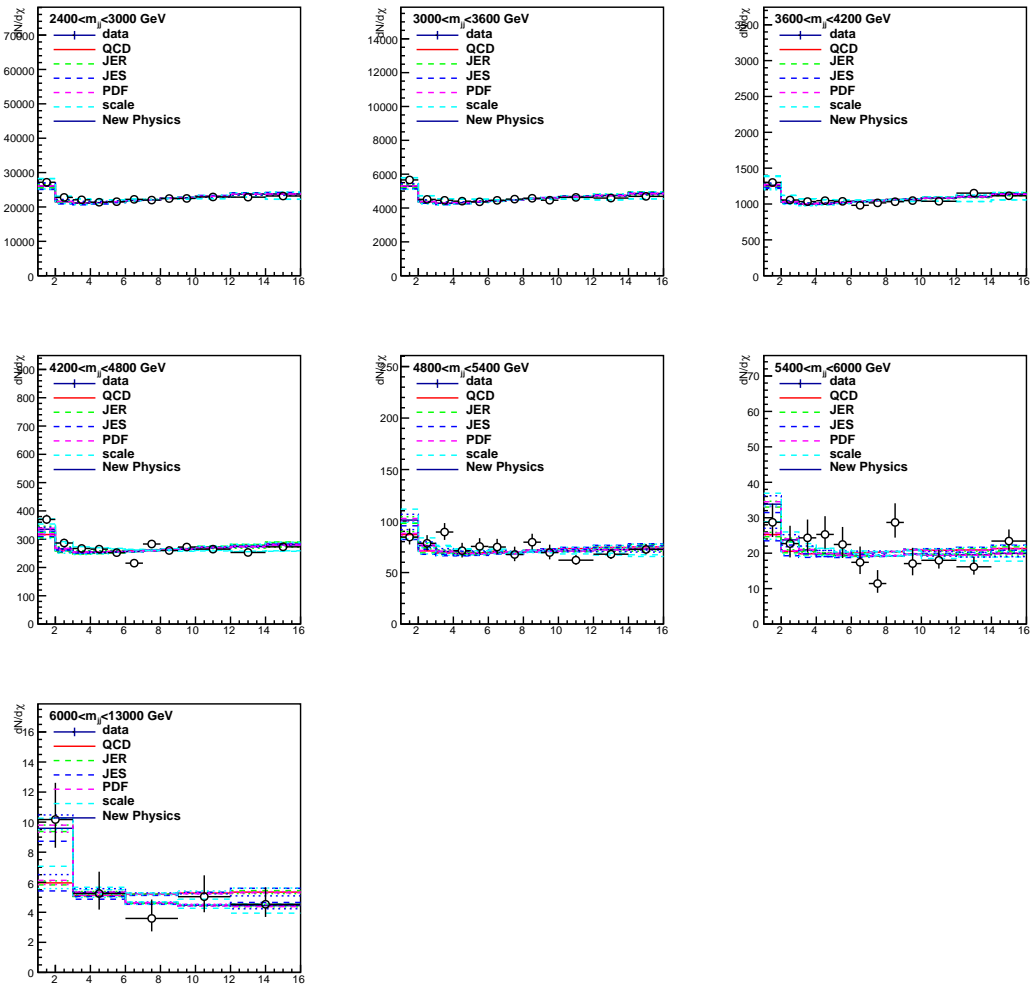


Figure 58: Summary of the input to the statistical analysis for QCD+CI with Λ_{LL}^+ (NLO) = 14 TeV (before splitting JES).

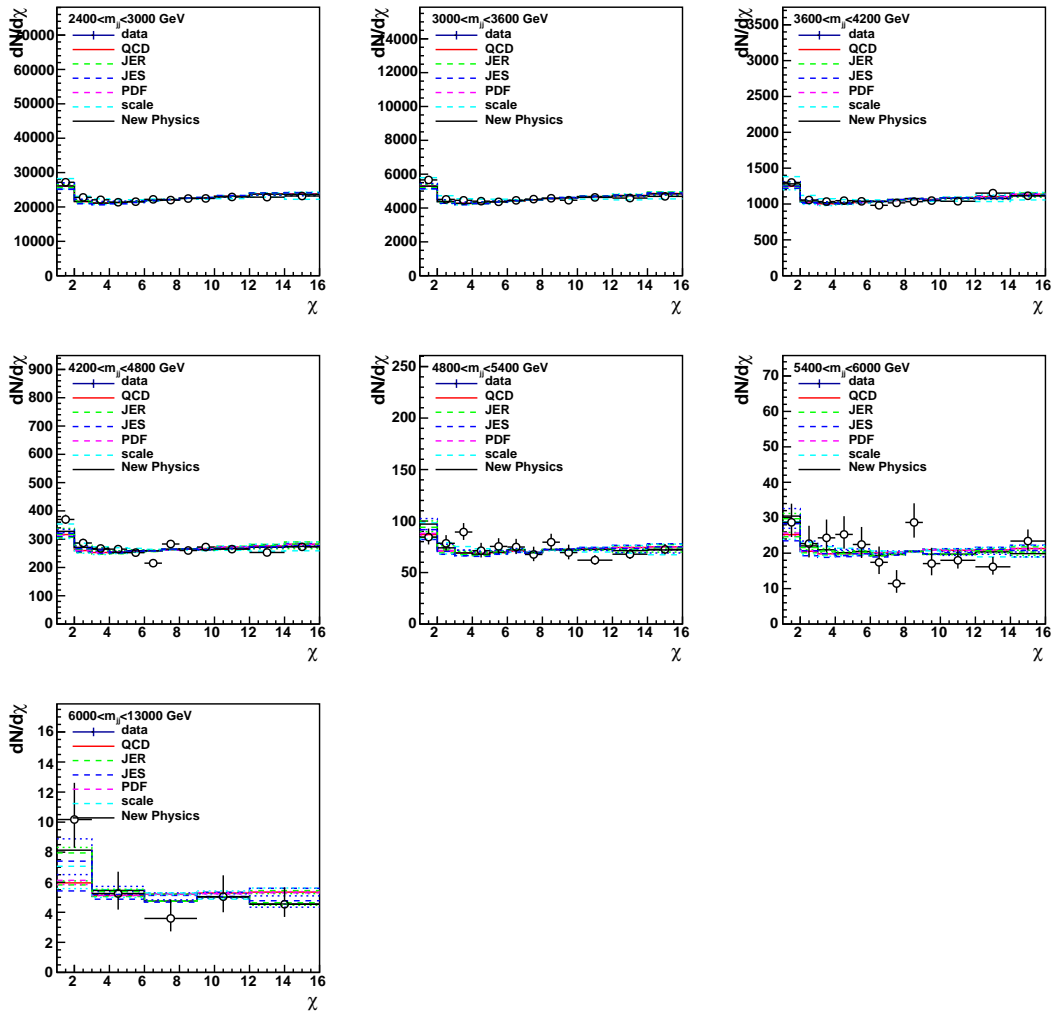


Figure 59: Summary of the input to the statistical analysis for QCD+ADD with Λ_T (GRW) = 12 TeV (before splitting JES).

554 **7.2 Significance of the data**

555 We evaluate the significance of the data distributions in four ways. Firstly, we estimate the
 556 p-values $1 - CL_B = P_{QCD}(Q \leq Q_{obs})$ for each mass using the contact interaction model in the
 557 likelihood ratio which tells how large of an upward fluctuation at low chi as predicted by the
 558 contact interaction and DM mediator models is observed. Secondly, we estimate $P_{QCD}(Q >$
 559 $Q_{obs})$ for each mass using an unphysical model with an opposite effect on the chi distribution
 560 as the contact interaction model in the likelihood ratio which tells how large of a downward
 561 fluctuation at low chi in opposite direction of the contact interaction model is observed. Thirdly,
 562 we calculate a simple χ^2/DOF , summing in quadrature systematic and statistical uncertainties
 563 and assuming that they are uncorrelated between χ bins (which is not true for the systematic
 564 uncertainties). Fourth, we perform a goodness of fit test taking into account all uncertainties
 565 and their correlations based on the saturated model as described in this note [73] and estimate
 566 the significance w.r.t. the expected goodness of fit. The results are summarized in Table 8 and 9.

Table 8: Significance of the data distribution in number of standard deviations.

Model	Mass bins [TeV]	from CI-model	from Anti-Cl-model	from χ^2/DOF	from GOF
$\Lambda_{LL/RR}^+$	6.0	1.8	0.0	1.2	0.4
$\Lambda_{LL/RR}^+$	5.6	0.9	0.0	1.0	0.4
$\Lambda_{LL/RR}^+$	4.8	0.0	0.4	1.9	1.3
$\Lambda_{LL/RR}^+$	4.2	1.7	0.0	0.7	0.3
$\Lambda_{LL/RR}^+$	3.6	0.9	0.0	2.2	0.2
$\Lambda_{LL/RR}^+$	3.0	1.0	0.0	3.4	1.5
$\Lambda_{LL/RR}^+$	2.4	0.1	0.0	3.9	1.7
$\Lambda_{LL/RR}^+$	4.8, 5.4, 6.0	0.9	-	-	1.4
$\Lambda_{LL/RR}^+$	3.6, 4.2, 4.8, 5.4, 6.0	2.4	-	-	0.1

Table 9: Significance of the data distribution in number of standard deviations.

Model	Mass bins [TeV]	from model
$m_{Med} = 2 \text{ TeV}, g_q = 1$	2.4	0.2
$m_{Med} = 2.25 \text{ TeV}, g_q = 1$	2.4	0.2
$m_{Med} = 2.5 \text{ TeV}, g_q = 1$	2.4	0.6
$m_{Med} = 3 \text{ TeV}, g_q = 1$	2.4, 3.0	2.1
$m_{Med} = 3.5 \text{ TeV}, g_q = 1$	2.4, 3.0, 3.6	2.4
$m_{Med} = 4 \text{ TeV}, g_q = 1$	2.4, 3.0, 3.6	2.0
$m_{Med} = 4.5 \text{ TeV}, g_q = 1$	2.4, 3.0, 3.6, 4.2	2.8
$m_{Med} = 5 \text{ TeV}, g_q = 1$	2.4, 3.0, 3.6, 4.2, 4.8, 5.4	2.8
$m_{Med} = 6 \text{ TeV}, g_q = 1$	3.0, 3.6, 4.2, 4.8, 5.4, 6.0	2.7

567 7.3 CI, ADD, and QBH limits

568 Having defined the exclusion criterion $CL_s < 0.05$ at 95% confidence level, one can exclude
 569 parameter ranges for the quark compositeness, extra dimension models and quantum black
 570 hole productions. The quark compositeness model is described by an energy scale Λ . As the
 571 cross section of the contact interaction in the mass bins of the analysis decreases continuously
 572 with increasing Λ , one can set lower limits on the contact interaction scale Λ from the measured
 573 dijet angular distributions. The ADD model is described by an energy scale Λ_T or M_S , which
 574 plays a similar role as the contact interaction scale. The QBHs are studied in context of ADD
 575 model and RS model and can be described by the mass of the QBH. In the following we talk
 576 only about the contact interaction scales Λ , but the same description applies to the ADD scales
 577 Λ_T or M_S and QBHs.

578 The limits are obtained by calculating the CL_s as a function of Λ and finding the crossing point
 579 with $CL_s = 0.05$. In addition to the limit observed in data, it is important to study also the
 580 expected limit given the number of observed data events in each mass bin. The expected limit
 581 quantifies the sensitivity of the experiment independent from statistical fluctuations in the data
 582 and is therefore important for comparisons with other measurements. The expected CL_s is
 583 evaluated by using the log-likelihood-ratio $Q_{(QCD)}$ at the median of the $P_{QCD}(Q)$ instead of
 584 the Q_{obs} of the data. In this way a limit is extracted under the assumption that the data lies at
 585 the center of the expectation for the QCD hypothesis.

586 Additional to the expected limit one can also extract the variation of the expected limit within
 587 the uncertainties. By using the log-likelihood ratio Q at 16% (2.2%) and 84% (97.7%) values of
 588 $P_{QCD}(Q)$, instead of the median (=50%), 1σ (2σ) bands reflecting the variation of the expected
 589 limit, are obtained.

590 The observed and expected limits at 95% C.L. obtained using CLs with profiled nuisance pa-
 591 rameters are listed in Table 10.

Table 10: CLS observed and expected exclusion limits at 95% CL for various CI and extra di-
 mension models.

Model	Observed lower limit (TeV)	Expected lower limit (TeV)
$\Lambda_{LL/RR}^+$ (NLO)	12.7	14.8 ± 0.8
$\Lambda_{LL/RR}^-$ (NLO)	17.6	23.8 ± 3.1
Λ_{VV}^+ (NLO)	14.6	16.6 ± 0.9
Λ_{VV} (NLO)	22.5	31.2 ± 3.9
Λ_{AA}^+ (NLO)	14.7	16.7 ± 0.9
Λ_{AA}^- (NLO)	22.4	30.8 ± 3.6
$\Lambda_{(V-A)}^+$ (NLO)	9.2	11.6 ± 1.0
$\Lambda_{(V-A)}^-$ (NLO)	9.4	11.9 ± 1.1
ADD Λ_T (GRW)	10.3	11.7 ± 0.8
ADD M_S (HLZ) $n_{ED} = 2$	11.0	12.8 ± 0.9
ADD M_S (HLZ) $n_{ED} = 3$	12.2	13.7 ± 0.9
ADD M_S (HLZ) $n_{ED} = 4$	10.3	11.7 ± 0.8
ADD M_S (HLZ) $n_{ED} = 5$	9.3	10.6 ± 0.7
ADD M_S (HLZ) $n_{ED} = 6$	8.7	9.8 ± 0.6
QBH M_{QBH} (ADD6)	8.3	8.7 ± 0.3
QBH M_{QBH} (RS1)	6.0	6.5 ± 0.4
DM (Axial-)vector m_{Med}	2.5–5.0	2.5–5.2

592 The 4 highest mass bins are used for limit setting. Since the nuisance parameters are fitted,
 593 including lower mass bins helps constraining QCD scale uncertainties. In Table 11 and Table 12,
 594 we summarize the limits for $\Lambda_{LL/RR}^+$ and $\Lambda_{LL/RR}^-$ obtained from different combinations of mass
 595 bins.

Table 11: CLS observed and expected limits at 95% confidence level for the $\Lambda_{LL/RR}^+$ (NLO) model obtained from different combinations of mass bins (before splitting JES).

Mass bins [TeV]	Observed limit	Expected limit
6.0-inf	11.4	13.3 ± 1.2
5.4-6.0	12.6	13.1 ± 0.9
4.8-5.4	13.5	12.9 ± 0.8
5.4-6.0, 6.0-inf	12.5	14.0 ± 1.0
4.8-5.4, 5.4-6.0, 6.0-inf	13.7	14.5 ± 0.9
4.2-4.8, 4.8-5.4, 5.4-6.0, 6.0-inf	13.5	14.6 ± 0.9
3.6-4.2, 4.2-4.8, 4.8-5.4, 5.4-6.0, 6.0-inf	13.1	15.2 ± 0.9

Table 12: CLS observed and expected limits at 95% confidence level for the $\Lambda_{LL/RR}^-$ (NLO) model obtained from different combinations of mass bins (before splitting JES).

Mass bins [TeV]	Observed limit	Expected limit
6.0-inf	13.1	16.4 ± 2.3
5.4-6.0	16.0	17.4 ± 2.3
4.8-5.4	19.2	17.8 ± 2.3
5.4-6.0, 6.0-inf	15.5	18.6 ± 2.4
4.8-5.4, 5.4-6.0, 6.0-inf	18.7	20.4 ± 2.7
4.2-4.8, 4.8-5.4, 5.4-6.0, 6.0-inf	18.1	22.0 ± 3.0
3.6-4.2, 4.2-4.8, 4.8-5.4, 5.4-6.0, 6.0-inf	17.4	23.9 ± 3.0

596 As a cross check, we compute LEP-style CLs using the three highest mass bins for limit setting,
 597 since inclusion of lower mass bins do not improve the expected limit. This is demonstrated in
 598 Table 13 and Table 14, where we summarize the limits for $\Lambda_{LL/RR}^+$ and $\Lambda_{LL/RR}^-$ obtained from
 599 different combinations of mass bins.

Table 13: LEP-style CLS (as cross check) observed and expected limits at 95% confidence level for the $\Lambda_{LL/RR}^+$ (NLO) model obtained from different combinations of mass bins (before splitting JES).

Mass bins [TeV]	Observed limit	Expected limit
6.0-inf	11.5	13.8 ± 1.3
5.4-6.0	12.3	13.3 ± 1.5
4.8-5.4	12.4	12.8 ± 1.1
5.4-6.0, 6.0-inf	12.5	14.4 ± 1.5
4.8-5.4, 5.4-6.0, 6.0-inf	12.8	14.0 ± 1.2
4.2-4.8, 4.8-5.4, 5.4-6.0, 6.0-inf	12.2	13.8 ± 1.5
3.6-4.2, 4.2-4.8, 4.8-5.4, 5.4-6.0, 6.0-inf	11.8	13.5 ± 2.2

600 As a cross check, the limits for the CI models are also determined in Tab. 15 for the case in which
 601 the data are not corrected for detector effects and the QCD and NP predictions are smeared to
 602 include the jet p_T resolution effects using the response matrix. The extracted limits are found
 603 to agree with the quoted ones (Tab. 10) within 5%.

Table 14: LEP-style CLS (as cross check) observed and expected limits at 95% confidence level for the $\Lambda_{LL/RR}^-$ (NLO) model obtained from different combinations of mass bins (before splitting JES).

Mass bins [TeV]	Observed limit	Expected limit
6.0-inf	13.2	17.2 ± 2.5
5.4-6.0	15.8	17.7 ± 2.4
4.8-5.4	16.2	17.5 ± 2.8
5.4-6.0, 6.0-inf	15.5	18.9 ± 2.9
4.8-5.4, 5.4-6.0, 6.0-inf	16.4	19.1 ± 3.2
4.2-4.8, 4.8-5.4, 5.4-6.0, 6.0-inf	15.7	19.0 ± 3.4
3.6-4.2, 4.2-4.8, 4.8-5.4, 5.4-6.0, 6.0-inf	15.4	17.5 ± 3.6

604 A comparison between the smeared and the un-smeared distributions for the CI model with $\Lambda_{LL/RR}^- = 23$ TeV can be found in Figure 60

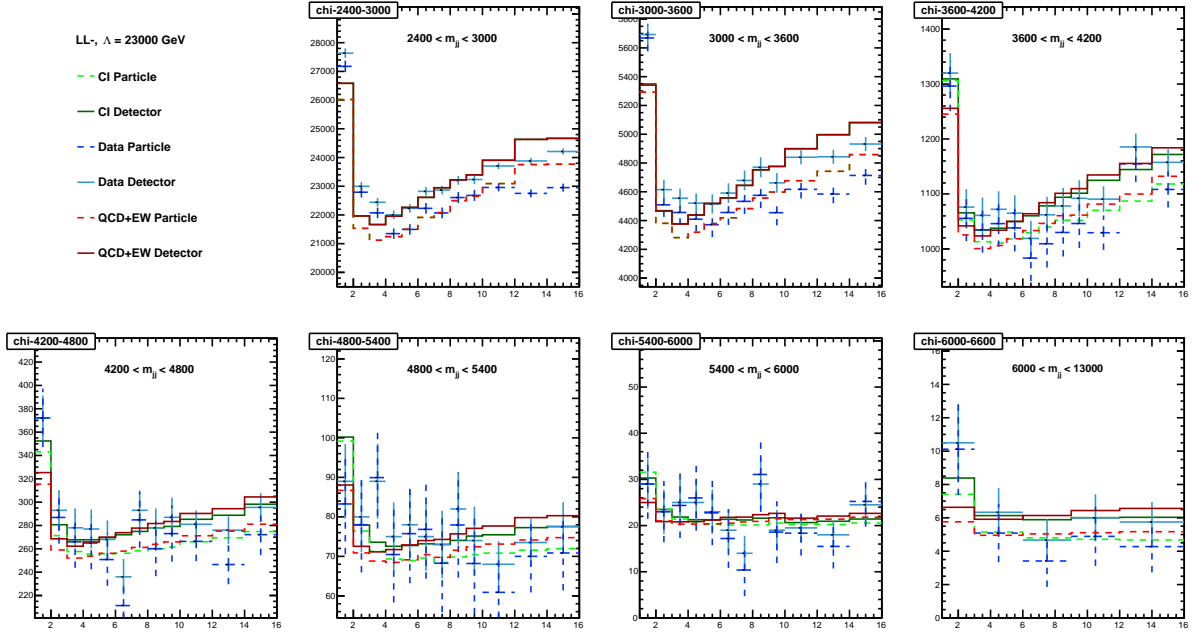


Figure 60: Compare the CI model with $\Lambda_{LL/RR}^- = 23\text{TeV}$ at detector-level and particle-level.

605

Table 15: Observed and expected exclusion limits at 95% CL for the NP models, determined for the case in which the data are not corrected for detector effects.

Model	Observed lower limit (TeV)	Expected lower limit (TeV)
$\Lambda_{\text{LL/RR}}^+$ (NLO)	12.8	14.6 ± 0.8
$\Lambda_{\text{LL/RR}}^-$ (NLO)	17.5	23.5 ± 3.0
Λ_{VV}^+ (NLO)	14.6	16.4 ± 0.8
Λ_{VV}^- (NLO)	22.4	30.7 ± 3.7
Λ_{AA}^+ (NLO)	14.7	16.5 ± 0.8
Λ_{AA}^- (NLO)	22.3	30.6 ± 3.8
$\Lambda_{(\text{V-A})}^+$ (NLO)	9.2	11.5 ± 1.0
$\Lambda_{(\text{V-A})}^-$ (NLO)	9.3	11.8 ± 1.1
ADD Λ_T (GRW)	10.1	11.5 ± 0.7
ADD M_S (HLZ) $n_{ED} = 2$	10.7	12.5 ± 0.8
ADD M_S (HLZ) $n_{ED} = 3$	12.0	13.7 ± 0.8
ADD M_S (HLZ) $n_{ED} = 4$	10.1	11.5 ± 0.7
ADD M_S (HLZ) $n_{ED} = 5$	9.1	10.4 ± 0.6
ADD M_S (HLZ) $n_{ED} = 6$	8.5	9.7 ± 0.6
QBH M_{QBH} (ADD $n_{ED} = 6$)	8.2	8.5 ± 0.4
QBH M_{QBH} (RS $n_{ED} = 1$)	5.9	6.3 ± 0.7

606 7.4 Dark Matter limits

607 Asymptotic LHC-style CLs method are used to calculate limits on the universal quark coupling
 608 of the mediators. Since for all the mediators, high mass tail of the resonance does not contribute
 609 significantly to the limit but introduce sensitivity to PDF uncertainty, for a mediator with mass
 610 M_{Med} , only mass bins that include the mass range $0.5M_{\text{Med}} < m_{jj} < 1.2M_{\text{Med}}$ are used in
 611 the limit setting. Normalized χ_{dijet} distributions for axial-vector and vector mediators with
 612 $g_q = 0.75$ and $g_{\text{DM}} = 1$ combined with QCD background are shown in Figure 61. For each
 613 mediator, χ_{dijet} distributions are only shown in the mass bins which are used for extracting
 614 limits. In a given mass bin, for bigger values of g_q , a larger relative contribution from DM
 615 mediator in the normalized χ_{dijet} distribution is expected since the cross section of the DM
 616 mediator increase when g_q increase.

617 Figure 62 shows the upper limits on the universal quark coupling g_q and the width for a lepto-
 618 phobic (axial-)vector DM mediator as a function of the mediator mass (M_{Med}) with $g_{\text{DM}} = 1$
 619 and $m_{\text{DM}} = 1$ GeV. For mediator masses between 2.5 and 5.0 TeV, this search excludes cou-
 620 plings $g_q \geq 1$, that are not accessible through dijet resonance searches. For the benchmark
 621 model chosen by the dijet resonance searches, in which $g_q = 0.25$, this analysis doesn't have
 622 sensitivity.

623 The obvious question about Figure 62 is why the expected limit goes up and down un-physically,
 624 but this is because we are binning our distributions very coarsely in dijet mass, such that our
 625 sensitivity as a function of resonance mass isn't very smooth, compare to the dijet resonance
 626 search.

The limits for arbitrary dark matter mass (m'_{DM}) as a function of mediator mass (M_{Med}) at fixed
 dark matter coupling ($g_{\text{DM}} = 1$) can be obtained as described below. The cross section for the
 simplified dark matter model can be written by:

$$\sigma = \frac{g_q^4}{\Gamma} \frac{C}{M_{\text{Med}}} \quad (11)$$

where C is a constant and Γ is the total width of the dark matter mediator (Z'). And the partial
 width for $Z' \rightarrow q\bar{q}$ and $Z' \rightarrow \chi\bar{\chi}$ processes can be written by:

$$\Gamma_{\text{vector}}^{q\bar{q}} = \frac{g_q^2 M_{\text{Med}}}{4\pi} \left(1 - 4 \frac{m_q^2}{M_{\text{Med}}^2}\right)^{1/2} \left(1 + 2 \frac{m_q^2}{M_{\text{Med}}^2}\right) \quad (12)$$

$$\Gamma_{\text{vector}}^{\chi\bar{\chi}} = \frac{g_{\text{DM}}^2 M_{\text{Med}}}{12\pi} \left(1 - 4 \frac{m_{\text{DM}}^2}{M_{\text{Med}}^2}\right)^{1/2} \left(1 + 2 \frac{m_{\text{DM}}^2}{M_{\text{Med}}^2}\right) \quad (13)$$

and

$$\Gamma_{\text{axial-vector}}^{q\bar{q}} = \frac{g_q^2 M_{\text{Med}}}{4\pi} \left(1 - 4 \frac{m_q^2}{M_{\text{Med}}^2}\right)^{3/2} \quad (14)$$

$$\Gamma_{\text{axial-vector}}^{\chi\bar{\chi}} = \frac{g_{\text{DM}}^2 M_{\text{Med}}}{12\pi} \left(1 - 4 \frac{m_{\text{DM}}^2}{M_{\text{Med}}^2}\right)^{3/2} \quad (15)$$

for axial-vector or vector mediator, respectively. For arbitrary dark matter mass m'_{DM} with
 $g_{\text{DM}} = 1$ and $m_{\text{DM}} = 1$ GeV and $g_{\text{DM}} = 1$, we have:

$$\sigma = \frac{g_q^4}{\Gamma^{q\bar{q}}(g_q = 1) + \Gamma^{\chi\bar{\chi}}(m_{\text{DM}} = 1, g_{\text{DM}} = 1)} \frac{C}{M_{\text{Med}}} = \frac{g'_q^4}{\Gamma^{q\bar{q}}(g'_q) + \Gamma^{\chi\bar{\chi}}(m'_{\text{DM}}, g_{\text{DM}} = 1)} \frac{C}{M_{\text{Med}}} \quad (16)$$

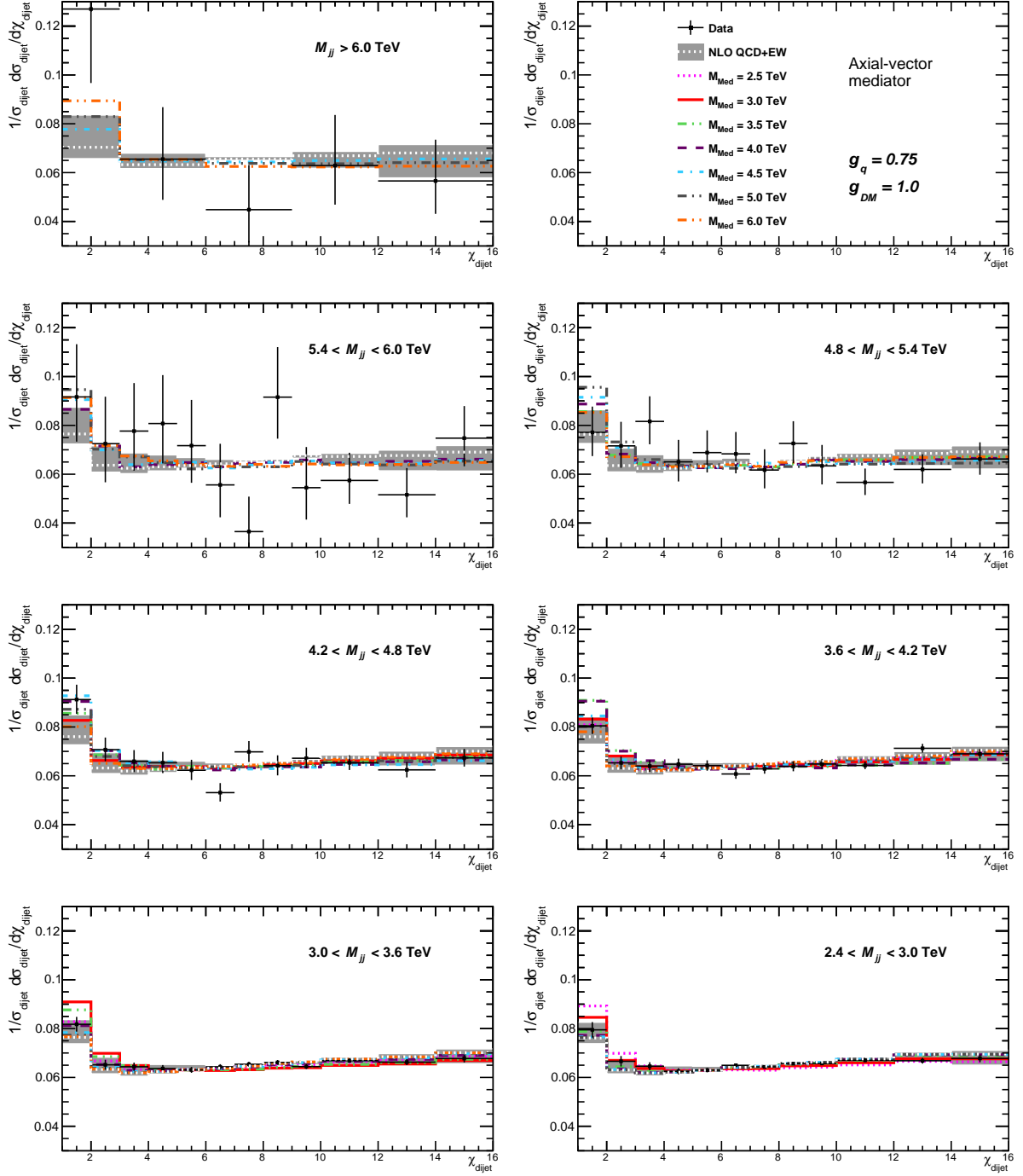


Figure 61: Normalized χ_{dijet} distributions for (axial-)vector mediators at $g_q = 0.75$ and $g_{\text{DM}} = 1$.

Solve Equation 16, we get:

$$g_q = \sqrt{\frac{A + \sqrt{A^2 + 4B}}{2}} \quad (17)$$

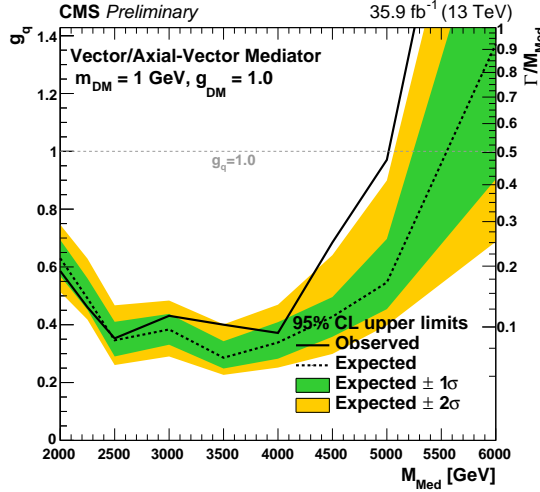


Figure 62: The 95% CL upper limits on the universal quark coupling g_q and the width for a leptophobic (axial-)vector DM mediator as a function of the mediator mass with $g_{DM} = 1$ and $m_{DM} = 1$ GeV. The observed limits (solid), expected limits (dashed) and their variation at the 1 standard deviation level (shaded bands) are shown. A dotted horizontal line show the coupling strength for a benchmark DM mediator with $g_q = 1$. A dashed horizontal line at $g_q = 0.5$ indicates the lower border of the region for which the resonance width predicted in the DM benchmark model with $g_{DM} = 1$ is $> 15\%$ and thus not accessible in dijet resonance searches.

where

$$A = \frac{g'^2 \Gamma^{q\bar{q}}(g'_q)}{\Gamma^{q\bar{q}}(g'_q) + \Gamma^{\chi\bar{\chi}}(m'_{DM}, g_{DM} = 1)} \text{ and } B = \frac{g'^4 \Gamma^{\chi\bar{\chi}}(m_{DM} = 1, g_{DM} = 1)}{\Gamma^{q\bar{q}}(g'_q) + \Gamma^{\chi\bar{\chi}}(m'_{DM}, g_{DM} = 1)} \quad (18)$$

We therefor can transfer the limits for m'_{DM} at given g'_{DM} to the limits for $m_{DM} = 1$ GeV at g_q . Since the mediator width is dominated by the decay width to quarks with $g_q = 1$ and $g_{DM} = 1$, the width change of the mediator due to the dark matter mass change is a minor effect. As an example, for axial-vector mediators, the limits for $m_{DM} = 2500$ GeV with $g_{DM} = 1$ and $g_q = 1$ correspond to the limits for $m_{DM} = 1$ GeV with $g_{DM} = 1$ and $g_q = 1.03$ for $2m_{DM} < M_{Med}$ or $g_q = 1.02$ for $2m_{DM} > M_{Med}$.

The resulting exclusion limits for dark matter mass as a function of mediators mass with $g_q = 1$ and $g_{DM} = 1$ are shown in Figure 63.

The 95% CL observed (solid) and expected (dashed) excluded regions in the plane of dark matter mass vs. mediator mass, for an (left) axial-vector mediator and a (right) vector mediator for a DM benchmark model with $g_{DM} = 1$ and $g_q = 1$.

The limits for the dark matter models are also extracted using data without the unfolding correction. The QCD predictions are smeared to include the detector effects using the 2D response matrix. The DM predictions are smeared using the 2D response matrix and the crystal-ball parameterization of the jet p_T resolution. The resulting limits with the response matrix smeared and the crystal-ball smeared predictions can be found in Figure 64.

Detailed comparisons for the background and the signal distributions at particle-level, response matrix smeared detector-level, and crystal-ball function smeared detector-level can be found in Figure 65 for $M_{Med} = 2.0$ TeV and $g_q = 0.5$, Figure 66 for $M_{Med} = 2.0$ TeV and

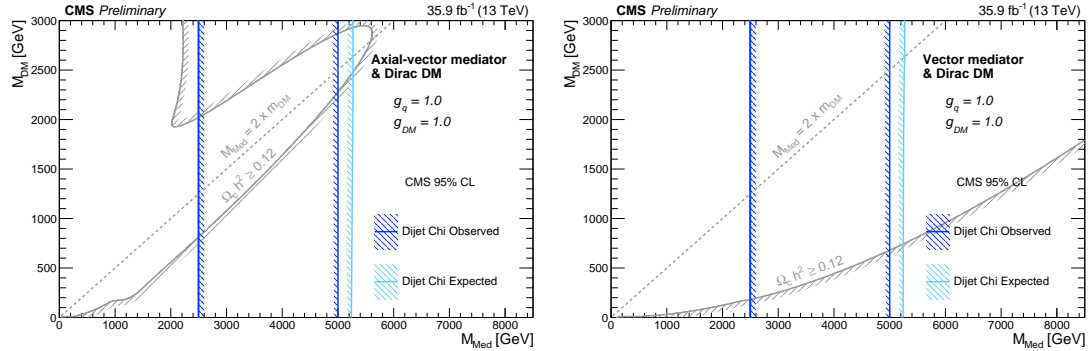


Figure 63: The 95% CL observed (solid) and expected (dashed) excluded regions in the plane of dark matter mass vs. mediator mass, for an (left) axial-vector mediator and a (right) vector mediator for a DM benchmark model with $g_{DM} = 1$ and $g_q = 1$ are compared to constraints from the cosmological relic density of DM (light gray) determined from astrophysical measurements and MADDAM version 2.0.6 [68, 69].

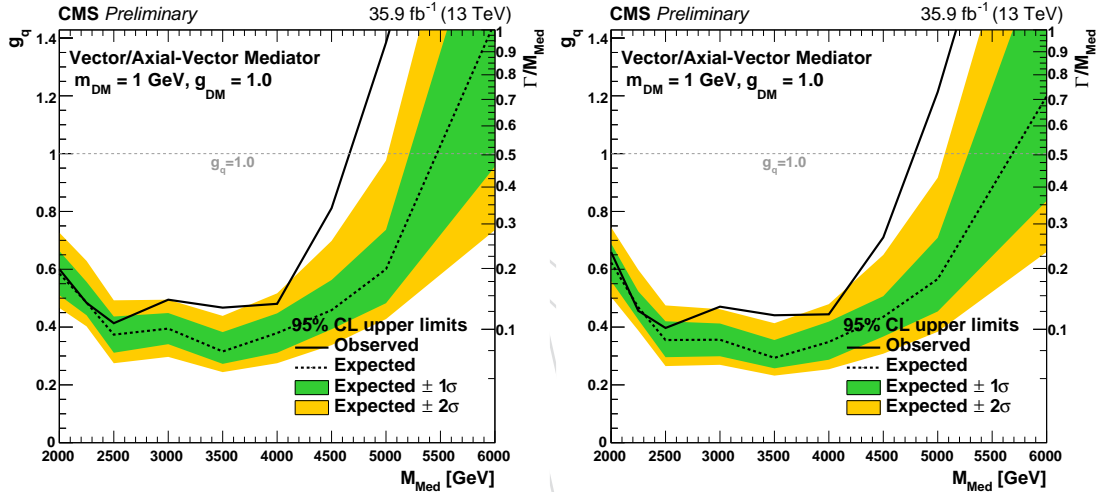


Figure 64: The 95% CL upper limits on the universal quark coupling g_q and the width for a leptophobic (axial-)vector DM mediator as a function of the mediator mass with $g_{DM} = 1$ and $m_{DM} = 1$ GeV. The limits are extracted using data at detector-level, QCD predictions smeared with the response matrix, and DM models smeared with the response matrix (left) and the crystal-ball function (right).

646 $g_q = 0.75$, Figure 66 for $M_{Med} = 2.0$ TeV and $g_q = 1.0$, Figure 68 for $M_{Med} = 2.5$ TeV and
 647 $g_q = 0.3$, Figure 69 for $M_{Med} = 2.5$ TeV and $g_q = 0.5$, Figure 70 for $M_{Med} = 3.0$ TeV and
 648 $g_q = 0.3$, Figure 71 for $M_{Med} = 3.0$ TeV and $g_q = 0.5$, Figure 72 for $M_{Med} = 3.5$ TeV and
 649 $g_q = 0.3$, Figure 73 for $M_{Med} = 4.0$ TeV and $g_q = 0.5$, Figure 74 for $M_{Med} = 5.0$ TeV and
 650 $g_q = 0.5$, Figure 75 for $M_{Med} = 5.0$ TeV and $g_q = 0.75$, and Figure 76 for $M_{Med} = 6.0$ TeV and
 651 $g_q = 1.0$. Both pre-fit and post-fit signal and background distributions are shown in the plots.

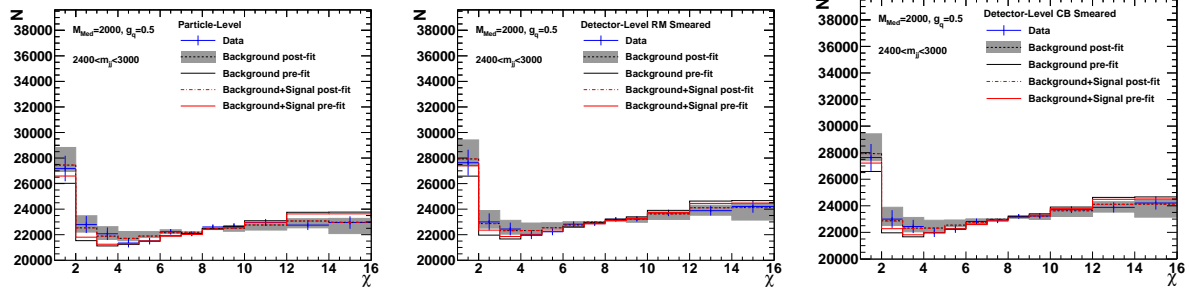


Figure 65: Data, background, and signal pre-fit and post-fit distributions at particle-level, response matrix smeared detector-level, and crystal ball smeared detector-level.

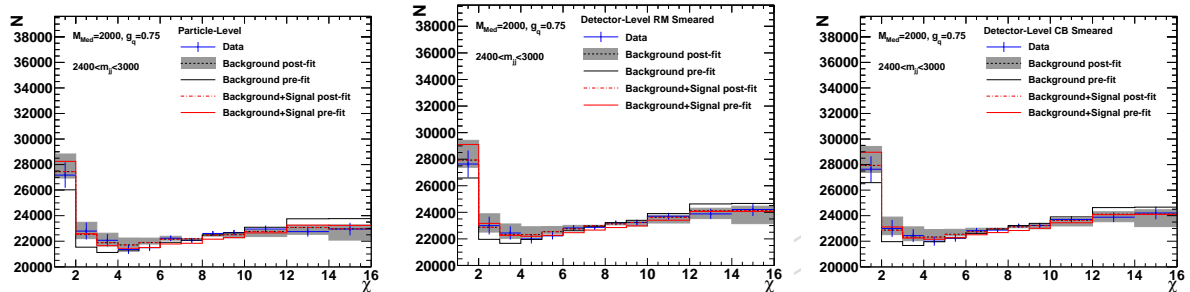


Figure 66: Data, background, and signal pre-fit and post-fit distributions at particle-level, response matrix smeared detector-level, and crystal ball smeared detector-level.

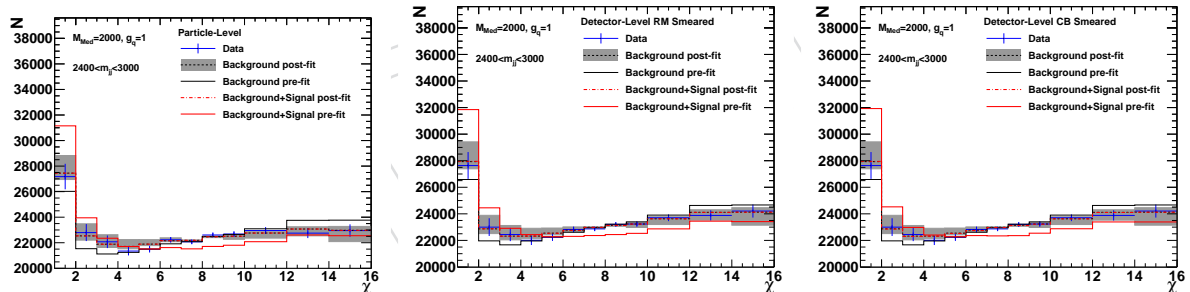


Figure 67: Data, background, and signal pre-fit and post-fit distributions at particle-level, response matrix smeared detector-level, and crystal ball smeared detector-level.

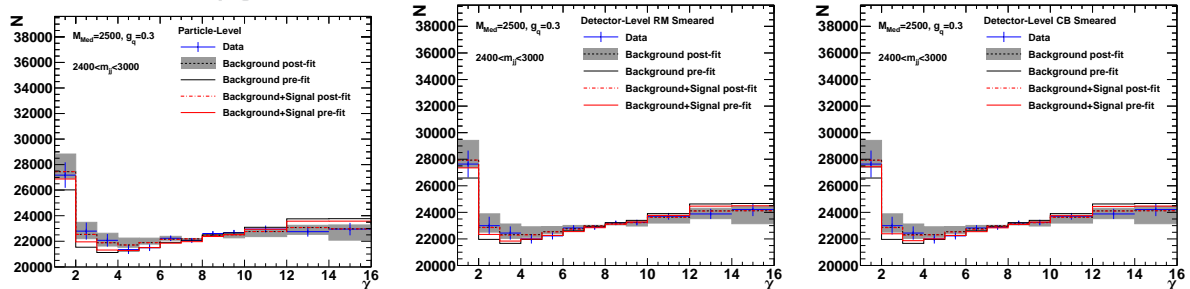


Figure 68: Data, background, and signal pre-fit and post-fit distributions at particle-level, detector-level from response matrix smearing, and detector-level from crystal ball smearing for DM model with $M_{\text{Med}} = 2.5$ TeV and $g_q = 0.3$.

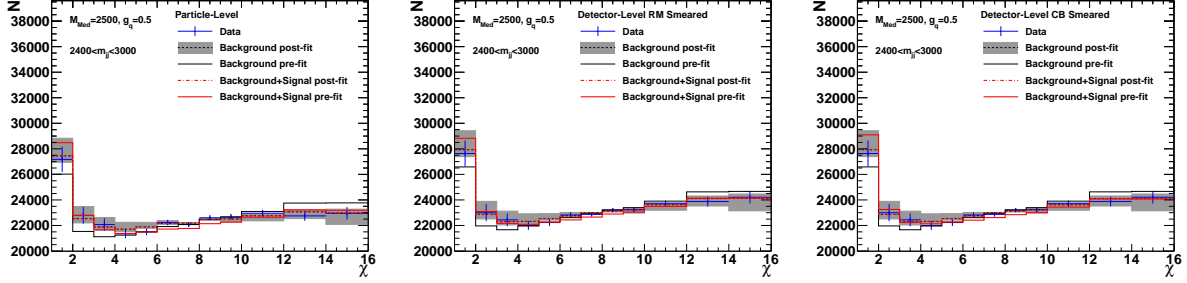


Figure 69: Data, background, and signal pre-fit and post-fit distributions at particle-level, response matrix smeared detector-level, and crystal ball smeared detector-level.

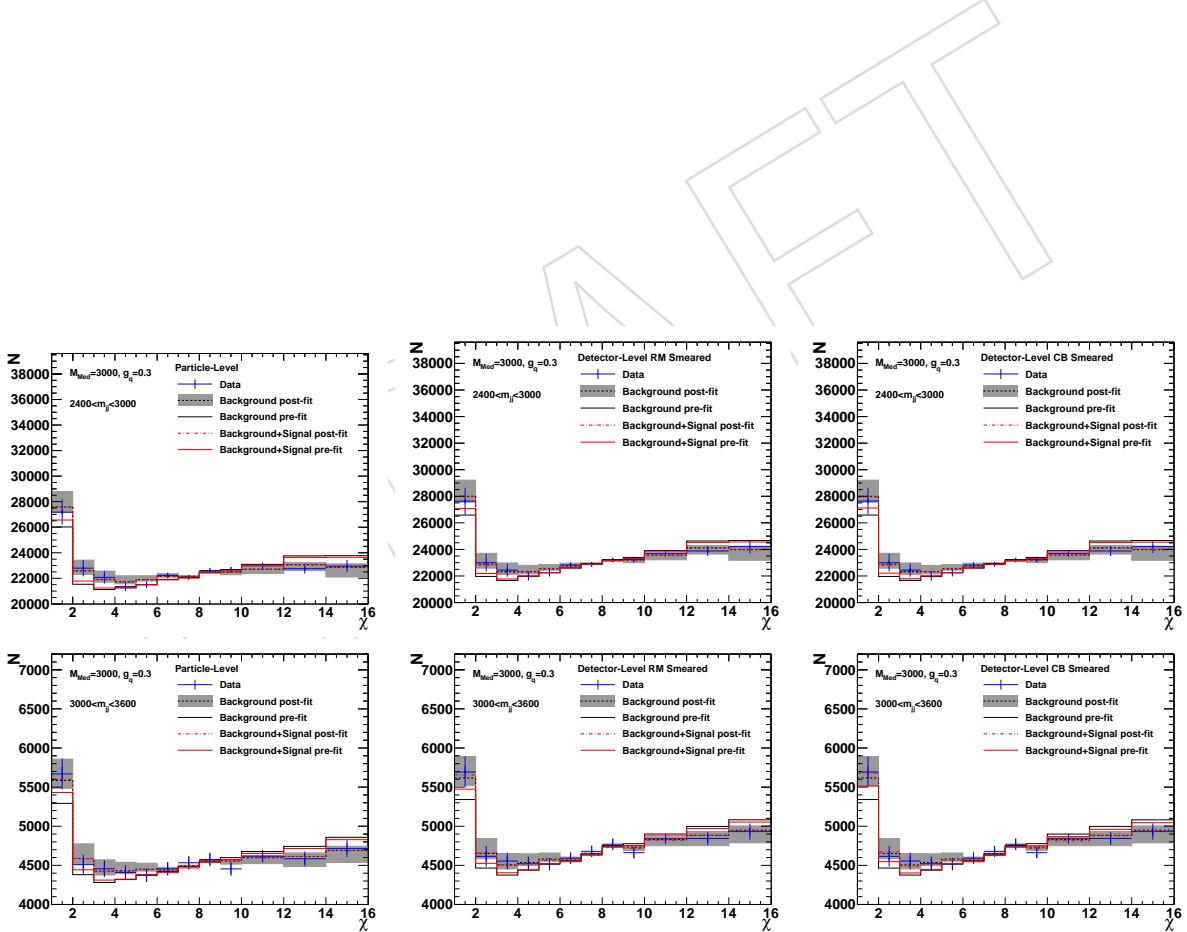


Figure 70: Data, background, and signal pre-fit and post-fit distributions at particle-level, response matrix smeared detector-level, and crystal ball smeared detector-level.

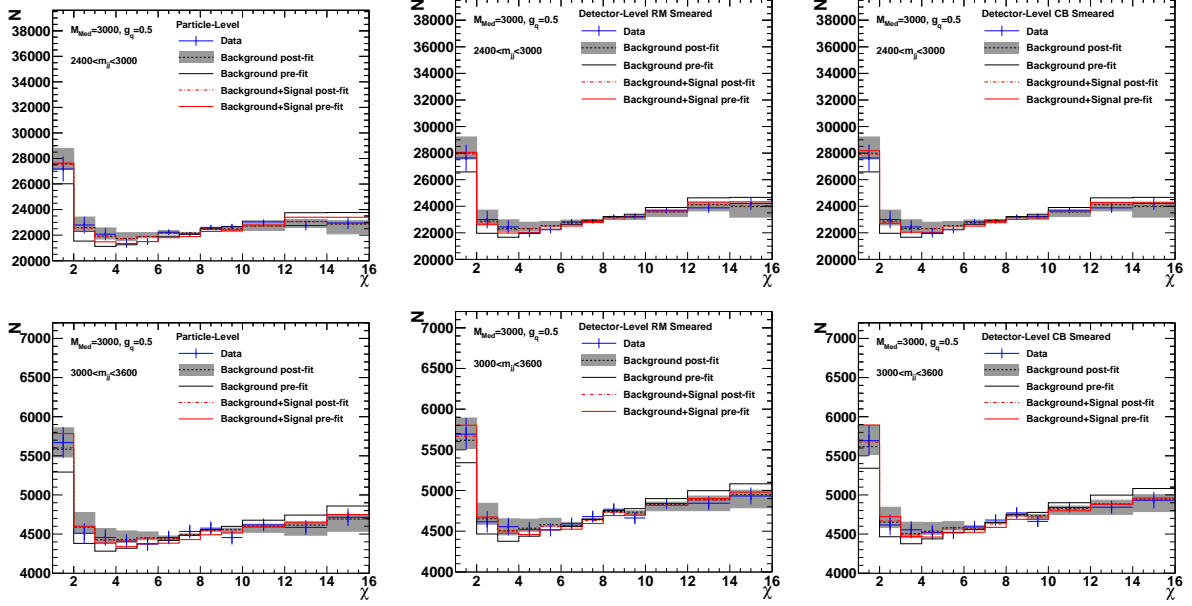


Figure 71: Data, background, and signal pre-fit and post-fit distributions at particle-level, response matrix smeared detector-level, and crystal ball smeared detector-level.

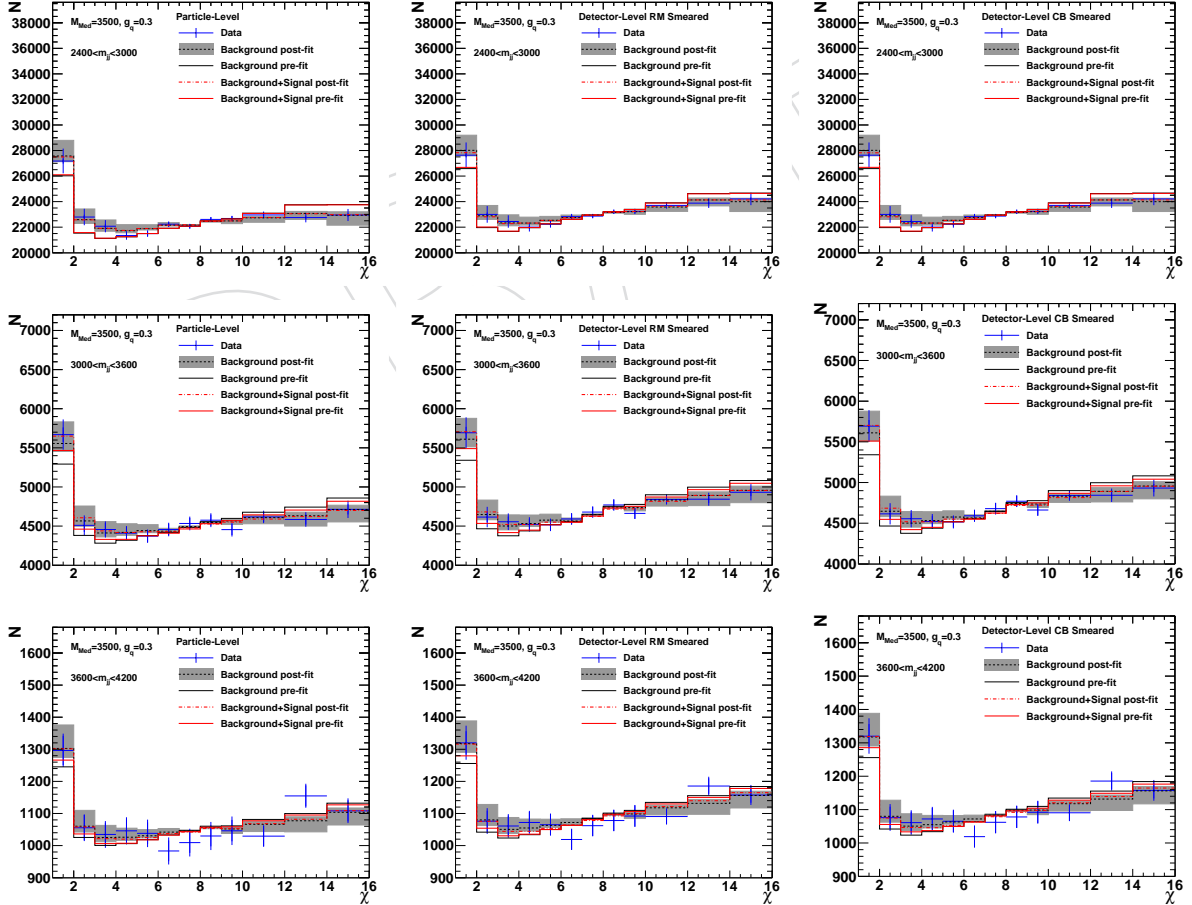


Figure 72: Data, background, and signal pre-fit and post-fit distributions at particle-level, response matrix smeared detector-level, and crystal ball smeared detector-level.

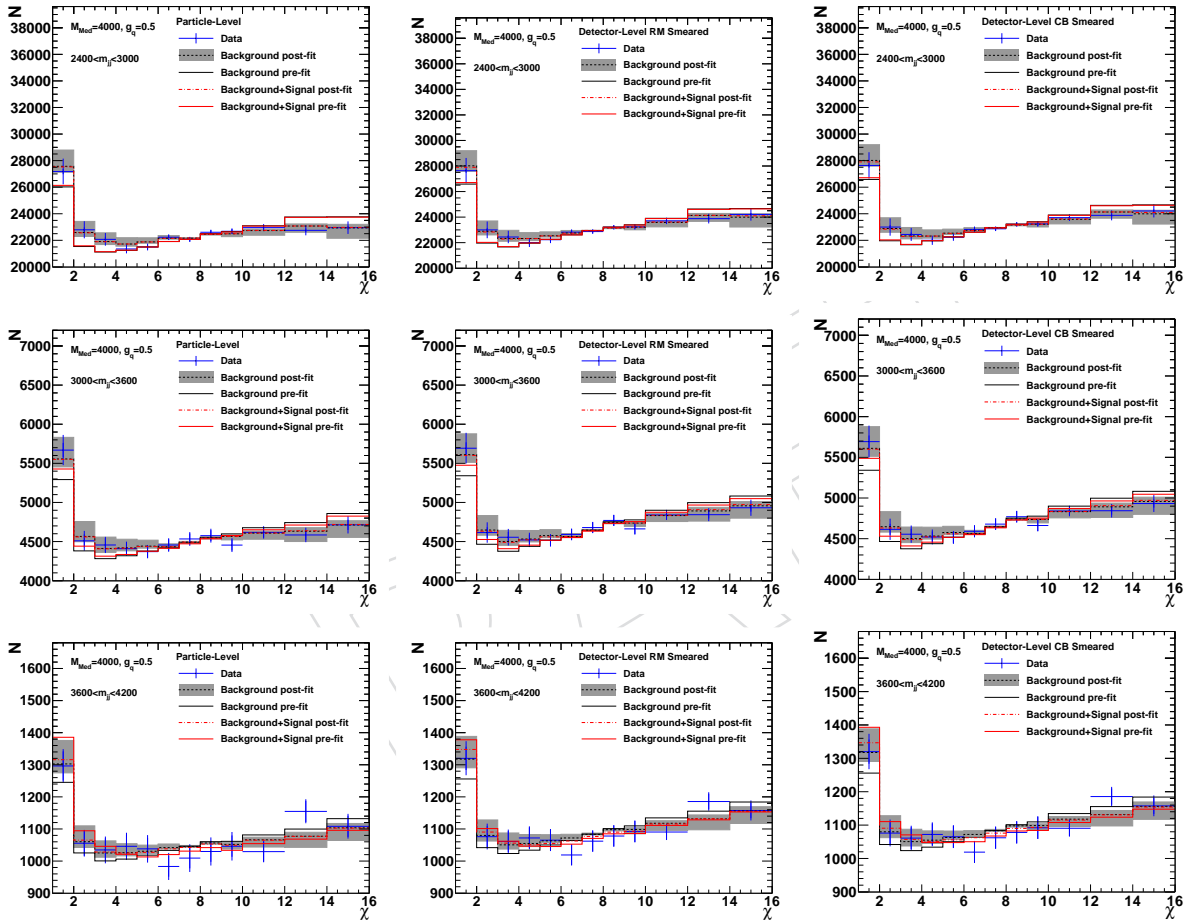


Figure 73: Data, background, and signal pre-fit and post-fit distributions at particle-level, response matrix smeared detector-level, and crystal ball smeared detector-level.

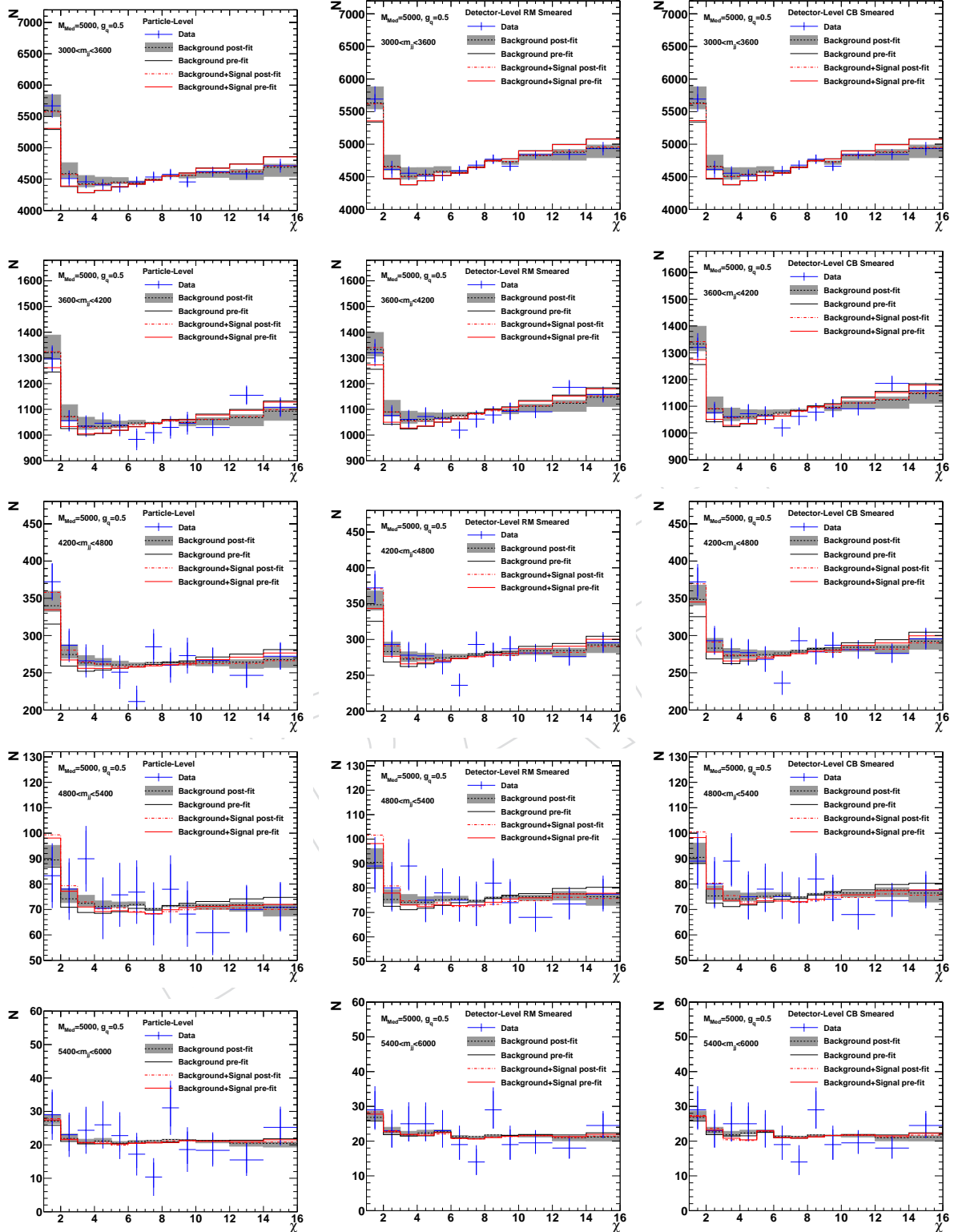


Figure 74: Data, background, and signal pre-fit and post-fit distributions at particle-level, response matrix smeared detector-level, and crystal ball smeared detector-level.

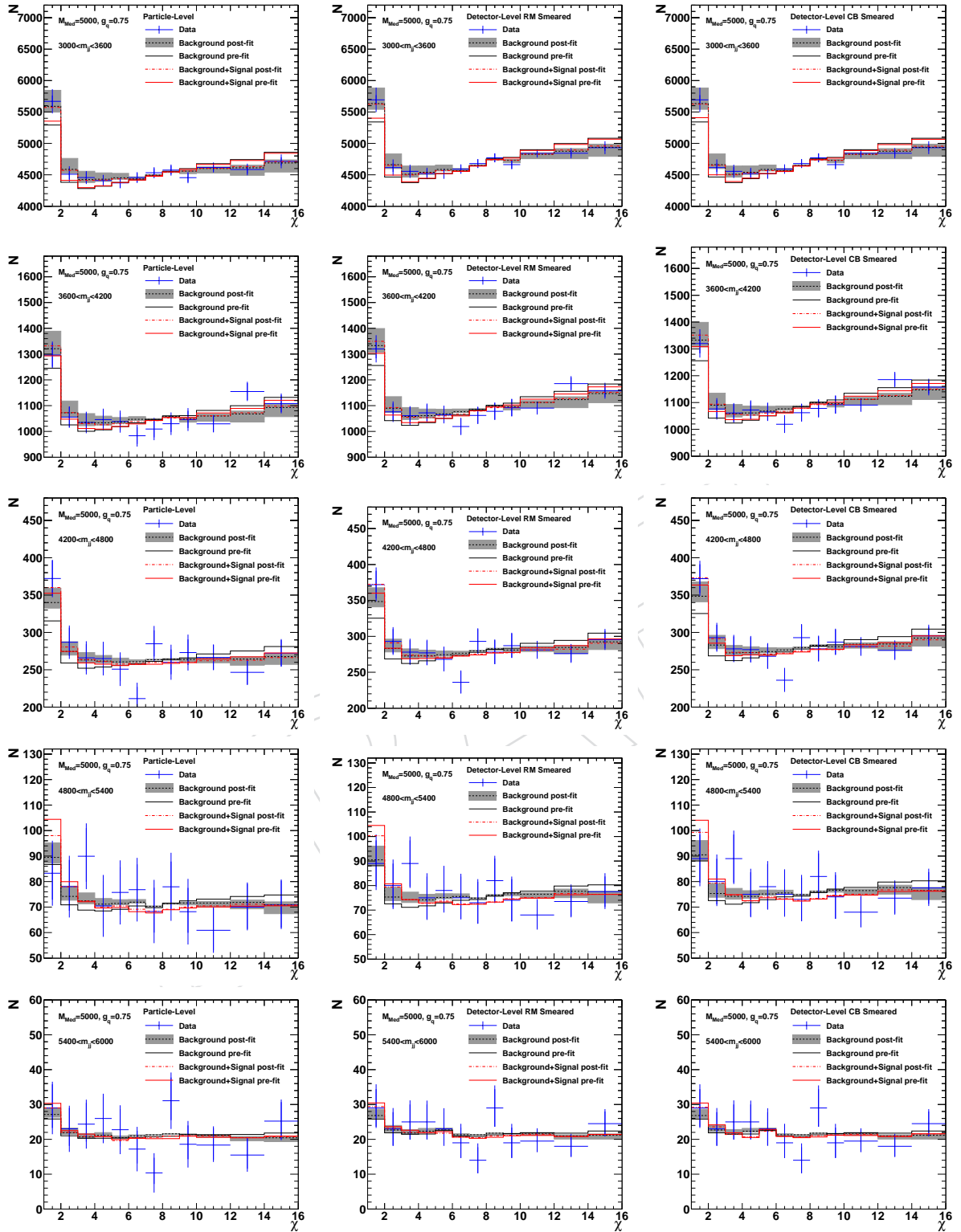


Figure 75: Data, background, and signal pre-fit and post-fit distributions at particle-level, response matrix smeared detector-level, and crystal ball smeared detector-level.

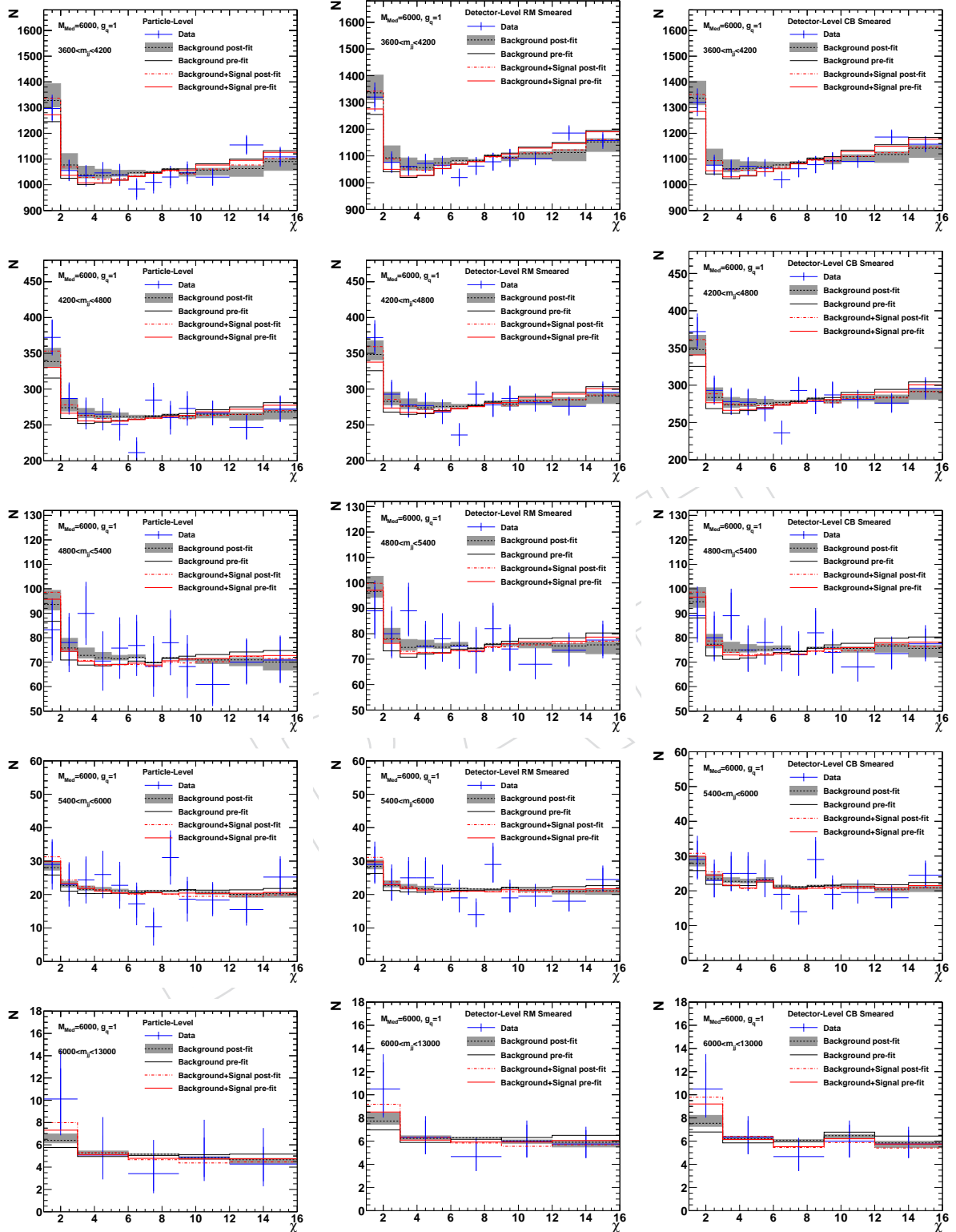


Figure 76: Data, background, and signal pre-fit and post-fit distributions at particle-level, response matrix smeared detector-level, and crystal ball smeared detector-level.

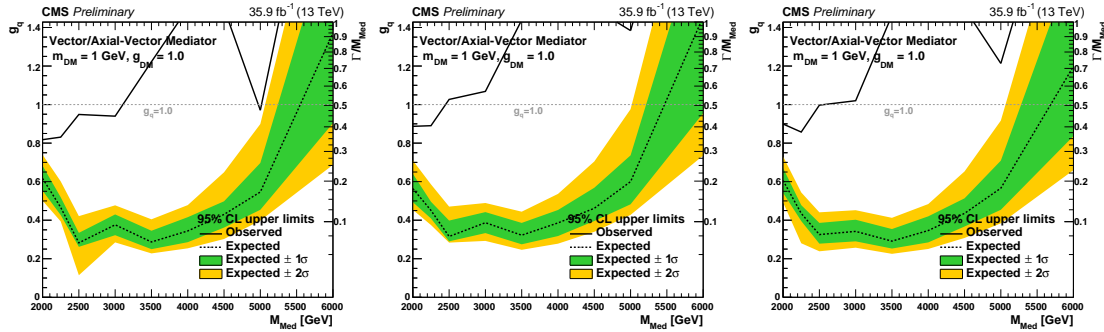


Figure 77: Results for the injection tests with particle-level (left), response matrix smeared detector-level (middle), and crystal-ball smeared detector-level (right) distributions.

652 Signal injection tests are performed for particle-level, response matrix smeared detector-level,
 653 and crystal-ball smeared detector-level limits. Signals correspond to $g_q = 0.75$ in the DM
 654 model for each mediator masses with 2.0, 2.25, 3.0, 3.5, 4.0, and 4.5 TeV are added to the data.
 655 Maximum likelihood fits are performed for the signal + background distributions to the mod-
 656 ified data distributions. The fitted signal strengths are shown in Table 16 and are compared to
 657 those from the fits to the unmodified data distributions. The fitted signal strengths from mod-
 658 ified data distributions converge to 1 as expected. The results in Table 16 are for crystal-ball
 659 smeared detector-level distributions. Results for particle-level distributions and response ma-
 660 trix smeared distributions can be found in Table 18 and Table 17. The limits for the modified
 661 data can be found in Figure 77. As expected, for the data + $g_q = 0.75$ signal distributions, we
 662 get observed limits greater than 7.5.

Table 16: Fitted signal strengths from signal + background fit to data + signal distributions are compared to those from the fits to the data only distributions.

Mediator Mass (TeV)	Fitted μ (Data)	Fitted μ (Data + Signal)
2.0	0.35	1.07
2.25	0.01	0.98
2.5	0.27	1.05
3.0	0.48	1.11
3.5	0.53	1.13
4.0	0.55	1.14
4.5	0.75	1.24

Table 17: Fitted signal strengths from signal + background fit to data + signal distributions are compared to those from the fits to the data only distributions. Comparison is made at the response matrix smeared detector-level.

Mediator Mass (TeV)	Fitted μ (Data)	Fitted μ (Data + Signal)
2.0	0.21	1.02
2.25	0.14	1.01
2.5	0.29	1.06
3.0	0.51	1.12
3.5	0.55	1.14
4.0	0.58	1.15
4.5	0.80	1.27

Table 18: Fitted signal strengths from signal + background fit to data + signal distributions are compared to those from the fits to the data only distributions. Comparison is made at the particle-level.

Mediator Mass (TeV)	Fitted μ (Data)	Fitted μ (Data + Signal)
2.0	0.002	0.89
2.25	0.001	0.94
2.5	0.13	1.01
3.0	0.36	1.05
3.5	0.44	1.08
4.0	0.40	1.07
4.5	0.71	1.21

663 8 Summary

664 The dijet angular distributions in M_{jj} bins have been measured at CMS using LHC data taken in
665 2016 at 13 TeV with an integrated luminosity of 35.9 fb^{-1} . The χ_{dijet} distributions are compared
666 to theoretical predictions from NLO. The data are found in good agreement with the theory
667 predictions. Limits at the 95 % CL are set on quark compositeness, large extra dimension sig-
668 natures, Quantum black hole productions, and simplified models of quark and dark matter
669 interactions. A new lower limit at the 95% confidence level of $g_q > 1$ on the universal quark
670 coupling of a axial-vector (vector) dark matter mediator with masses between 2.5 and 5.0 (4.4)
671 TeV is set in a region that is not accessible through dijet resonance searches. The lower limits
672 for the contact interaction scale Λ range from 9.1 to 22.2 TeV. The lower limits for the scales of
673 ADD models, Λ_T (GRW) and M_S (HLZ), are in the range of 8.9 – 12.6 TeV. Quantum black hole
674 production scales in the ADD $n_{\text{ED}} = 6$ model of up to 8.3 TeV and in the Randall–Sundrum
675 $n_{\text{ED}} = 1$ model of up to 6.0 TeV are excluded and this analysis provides the most stringent set
676 of limits on ADD models.

DRAFT

677 References

- 678 [1] "D0 Collaboration", "Measurement of dijet angular distributions at $\sqrt{s} = 1.96 \text{ tev}$ and
679 searches for quark compositeness and extra spatial dimensions", *Phys. Rev. Lett.* **103**
680 (2009) 191803, doi:10.1103/PhysRevLett.103.191803.
- 681 [2] "D0 Collaboration", "High- p_T jets in $p\bar{p}$ collisions at $\sqrt{s} = 630$ and 1800 gev", *Phys. Rev.*
682 *D* **64** (2001) 032003, doi:10.1103/PhysRevD.64.032003.
- 683 [3] CDF Collaboration, "Measurement of dijet angular distributions at cdf", [*Erratum-ibid.*
684 **78**, 4307 (1997)] *Phys. Rev. Lett.* **77** (1996) 5336, doi:10.1103/PhysRevLett.77.5336.
- 685 [4] ATLAS Collaboration, "Search for new phenomena in dijet angular distributions in
686 proton-proton collisions at $\text{sqrt}(s) = 8 \text{ tev}$ measured with the atlas detector", *Phys. Rev.*
687 *Lett.* **114** (2015) 221802, doi:10.1103/PhysRevLett.114.221802.
- 688 [5] ATLAS Collaboration, "Atlas search for new phenomena in dijet mass and angular
689 distributions using pp collisions at $\sqrt{s} = 7 \text{ tev}$ ", *JHEP* **1301** (2013) 029,
690 doi:10.1007/JHEP01(2013)029.
- 691 [6] ATLAS Collaboration, "Search for new physics in dijet mass and angular distributions in
692 pp collisions at $\sqrt{s} = 7 \text{ tev}$ measured with the atlas detector", *New J. Phys.* **13** (2011)
693 053044, doi:10.1088/1367-2630/13/5/05044.
- 694 [7] ATLAS Collaboration, "Search for quark contact interactions in dijet angular
695 distributions in pp collisions at $\sqrt{s} = 7 \text{ tev}$ measured with the atlas detector", *Phys. Lett.*
696 **B694** (2010) 327, doi:10.1016/j.physletb.2010.10.021.
- 697 [8] ATLAS Collaboration, "Search for new phenomena in dijet mass and angular
698 distributions from pp collisions at $\sqrt{s} = 13 \text{ TeV}$ with the ATLAS detector", *Phys. Lett. B*
699 **754** (2016) 302–322, doi:10.1016/j.physletb.2016.01.032, arXiv:1512.01530.
- 700 [9] CMS Collaboration, "Search for quark contact interactions and extra spatial dimensions
701 using dijet angular distributions in proton-proton collisions at $\text{sqrt}(s) = 8 \text{ tev}$ ", *Phys. Lett.*
702 *B* **746** (2015) 79, doi:10.1016/j.physletb.2015.04.042.
- 703 [10] CMS Collaboration, "Search for quark compositeness in dijet angular distributions from
704 pp collisions at $\sqrt{s} = 7 \text{ tev}$ ", *JHEP* **05** (2012) 055, doi:10.1007/JHEP05(2012)055.
- 705 [11] CMS Collaboration, "Measurement of dijet angular distributions and search for quark
706 compositeness in pp collisions at $\sqrt{s} = 7 \text{ tev}$ ", *Phys. Rev. Lett.* **106** (2011) 201804,
707 doi:10.1103/PhysRevLett.106.201804.
- 708 [12] CMS Collaboration, "Search for quark compositeness with the dijet centrality ratio in pp
709 collisions at $\sqrt{s}=7 \text{ tev}$ ", *Phys. Rev. Lett.* **105** (2010) 262001,
710 doi:10.1103/PhysRevLett.105.262001.
- 711 [13] CMS Collaboration, "Search for new physics with dijet angular distributions in
712 proton-proton collisions at $\text{sqrt}(s) = 13 \text{ TeV}$ ", *submitted to JHEP* (2017)
713 arXiv:1703.09986.
- 714 [14] E. Eichten, K. Lane, and M. Peskin, "New tests for quark and lepton substructure", *Phys.*
715 *Rev. Lett.* **50** (1983) 811, doi:10.1103/PhysRevLett.50.811.

- 716 [15] E. Eichten et al., "Supercollider physics", *Rev. Mod. Phys.* **56** (1984) 579,
717 doi:10.1103/RevModPhys.56.579.
- 718 [16] K. Nakamura et al. (Particle Data Group), "Review of particle physics", *J. Phys. G: Nucl.
719 Part. Phys.* **37** (2010) 075021, doi:10.1088/0954-3899/37/7A/075021.
- 720 [17] CMS Collaboration, "Search for contact interactions using the inclusive jet pt spectrum in
721 pp collisions at $\sqrt{s} = 7$ tev", *Phys. Rev. D* **87** (2013) 052017,
722 doi:10.1103/PhysRevD.87.052017.
- 723 [18] N. Arkani-Hamed, S. Dimopoulos, and G. Dvali, "The hierarchy problem and new
724 dimensions at a millimeter", *Phys. Lett. B* **429** (1998) 263,
725 doi:10.1016/S0370-2693(98)00466-3.
- 726 [19] N. Arkani-Hamed, S. Dimopoulos, and G. Dvali, "Phenomenology, astrophysics and
727 cosmology of theories with sub-millimeter dimensions and tev scale quantum gravity",
728 *Phys. Rev. D* **59** (1999) 086004, doi:10.1103/PhysRevD.59.086004.
- 729 [20] G. Giudice, R. Rattazzi, and J. Wells, "Quantum gravity and extra dimensions at
730 high-energy colliders", *Nucl. Phys. B* **544** (1999) 3,
731 doi:10.1016/S0550-3213(99)00044-9.
- 732 [21] T. Han, J. Lykken, and R. Zhang, "On kaluza-klein states from large extra dimensions",
733 *Phys. Rev. D* **59** (1999) 105006, doi:10.1103/PhysRevD.59.105006.
- 734 [22] K. Cheung and G. Landsberg, "Drell-Yan and diphoton production at hadron colliders
735 and low scale gravity model", *Phys. Rev. D* **62** (2000) 076003,
736 doi:10.1103/PhysRevD.62.076003, arXiv:hep-ph/9909218.
- 737 [23] CMS Collaboration, "Search for large extra dimensions in dimuon and dielectron events
738 in pp collisions at $\sqrt{s} = 7$ tev", *Phys. Lett. B* **711** (2012) 15,
739 doi:10.1016/j.physletb.2012.03.029.
- 740 [24] CMS Collaboration, "Search for physics beyond the standard model in dilepton mass
741 spectra in proton-proton collisions at $\sqrt{s} = 8$ TeV", *JHEP* **04** (2015) 025,
742 doi:10.1007/JHEP04(2015)025, arXiv:1412.6302.
- 743 [25] ATLAS Collaboration, "Search for contact interactions and large extra dimensions in
744 dilepton events from pp collisions at $\sqrt{s} = 7$ tev with the atlas detector", *Phys. Rev. D* **87**
745 (2013) 015010, doi:10.1103/PhysRevD.87.015010.
- 746 [26] CMS Collaboration, "Search for Large Extra Dimensions in the Diphoton Final State at
747 the Large Hadron Collider", *JHEP* **05** (2011) 085, doi:10.1007/JHEP05(2011)085,
748 arXiv:1103.4279.
- 749 [27] CMS Collaboration, "Search for signatures of extra dimensions in the diphoton mass
750 spectrum at the large hadron collider", *Phys. Rev. Lett.* **108** (2012) 111801,
751 doi:10.1103/PhysRevLett.108.111801.
- 752 [28] ATLAS Collaboration, "Search for extra dimensions in diphoton events using
753 proton-proton collisions recorded at $\sqrt{s} = 7$ tev with the atlas detector at the lhc", *New J.
754 Phys.* **15** (2013) 043007, doi:10.1088/1367-2630/15/4/043007.

- [29] ATLAS Collaboration, "Search for contact interactions and large extra dimensions in the dilepton channel using proton-proton collisions at $\sqrt{s} = 8$ TeV with the ATLAS detector", *Eur. Phys. J. C* **74** (2014), no. 12, 3134, doi:10.1140/epjc/s10052-014-3134-6, arXiv:1407.2410.
- [30] D0 Collaboration, "Measurement of dijet angular distributions at $\sqrt{s} = 1.96$ tev and searches for quark compositeness and extra spatial dimensions", *Phys. Rev. Lett.* **103** (2009) 191803, doi:10.1103/PhysRevLett.103.191803.
- [31] R. Franceschini et al., "Lhc bounds on large extra dimensions", *JHEP* **05** (2011) 092, doi:10.1007/JHEP05(2011)092.
- [32] P.C. Argyres, S. Dimopoulos and J. March-Russell, "Black holes and sub-millimeter dimensions", *Phys. Lett. B* **441** (1998) 96–104, doi:10.1016/S0370-2693(98)01184-8.
- [33] S. Dimopoulos and G.L. Landsberg, "Black holes at the lhc", *Phys. Rev. Lett.* **87** (2001) 161602, doi:10.1103/PhysRevLett.87.161602.
- [34] S.B. Giddings and S.D. Thomas, "High energy colliders as black hole factories: the end of short distance physics", *Phys. Rev. D* **65** (2002) 056010, doi:10.1103/PhysRevD.65.056010.
- [35] S. W. Hawking, "Particle creation by black holes", *Commun. Math. Phys.* **43** (1975) 199–220, doi:10.1007/BF02345020.
- [36] CMS Collaboration, "Search for microscopic black hole signatures at the large hadron collider", *Phys. Lett. B* **697** (2011) 434, doi:10.1016/j.physletb.2011.02.032.
- [37] CMS Collaboration, "Search for microscopic black holes in pp collisions at $\sqrt{s} = 7$ tev", *JHEP* **04** (2012) 061, doi:10.1007/JHEP04(2012)061.
- [38] CMS Collaboration, "Search for microscopic black holes in pp collisions at $\sqrt{s} = 8$ tev", *JHEP* **07** (2013) 178, doi:10.1007/JHEP07(2013)178.
- [39] ATLAS Collaboration, "Search for low-scale gravity signatures in multi-jet final states with the atlas detector at $\sqrt{s} = 8$ tev", *JHEP* **07** (2015) 032, doi:10.1007/JHEP07(2015)032.
- [40] ATLAS Collaboration, "Search for strong gravity in multijet final states produced in pp collisions at $\sqrt{s} = 13$ tev using the atlas detector at the lhc", *JHEP* **03** (2015) 026, doi:10.1007/JHEP03(2016)026.
- [41] X. Calmet, W. Gong, and S. D. H. Hsu, "Colorful quantum black holes at the lhc", *Phys. Lett. B* **668** (2008) 20, doi:10.1016/j.physletb.2008.08.011.
- [42] P. Meade, L. Randall, "Black holes and quantum gravity at the lhc", *JHEP* **05** (2008) 003, doi:10.1088/1126-6708/2008/05/003.
- [43] D. M. Gingrich, "Quantum black holes with charge, colour, and spin at the lhc", *J. Phys. G* **37** (2010) 105008, doi:10.1088/0954-3899/37/10/105008.
- [44] L. Randall, and R. Sundrum, "Large mass hierarchy from a small extra dimension", *Phys. Rev. Lett.* **83** (1999) 3370, doi:10.1103/PhysRevLett.83.3370.

- 794 [45] L. Randall, R. Sundrum, "An alternative to compactification", *Phys. Rev. Lett.* **83** (1999)
795 4690, doi:10.1103/PhysRevLett.83.4690.
- 796 [46] J. Abdallah et al., "Simplified Models for Dark Matter Searches at the LHC", *Phys. Dark
797 Univ.* **9-10** (2015) 8–23, doi:10.1016/j.dark.2015.08.001, arXiv:1506.03116.
- 798 [47] G. Busoni et al., "Recommendations on presenting LHC searches for missing transverse
799 energy signals using simplified s-channel models of dark matter", arXiv:1603.04156.
- 800 [48] ATLAS Collaboration, "Search for new phenomena in dijet events using 37 fb^{-1} of pp
801 collision data collected at $\sqrt{s} = 13 \text{ TeV}$ with the ATLAS detector", *submitted to PRD* (2017)
802 arXiv:1703.09127.
- 803 [49] CMS Collaboration, "Search for dijet resonances in proton-proton collisions at $\text{sqrt}(s) = 13$
804 TeV and constraints on dark matter and other models", *Phys. Lett. B* (2016)
805 doi:10.1016/j.physletb.2017.02.012, arXiv:1611.03568.
- 806 [50] ATLAS Collaboration, "Search for new phenomena in final states with an energetic jet
807 and large missing transverse momentum in pp collisions at $\sqrt{s} = 13 \text{ TeV}$ using the
808 ATLAS detector", *Phys. Rev. D* **94** (2016), no. 3, 032005,
809 doi:10.1103/PhysRevD.94.032005, arXiv:1604.07773.
- 810 [51] CMS Collaboration, "Search for dark matter produced with an energetic jet or a
811 hadronically decaying W or Z boson at $\sqrt{s} = 13 \text{ TeV}$ ", *submitted to JHEP* (2017)
812 arXiv:1703.01651.
- 813 [52] CMS Collaboration, "Jet in 0.9 and 2.36 tev pp collisions", *CMS Physics Analysis Summary
814 CMS-PAS-JME-10-001* (2010).
- 815 [53] CMS Collaboration, "Determination of jet energy calibration and transverse momentum
816 resolution in CMS", *JINST* **06** (2011) 11002,
817 doi:10.1088/1748-0221/6/11/P11002.
- 818 [54] T. Sjostrand, S. Mrenna, and P. Skands, "A brief Introduction to PYTHIA 8.1", *Comput.
819 Phys. Comm.* **178** (2008) 852, doi:10.1016/j.cpc.2008.01.036.
- 820 [55] GEANT4 Collaboration, "G4—a simulation toolkit", *NIM A506* (2003).
- 821 [56] CMS Collaboration, "Jet performance in pp collisions at 7 tev", *CMS Physics Analysis
822 Summary CMS-PAS-JME-10-003* (2010).
- 823 [57] CMS Collaboration, "Jet energy resolutions derived from qcd simulation for the analysis
824 of first $\sqrt{s} = 7 \text{ tev}$ collision data", (2010). CMS AN-2010/121.
- 825 [58] CMS Collaboration, "Jet position resolutions in 7 tev data", (2010). CMS AN-2010/121.
- 826 [59] T. Adye, "Unfolding algorithms and tests using RooUnfold", in *Proceedings of the
827 PHYSTAT 2011 Workshop on Statistical Issues Related to Discovery Claims in Search
828 Experiments and Unfolding*, pp. 313–318. Geneva, Switzerland, January, 2011.
829 arXiv:1105.1160.
- 830 [60] G. D'Agostini, "A multidimensional unfolding method based on bayes' theorem",
831 *Nuclear Instruments and Methods in Physics Research Section A: Accelerators, Spectrometers,
832 Detectors and Associated Equipment* **362** (1995), no. 23, 487 – 498,
833 doi:[http://dx.doi.org/10.1016/0168-9002\(95\)00274-X](http://dx.doi.org/10.1016/0168-9002(95)00274-X).

- 834 [61] Z. Nagy, "Three-jet cross sections in hadron hadron collisions at next-to-leading order",
 835 *Phys. Rev. Lett.* **88** (2002) 122003, doi:10.1103/PhysRevLett.88.122003.
- 836 [62] T. Kluge, K. Rabbertz, and M. Wobisch, "Fast pQCD calculations for PDF fits", in *14th*
 837 *International Workshop on Deep Inelastic Scattering (DIS 2006)*, 20-24 Apr 2006, pp. 483–486.
 838 Tsukuba, Japan, April, 2006. arXiv:hep-ph/0609285.
- 839 [63] M. Heinrich, A. Oehler, K. Rabbertz, "Nlo calculations for inclusive jets with fastnlo at 10
 840 tev", *AN-2009-058* (2009).
- 841 [64] S. Dulat et al., "The CT14 Global Analysis of Quantum Chromodynamics",
 842 arXiv:1506.07443.
- 843 [65] S. Dittmaier, A. Huss, and C. Speckner, "Weak radiative corrections to dijet production at
 844 hadron colliders", *JHEP* **11** (2012) 095, doi:10.1007/JHEP11(2012)095,
 845 arXiv:1210.0438.
- 846 [66] J. Gao et al., "Next-to-leading qcd effect to the quark compositeness search at the lhc",
 847 *Phys. Rev. Lett.* **106** (2011) 142001, doi:10.1103/PhysRevLett.105.262001.
- 848 [67] D. M. Gingrich, "Monte carlo event generator for black hole production and decay in
 849 proton-proton collisions", *Comput.Phys.Commun.* **181** (2010) 1917–1924,
 850 doi:10.1016/j.cpc.2010.07.027.
- 851 [68] M. Backovic, K. Kong, and M. McCaskey, "MadDM v.1.0: Computation of Dark Matter
 852 Relic Abundance Using MadGraph5", *Physics of the Dark Universe* **5-6** (2014) 18–28,
 853 doi:10.1016/j.dark.2014.04.001, arXiv:1308.4955.
- 854 [69] M. Backovi et al., "Direct Detection of Dark Matter with MadDM v.2.0", *Phys. Dark Univ.*
 855 **9-10** (2015) 37–50, doi:10.1016/j.dark.2015.09.001, arXiv:1505.04190.
- 856 [70] G. Cowan, K. Cranmer, E. Gross, and O. Vitells, "Asymptotic formulae for
 857 likelihood-based tests of new physics", *Eur. Phys. J. C* **71** (2011) 1554, doi:10.1140/
 858 epjc/s10052-011-1554-0, 10.1140/epjc/s10052-013-2501-z,
 859 arXiv:1007.1727. [Erratum: *Eur. Phys. J. C* **73** (2013) 2501].
- 860 [71] T. Junk, "Confidence level computation for combining searches with small statistics",
 861 *Nucl. Instrum. Meth.* **A434** (1999) 435, doi:10.1016/s0168-9002(99)00498-2.
- 862 [72] A. L. Read, "Modified frequentist analysis of search results", in *First Workshop on*
 863 *Confidence Limits*, pp. 81–101. CERN, Geneva, Switzerland, 2000.
- 864 [73] R. Cousins, "Saturated model for goodness of fit", doi:<http://www.physics.ucla.edu/~cousins/stats/cousins\饱和.pdf>.
- 865